Advanced Automatic Techniques for Image Analysis

Giulia Troglio

Advanced Automatic Techniques for Image Analysis

Giulia Troglio

Joint Ph.D. program in:

Electrical and Computer Engineering, University of Iceland

Electronic, Computer, Robotics, and Telecommunications Engineering, University of Genoa

Advisors:
Prof. Jón Atli Benediktsson
Prof. Sebastiano Bruno Serpico

Committee:
Prof. Jón Atli Benediktsson, Chairman
Prof. Sebastiano Bruno Serpico, Co-chairman
Dr. Gabriele Moser
Prof. Einar Stefánsson
Prof. Jóhannes Rúnar Sveinsson

Opponents:
Prof. John Kerekes
Prof. Josiane Zerubia

Defence President:
Prof. Helgi Þorbergsson

Faculty of Electrical and Computer Engineering,
University of Iceland

Faculty of Engineering, University of Genoa

Reykjavik, May 2011

Advanced Automatic Techniques for Image Analysis
Segmentation, registration, and change detection
Thesis submitted in partial fulfillment of a joint *Philosophiae Doctor* degree in
Electrical and Computer Engineering and in Electronic, Computer, Robotics, and
Telecommunications Engineering

Faculty of Electrical and Computer Engineering
School of Engineering and Natural Sciences
University of Iceland
VR-II, Hjardarhaga 2-6,
107, Reykjavik, Iceland

Telephone: +354 525 4000

Faculty of Engineering
University of Genoa
Via Montallegro 1,
16145, Genova, Italy

Reykjavík, April 2011

Abstract

Image analysis is aimed at extracting meaningful information from images, by means of digital processing techniques. It covers diverse applications, which are continuously expanding through all areas of science and industry, including, among all, medicine, astronomy, security, remote sensing. Several techniques for the automatic analysis of images have been proposed for different purposes. Generally, each technique is applied to a small range of tasks and often outperformed by human analyzing capabilities. Hence, there is still the need for developing new and advanced methods of image analysis.

In this thesis, we propose and develop novel methods and algorithms for the analysis of different types of images and for different purposes. The proposed methods are applied to two different fields, i.e., diagnostic ophthalmology and planetary surface analysis.

In this framework, the novel contributions of the present thesis can be collected in three areas.

First, various feature-extraction methods are proposed and applied in different contexts. On one hand, segmentation methods for the extraction of spatial features from planetary images are proposed. Different feature extraction techniques are explored and applied for the detection of craters and rocks on planetary images. The application of the proposed methods for registration purposes is also presented. On the other hand, feature extraction in retinal images is proposed as a

preprocessing step for the registration of multitemporal images.

Subsequently, a feature-based image registration approach is proposed, based on global optimization techniques, in order to spatially align pairs of images. In particular, a genetic algorithm is used to match previously extracted features from an image pair to be registered (e.g., blood vessel maps from retinal images or elliptical features from planetary images).

Finally, we concentrate on approaches to analyze multitemporal registered images, focusing on change-detection. Different change-detection approaches, based on automatic thresholding techniques and multiple classifiers, are proposed and applied to analyze pairs of multitemporal retinal images. Then, the classification of temporal changes is addressed, by analyzing different image features.

The new techniques, developed in this thesis and experimentally validated on diverse data, improve the state of the art in each of the mentioned application fields, when compared to previously proposed methods, and thus show great potential for various image analysis scenarios.

Keywords: Image registration, image segmentation, feature extraction, change-detection, retinal images, planetary images, genetic algorithm, Hough transform, watershed, marked point process, multiple classifiers.

Ágrip

Myndgreining miðar að því að nota stafrænar aðferðir til að draga upplýsingar fram úr myndum. Myndgreining hefur margs kyns notkunarsvið í vísindum og iðnaði, og eru notkunarsviðin sífellt að verða víðtækari og má nefna dæmin læknisfræði, stjörnufræði, öryggismál og fjarkönnun. Nokkrar aðferðir til sjálfvirkar greiningar mynda fyrir mismunandi notkunarsvið hafa komið fram á undanförnum árum. Að jafnaði er sérhver aðferð hönnuð fyrir þröngt notkunarsvið og því getur fólk oft náð betri árangri í greiningu vandamálanna með berum augum. Af þessum sökum er nauðsyn að þróa nýjar og framsæknar aðferðir til sjálfvirkrar myndgreiningar.

Í þessari doktorsritgerð, eru lagðar til og þróaðar nýjar aðferðir og algrím fyrir sjálfvirka myndgreiningu. Nýju aðferðunum er beitt á tvo mismunandi notkunarsvið, þ.e. greiningu í augnlæknisfræði og yfirborðsgreiningu á reikistjörnum.

Með tilliti til ofangreinds, má flokka framlag ritgerðarinnar í þrjú meginsvið.

Fyrst má nefna að margar aðferðir til útdtráttar á einkennum (e. *feature extraction*) eru kynntar og beitt í mismunandi samhengi. Í fyrsta lagi eru settar fram myndhlutunar aðferðir (e. *segmentation*) sem draga fram rúmfræðileg einkenni fyrir myndir af reikistjörnum (e. *planetary images*). Nokkrar mismunandi þannig aðferðir eru skoðaðar og þeim beitt í skynjun gíga og steina í reikistjarnamyndum.

Aðferðunum er einnig beitt við skráningu mynda (e. *image registration*). Í öðru lagi eru aðferðir til framdráttar einkenna í augnbotnamyndum settar fram sem forvinnsluaðferð fyrir skráningu mynda frá mismunandi tímum.

Því næst er myndskráningaraðferð sem byggir á notkun einkenna sett fram. Þessi aðferð byggir á víðværri bestunartækni sem leitast við að stilla pör mynda rúmfræðilega saman. Erfðafræðilegt algrím (e. *genetic algorithm*) er notað til að samstilla einkenni sem dregin hafa verið fram úr þeim myndpörum er skrá skal saman (t.d. kort af æðum í augnbotnamyndum eða sporöskjulaga einkenni úr myndum af reikistjörnum).

Að lokum eru rannsakaðar aðferðir til að greina skráðar myndir frá mismunandi tímum með höfuðáherslu á skynjun á breytingum (e. *change detection*) í myndunum. Mismunandi aðferðir til skynjunar á breytingum eru settar fram en þessar aðferðir byggja á sjálfvirkum þröskuldum og fjölflokkurum (e. *multiple classifiers*). Aðferðunum er beitt við greiningu á pörum augnbotnamynda frá mismunandi tímum. Síðan er gerð flokkun á breytingum sem orðið hafa með því að nota mismunandi einkenni myndanna.

Nýju aðferðirnar sem þróaðar eru í ritgerðinni og staðfestar með beitingu á mismandi gögn, er framlag til þeirra notkunarsviða sem fjallað er um í ritgerðinni eins og sýnt er með samanburði við fyrri aðferðir. Nýju aðferðirnar bjóða því upp á mikla möguleika í margs konar myndgreiningarverkefnum.

Lykilorð Myndgreining, hlutun mynda, útdráttur einkenna, skynjun breytinga, augnbotnamyndir, myndir af reikistjörnum, erfðafræðileg algrím, Hough vörpun, vatnaskil, merkt punktferli, fjölflokkarar.

Sommario

L'analisi di immagini consiste nell' estrazione di informazioni significative da immagini digitali, attraverso specifiche tecniche di elaborazione. Essa ricopre varie applicazioni in continua espansione attraverso tutte le aree della scienza e dell'industria, che includono, tra le altre, medicina, astronomia, sicurezza, telerilevamento. Sono state proposte diverse tecniche per l'analisi automatica di immagini a vari scopi. Generalmente, ogni tecnica è applicabile ad un piccolo insieme di compiti e spesso superata dalle capacità umane. Quindi, lo sviluppo di metodi nuovi ed avanzati per l'analisi di immagini risulta tuttora necessario.

Nella presente tesi, si propongono metodi ed algoritmi innovativi per l'analisi di diversi tipi di immagini e a vari scopi. L'applicazione dei metodi proposti avviene in due diversi ambiti, quali l'oftalmologia diagnostica e l'analisi di superfici planetarie.

In tale contesto, i contributi innovativi della presente tesi si raggruppano in tre diverse categorie.

In primo luogo, si propongono diversi metodi per l'estrazione di strutture spaziali caratteristiche (*feature*) e si applicano in diversi ambiti. Da un lato, si esplorano metodi per l'estrazione di strutture spaziali da immagini planetarie, nelle quali la rivelazione di crateri e rocce viene effettuata attraverso diverse tecniche di segmentazione; tali metodi vengono applicati al fine di registrare immagini planetarie.

Dall'altro lato, si propone l'estrazione di *feature* in immagini della retina come fase di pre-elaborazione per la registrazione di immagini retiniche multitemporali.

Successivamente, si propone un approccio per la registrazione, attraverso l'utilizzo di tecniche di ottimizzazione globale, allo scopo di allineare spazialmente coppie di immagini. In particolare, si utilizza un algoritmo genetico per determinare la corrispondenza tra *feature* precedentemente estratte da una coppia di immagini da registrare. Tali possono essere, ad esempio, mappe dei capillari in immagini retiniche o strutture ellittiche in immagini planetarie.

Infine, si studiano approcci per l'analisi di immagini multitemporali precedentemente registrate. In particolare, ci si focalizza su tecniche di rivelazione di cambiamenti. Si propongono diversi approcci di rivelazione di cambiamenti, basati su tecniche di sogliatura automatica e classificatori multipli. Le tecniche proposte vengono utilizzate per l'analisi coppie di immagini retiniche acquisite in tempi diversi. Successivamente, si affronta il problema della classificazione dei cambiamenti rilevati, analizzando diverse caratteristiche.

Le nuove tecniche, sviluppate in questa tesi e valutate sperimentalmente su varie tipologie di immagini, migliorano lo stato dell'arte in ognuno degli ambiti applicativi menzionati, in confronto a metodi precedentemente proposti nella letteratura scientifica. Pertanto costituiscono un elevato potenziale in vari scenari dell'analisi di immagini.

Parole chiave: Registrazione di immagini, segmentazione, estrazione di *feature*, rivelazione di cambiamenti, diagnostica per immagini della retina, pianeti, algoritmo genetico, trasformata di Hough, watershed, processo a punti marcati, classificatori multipli.

Contents

List of Acronyms

BA   Bayesian Algorithm
CVA   Change Vector Analysis
DEM   Digital Elevation Model
GA   Genetic Algorithm
GHT   Generalized Hough Transform
HiRISE   High Resolution Imaging Science Experiment
HLS   Hue Lightness Saturation color model
HR   HiRise image
IR   InfraRed THEMIS image
K&I   K&I applied on the Entire Image
KEI   Kittler and Illingworth thresholding
MAP   Maximum A-posteriori Probability
MC   Multiple Classifier approach
MCMC   Markov Chain Monte-Carlo
MOM   Measure Of Match
MPP   Marked Point Process
MRO   Mars Reconnaissance Orbiter
PI   Planetary Image
RGB   Red Green Blue color model
RI   Retinal Image
SA   Simulated Annealing
SE   Structuring Element
SVM   Support Vector Machines
THEMIS   THermal EMission Imaging System
VIS   VISible THEMIS image

Part I

Extended Research Summary

Chapter 1

Introduction and Thesis Overview

Visual information plays an important role in almost all areas of our life. Thanks to the fast spreading of new digital tools, nowadays much of this information is represented and processed digitally. Digital image analysis has become a challenging problem. It covers a wide range of fields, with applications ranging from remote sensing to diagnostic medicine, from astronomy to robotics, from security to microscopy. An effective exploitation of such potential calls for the development of accurate and fast image analysis procedures, able to extract the information of interest from the available image data.

In this context, different image analysis issues are addressed here. The aim of this thesis is to propose innovative and advanced approaches to solve different problems, which can be applied to different specific areas of interest. The issues addressed in this thesis can be grouped into three categories, i.e., image segmentation, image registration, and change detection. Several algorithms, which have been developed to address specific image analysis problems, are proposed.

This chapter introduces the framework of the research work that

will be presented in this thesis. Then, the thesis objectives and main contributions are described. These contributions will be further discussed in the following chapters (i.e., Chapters 2, 3, and 4), each of them focusing on one of the problems and on the corresponding developed methods. Results obtained by applying the proposed algorithms to specific data will be presented in Chapter 5. General conclusions about the approaches proposed in the thesis will be drawn in Chapter 6. Finally, the second part of the thesis is composed of different annexes, each of them representing a publication related to the main findings of the research work.

1.1   Image Analysis

Image analysis is aimed at extracting meaningful information from digital images and involves the use of image processing techniques. In particular, it is the process of characterizing an image with its content description at a given semantical level.

Image analysis has become a critical component in contemporary science and technology and has extensive applications, which are continuously expanding through many different areas. Applications include, among others, medicine, remote sensing, astronomy, robotics, etc. In particular, in medical applications, image analysis can be used in order to detect specific diseases, providing a powerful tool as a support for the diagnostic process. Applications range from the detection of cancer in MRI (Magnetic Resonance Imaging) scans, to the monitoring of diabetic retinopathy through the analysis of retinal images. Moreover, environmental remote sensing represents the set of image processing techniques aiming at retrieving information about a geographical area by exploiting Earth-observation data. This type of technology has been

acquiring a growing interest from the viewpoints of environmental monitoring and management. In addition, the analysis of planetary images has been acquiring strong attention. In fact, thanks to the increasing number of planetary missions devoted to the acquisition of planetary imagery, image-analysis technologies present a huge potential for a wide range of planetary applications. Among them, selecting safe landing sites, identifying planetary resources, and preparing for subsequent planetary exploration by humans and robots.

The research work described here is aimed at identifying novel and advanced image processing approaches for different applications. In particular, from an application viewpoint, we focus on the analysis of retinal images, on one side, and planetary images, on the other side.

In both frameworks, in the ideal case, the features of interest are sharp and clearly defined, hence, easy to detect. In practice, however, image quality can be uneven, due to different factors.

Here, we deal with images acquired with different modalities, under poor illumination conditions, different field angles, etc. Those images are difficult to analyze and the features represented are generally barely visible. Hence, the proposal of new advanced techniques for their automatic analysis is highly desirable.

On one hand, we focus on the analysis of retinal images. In ophthalmology, diagnosis of retinal diseases is based on the analysis of the changes in the retina that can occur during time. The analysis of multitemporal images is an important diagnostic tool. Fundus images may be used to diagnose many diseases that affect the vascular structure by revealing the changes that have occurred in it during the period between two consecutive medical visits. A multitude of image devices have been brought into clinical practice, by facilitating visual access to different parts of the eye. In particular, fundus cameras have been commonly used over the last decades. These devices produce a large amount of

images that need to be visually inspected by ophthalmologists to diagnose abnormalities. Therefore, automatic methods of retinal image analysis have been acquiring a growing interest in order to support the diagnosis. The aim of the work presented in this thesis, which will be detailed in the following section, is to develop a set of new algorithms to help ophthalmologist diagnosis and to be used in automated systems for retinopathy screening.

On the other hand, the analysis of planetary images is addressed. With each new planetary mission, the volume of acquired data significantly increases. Different types of data are being collected at different times, by different sensors, and from different view-points. Feature extraction, i.e., extraction of spatial features in the images, is typically the first step in most image analysis processes. For instance, registration is an essential task to jointly exploit, integrate, or compare all these different data and usually requires a prior accurate extraction of the spatial features in the image. Identification of spatial features on planetary surfaces can be manually performed by human experts but this process can be very time consuming. Therefore, a reliable automatic approach to detect the position, structure, and dimension of each feature is highly desirable. This is a difficult task for several reasons: Limited data are usually available, the contrast of planetary images is generally low (i.e., it is heavily affected by illumination, surface properties and atmospheric state), and the features that are present in the images can be barely visible due to atmospheric erosion and they may be based on different structure types of variable sizes. Hence, the proposal of new automatic approaches to help planetary scientists in identifying spatial features to be used in automated systems for image registration is of high interest.

1.2 Aim of The Thesis

The main objective of this thesis is the development of new advanced methods and algorithms for the analysis of different types of data. The developed approaches should be efficient in terms of accuracy and computational complexity. In particular, here, we address the following specific issues:

1. Image segmentation, i.e., the process of partitioning an image into multiple regions, generally used to locate objects in an image.

2. Image registration, i.e., the process of spatially aligning two or more images, a step always necessary when comparing two or more images.

3. Change detection, i.e., the process of identifying differences in the state of an object or phenomenon, by observing it at different times through multitemporal images.

The main contributions of this thesis are summarized in Figure 1.1, which depicts the proposed methods and algorithms for feature extraction, image registration and change detection of the analyzed data. In order to achieve our objective, we address the three different main issues previously defined and propose and develop different novel solutions.

1. Image segmentation methods are proposed with a specific focus on:

    a) Feature extraction in retinal images, based on mathematical morphology, for registration purposes (described in Chapter 2).

    b) Feature extraction in planetary images, by using watershed segmentation combined with the generalized Hough transform, for registration purposes (detailed in Chapter 2 and object of the paper reported in Annex C).
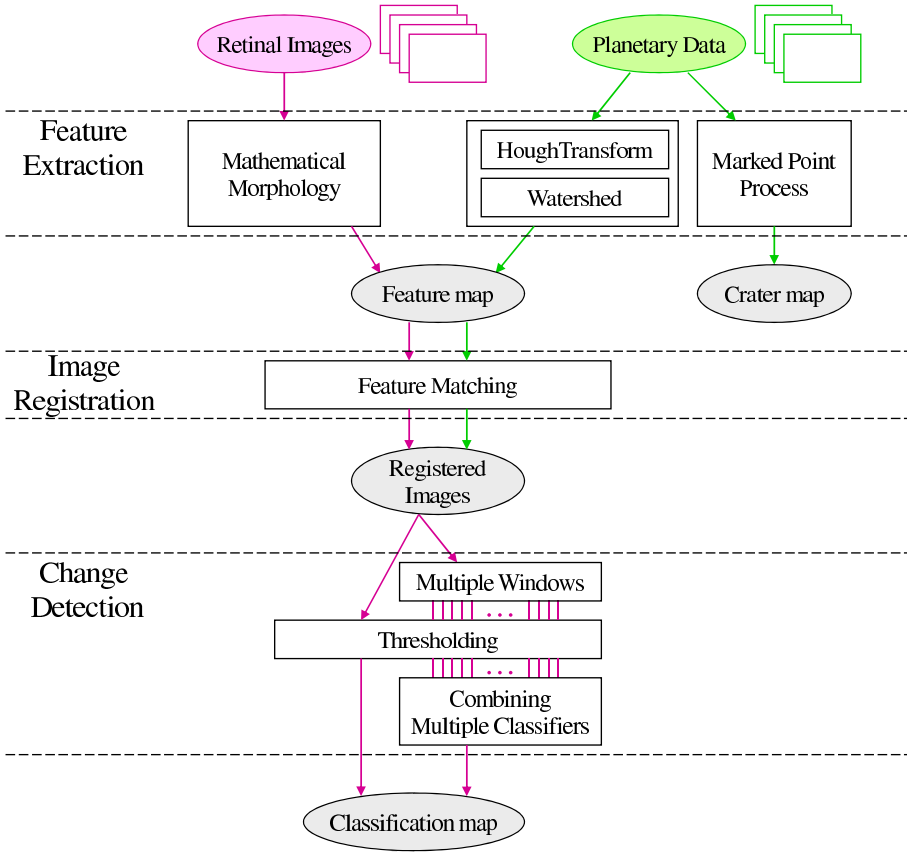
Figure 1.1: Overall block diagram of the proposed methods for feature extraction, registration and change detection of the analyzed images.

    c) Crater detection in planetary images, based on marked point processes (introduced in Chapter 2 and subject of the paper reported in Annex D).

2. Image registration is addressed for:

    a) Registration of retinal images by matching the extracted features, i.e., retinal blood vessels, through a Genetic Algorithm, GA (described in Chapter 3 and in the book chapter presented in Annex A).

b) Registration of planetary images by matching through GA the elliptical features previously extracted (i.e., craters and rocks) by using the method proposed in the paper reported in Annex C (as detailed in the same annex).

3. Change detection in multitemporal retinal images, especially focusing on:

    a) Change detection by using an automatic thresholding technique (detailed in Chapter 4 and addressed in Annex A).

    b) Change detection by using an automatic thresholding technique integrated within a multiple classifier approach (detailed in Chapter 4 and in the paper reported in Annex B).

1.3   Thesis Structure

This thesis is composed as a collection of publications, preceded by an extended research summary. The manuscript is organized as follows: Chapters 2, 3, and 4 deal with the problems addressed in this thesis, which are image segmentation, image registration, and change detection, respectively. In particular, in each of the three Chapters an overview of the analyzed problem is introduced, an overview of the literature analysis is given, and, finally, the architecture of the proposed approaches is detailed. An evaluation of the results obtained by applying the proposed approaches is given in Chapter 5. Concluding remarks and suggestions for future work are drawn in Chapter 6.

In the subsequent annexes different publications presenting the main findings of this thesis are collected:

Annex A Book Chapter proposing a full system for registration and change detection in retinal images, as a support for the diagnosis

of retinopathy. The images are acquired from the same patient during different medical visits by a color fundus camera. An automatic registration approach, based on the extraction of the vascular structures in the images to be registered and the optimization of their match, is investigated. Then, in order to achieve the detection of temporal changes, an unsupervised approach, based on a minimum-error thresholding technique, is investigated. The algorithm is tested on color fundus images with small and large changes.

Annex B is a paper proposing a novel method for change detection in retinal images, based on a minimum-error thresholding technique integrated within a multiple classifier approach. Unsupervised thresholding is applied to separate the "change" and the "no-change" areas in a suitably defined difference image. However, in order to cope with local illumination differences, the thresholding technique is applied to randomly selected sub-images: The outputs of the different windows are combined with a majority vote approach. A novel approach, which performs local analysis by combining spatially different classifiers, is proposed.

Annex C is a paper addressing a feature extraction issue in planetary images. In particular, a new unsupervised method for the extraction of different features of elliptical and geometrically compact shape from the surface of the analyzed planet is proposed. This approach is based on a novel combination of several image processing techniques, including a watershed segmentation and a case-specific formulation of the generalized Hough transform. The method has many applications, including image registration.

Annex D is a paper proposing a novel application of a marked point

10

process for crater detection in planetary images. First, the contours in the image are extracted. The object boundaries are modeled as a configuration of an unknown number of random ellipses, i.e., the contour image is considered as a realization of a marked point process. Then, an energy function is defined, containing both an a priori energy and a likelihood term. The global minimum of this function is estimated by using reversible jump Monte-Carlo Markov chain dynamics and a simulated annealing scheme.

Chapter 2

Image Segmentation for Feature Extraction

Image segmentation is the process of partitioning an image into multiple homogeneous regions with some homogeneity criterion. In particular, each pixel is assigned with a label, such that pixels with the same label share specific characteristics or properties (e.g., color, texture, etc.). As a result the image is partitioned into a finite set of regions delimited by region boundaries. Image segmentation is typically used to locate objects and object boundaries in the analyzed images [106].

Here, different segmentation techniques are proposed, in the contest of the analysis of both Retinal Images (RIs) and Planetary Images (PIs). Concerning the former, methods for the detection of both optic disc and blood vessels in retinal images are investigated. Concerning the latter, different approaches for the identification of spatial features such, as craters and rocks, in PIs are proposed.

This Chapter is organized as follows: Sections 2.1 and 2.2 deal with the segmentation of RIs and PIs, respectively.

2.1 Retinal Image Segmentation

Retinal Images (RIs), generally acquired by a fundus camera, include different features of interest. Indeed, they represent the retina with its vascular structure and the optic nerve head. The choroid is the structure below the retina and it is usually obscured by it. The retina is a multilayer structure, which is transparent except for the deepest layer, the pigmented epithelium. This gives to the retina its reddish color. More superficially than the pigmented epithelium, there is the sensory retina, composed by the photoreceptor cells and the gangliar cells.

The segmentation of RIs, for registration purposes, is investigated here. In particular, the problem of detecting the optic disc is presented in Section 2.1.1 and the vessel extraction issue is addressed in Section 2.1.2.

2.1.1 Optic Disc Detection

The detection and exclusion of the optic disc are essential tasks in order to further analyze RIs. In fact, the identification of the optic disc is indispensable as a preprocessing step for the detection of changes, because the optic disc and the exudates have similar attributes in terms of brightness, color and contrast. Furthermore, the optic disc localization is a first step in understanding ocular fundus images: By estimating the optic disc position and dimension, the localization of the macula can be approximately determined. The macula is the entire area between the temporal vessels and represents the center of vision. It is of great importance as lesions in the macular region affect vision immediately. Localizing the optic disc is also crucial for blood vessel tracking and as a reference length for measuring distances in RIs.

First, an overview of previous work on optic disc detection is presented. Then, the proposed approach is described.

Previous Work

The optic disc is the entrance region of blood vessels and optic nerves into the retina. It is a brighter region than the rest of the fundus, due to the absence of retina layer. The shape of the optic disc is approximately circular, interrupted by the outgoing vessels. Sometimes the optic disc appears as an elliptical object in the image, due to a nonnegligible angle between image plane and object plane. Most of the time, however, it is only partially visible, lying on the border of the image.

An area threshold was used by Tamura *et al.* [113] to localize the optic disc. The contours were detected by means of the Hough transform for the detection of circular features. This approach was quite time consuming and it relied on the approximation of the shape of the optic disc as a circle, which is not always met. In fact, often the optic disc is even not entirely visible in the image plane, and its shape is neither circular nor elliptical. In Pinz *et al.* [92], a similar approach was proposed, in which the Hough transform was used to detect the contours of the optic disc in infrared and argon-blue images. In spite of some improvements, problems were stated if the optic disc does not meet the shape conditions (e.g., if it lies on the border of the image) or if the contrast is too low. In [2], the optic disc was identified by backtracking the vessels to their origin. This is certainly one of the safest ways to localize the optic disc, but it has to rely on vessel detection, which is, in itself, a complex problem. It is desirable to separate the segmentation tasks in order to avoid an accumulation of segmentation errors and reduce computational cost. Mendels *et al.* [71] proposed an approach based on morphological filtering techniques and active contours. Osareh *et al.* [83] described three different methods. The first

14

method, based on template matching, gave a good location of the optic disc; the second one, based on least square regression, estimated the optic disc as a circular shape; the third one, based on snakes, gave a very accurate representation of the shape and location of the optic disc.

Proposed Approach

In this work the location of the optic disc is estimated by exploiting the local grey level variation, as proposed in [108]. The appearance of the optic disc is characterized by a relatively rapid variation in intensity: The dark blood vessels are beside the bright nerve fibres, being the grey level variation in the papillary region higher than in any other part of the image. The variance of intensity of adjacent pixels is used for the recognition of the optic disc.

In the RGB color space, the contours of the optic disc appear more continuous and more contrasted against the background in the red channel. Anyway, this channel has a very narrow dynamic range. Moreover, the optic disc belongs to the brightest parts of the color image. Hence, in order to localize the optic disc, the luminance channel of the HLS color space is used.

Considering a square sub-image $W(i,j)$ of size $M_W \times M_W$ centered on pixel (i, j), the mean intensity within $W(i,j)$, $|I^R|_W$ can be defined as

$$|I^R|_W(i,j) = \frac{1}{M_W{}^2} \sum_{l=i-M_W/2}^{i+M_W/2} \sum_{m=j-M_W/2}^{j+M_W/2} I^R(l,m), \qquad (2.1)$$

where $I^R(l,m)$ is the intensity of the pixel (l,m) in the original retinal image I^R. A variance image V can be obtained by the equation

$$V(i,j) = |(I^R)^2|_W(i,j) - (|I^R|_W(i,j))^2. \qquad (2.2)$$

An image of the average variance $\bar{V}$ within sub-images is then obtained

as

$$\bar{V}(i,j) = |V|_W(i,j). \tag{2.3}$$

The location c_{OD} of the maximum of $\bar{V}$ is selected as an estimate for the center of the optic disc.

The shape of the optic disc is estimated as a circular region, centered in c_{OD} as detected by the proposed method.

2.1.2 Vessel Extraction

The detection of the blood vessels is an essential tasks in order to further analyze RIs. The vascular structure is the most prominent feature in the fundus of the eye, it covers all the retina, and is assumed to be stable over time. Vessel elongation, changes in width and tortuosity may happen, due to specific retinal diseases, but generally they are not large enough between visits to markedly affect the main vascular structure [57].

Actually, automatic detection of blood vessels in RIs is a challenging task. The contrast of such image data diminishes as the distance of a pixel from the center of the image increases. And the presence of noise, the variability of vessel width, the presence of pathological lesions, all make the task more difficult.

First, an overview of previous work on retinal blood vessel detection is presented. Then, the proposed approach is described.

Previous Work

The problem of blood vessel segmentation has been extensively addressed and several solutions have been proposed in the literature. Pappas *et al.* [84] proposed a method for the mapping of arteries in angiograms, based on a local analysis of the image. A model was created for blood vessel densitometry and matched to regions of angiograms to

determine blood vessel location as well as diameter and cross-sectional area. Chauduri *et al.* [24] attempted to match the gray-scale intensities of regions of a retinal image to a Gaussian profile and thereby locate the blood vessels. Edge detection was done by [92], and parallel edges were connected and identified as blood vessels. More recent methods typically utilized three major steps to achieve retinal blood vessel segmentation. Generally, some type of filtering and thresholding is used in a preprocessing stage. The image is, then, processed in one of several ways, and, finally, a post-processing step is aimed at detecting misclassified pixels and patches together labeled segments. Li *et al.* [59] rejected the traditional single Gaussian filter for a double Gaussian filter which more accurately models the vessel profile. Li *et al.* used that piecewise Gaussian model to differentiate between arteries and veins. Lowell *et al.* [64] used a correlation filter to locate the optic disk, frequently a starting point for vessel segmentation algorithms. Such an approach has to rely on vessel detection. Nonetheless, as previously stated, it is desirable to separate the segmentation tasks in order to avoid an accumulation of segmentation errors. Lalonde *et al.* [59] used the Canny operator in order to detect the vessel edges and to estimate the normal vector to the edge. They followed the edge detection with thinning and then a tracking algorithm. Their tracking algorithm tracks each edge of each vessel individually before combining found walls as vessels by exploiting knowledge of the parallel character of vessel borders. In addition, several tracking methods have been implemented in the past. Previous tracking methods proceeded by first determining start points and then tracking the vessels from those points. One principal strategy involved locating the optic disc, usually the brightest part of the eye, and locating starting points from there. For instance, Tamura *et al.* [113] used this strategy and located pixels within the center of vessels by incrementally probing a vessel with a Gaussian profile. Tolias

17

and Panas [116] also proposed a vessel detection starting the segmentation process from the optic disc. In that approach, the probe was propagated by using a fuzzy pixel-classification profile rather than a Gaussian profile. Others chose alternative means to locate tracking starting points. Hoover *et al.* [52] skeletonize a thresholded image and start from the endpoints of the line segments they obtained. Subsequently, they probed the image and tested segments for region-based properties to determine whether they were vessels or not. One of the landmark works in this field was done by [52] and uses a hybrid method. These authors use match filters (as in [24]) to extract possible vessels from the background. This filtered image was then segmented using iterative thresholding. One of the reasons the work is considered so crucial is that they hand-labeled the blood vessels on 20 images and used these as the truth data. This data set has been referenced and used by many subsequent researchers.

Proposed Approach

In this work, blood vessel detection is addressed by using morphological operators.

Only the green channel γ of each RGB image is used in the extraction as it contains most of the vessel information, and it is treated as a gray scale image. First, the green plane γ is normalized, by scaling its histogram (i.e., by calculating minimum and maximum of the image matrix and by scaling its values within the range [0,1]).

Then, vessel segmentation is applied. In [23] an automatic method to detect linear features (i.e., roads) in remote sensing images is presented. The method is unsupervised and involves very few parameters (apart from the model dimensions, just one double threshold is involved). Here, it is used to extract vessel segments in RIs, as it is simple and fast.

18

Specifically, a pre-filtering operation is needed to remove the background noise. In order to remove the structures that are lighter than their surroundings, a morphological opening operator by reconstruction is applied [33]. This is a connected operator: It consists in removing the connected components of a binary image by an erosion and in preserving the other components. Therefore, it does not introduce any new discontinuity in the image. A square Structuring Element (SE) of size equal to five pixels is chosen, assuming that two different vessels will be separated by at least five pixels.

The removal of nonlinear (or too short) darker objects is achieved by taking the minimum of all possible directional morphological closings with predefined length λ_0 [105]. It is computed using linear SEs that are successively oriented in every possible direction (18 different directions for a 15 pixel long linear SE, assuming that all nonlinear dark objects are shorter than the fixed number of pixels).

The third operation is the morphological extraction, performed to detect vessel-pixels. The remaining linear objects that are too wide (more than a predefined size λ_1, corresponding to the maximum vessel width) are removed and the desired structures are extracted. The bottom-hat operator [105], that is, the residue between the current image and its closing, with a flat square SE of size λ_1 equal to 12 pixels, is calculated (assuming that the maximum vessel width corresponds to 12 pixels). The only remaining structures are the wide dark objects. The final binary decision (vessel pixel or not) is taken by a double thresholding with reconstruction: In particular two binary images are obtained, τ_{high} and τ_{low}, using one higher and one lower threshold, respectively. τ_{high} is used as marker and τ_{low} as mask. Finally, a morphological reconstruction of the marker with the connected elements of the mask is applied.

As a result, a binary image (which will be referred to as vessel map,

19

F^R) showing the blood vessel structure is obtained. The proposed technique for feature extraction can be used to register retinal image pairs taken of the same eye. For registration, two binary images need to be extracted from both images to be registered and their match can be estimated (see Chapter 3).

2.1.3 Conclusions

In the previous sections, two different approaches for the segmentation of RIs have been described. The proposed methods will be applied to RIs, acquired by a fundus camera from Icelandic patients attending a retinopathy screening service.

Those methods will be used as a preprocessing step for registration and change detection. In particular, the vessel detection approach presented in the previous section, will be used in order to register pairs of multitemporal RIs (see Chapter 3) Moreover, the optic disc detection approach presented in Section 2.1.1 will be used as a preprocessing step for change detection in retinal image pairs (see Chapter 4). The accuracy of the feature extraction results strongly influences the performance of the following processing steps, as it will be discussed in Chapter 5, where the experimental evaluation of proposed retinal image analysis approaches is presented.

2.2 Planetary Image Segmentation

Optical Planetary Images (PIs) show the surface of the planet that they represent. Identification of spatial features on planetary surfaces can be manually performed by human experts but this process can be very time consuming. Therefore, a reliable automatic approach to detect the position, structure, and dimension of each feature is highly

desirable. This is a difficult task for several reasons: Limited data are usually available, the contrast of PIs is generally low (i.e., it is heavily affected by illumination, surface properties and atmospheric state), and the features that are present in the images can be barely visible due to atmospheric erosion and they may be based on different structure types of variable sizes.

In Section 2.2.1, an overview on the previous works on feature extraction from PIs is presented. Then, the proposed approach for ellipsoidal feature extraction, based on a novel combination of the Canny operator, the Hough transform and the watershed, is detailed in Section 2.2.2. Finally, a novel method for crater detection, based on a Marked Point Process (MPP), is investigated in Section 2.2.3.

2.2.1 Previous Work

Among the typical features in planet-surface imagery, craters play a primary role. Detection of craters has been widely addressed and different approaches have recently been proposed in the literature, based on the analysis of planetary topography data [102], satellite images in the visible spectrum and the infrared spectrum [41].

The existing techniques can be divided into two main categories; supervised and unsupervised. Supervised methods require the input of an expert and generally use supervised learning concepts to train the algorithm for feature extraction. These techniques contemplate a learning phase, in which a training set of images containing craters is labeled by human experts. Craters are then detected by applying the previously trained algorithm to new unlabeled sets of images. In [122], a continuously scalable detector, based on a supervised template matching technique, is applied. In [124], different supervised

21

learning approaches, including ensemble methods, support vector machines (SVM), and continuously-scalable template models, were employed to derive crater detectors from ground-truthed images. The SVM approach with normalized image patches provided the best detection and localization performance. In a different approach, Martins *et al.* [66] adopted a supervised boosting algorithm, originally developed by Viola and Jones [123] in the context of face detection, to identify craters on Mars.

Unsupervised methods are fully automatic and generally based on image-analysis techniques. These approaches generally rely on the identification of circular or elliptical arrangements of edges along the crater boundary. A standard approach is based on the use of a Generalized Hough Transform (GHT) [120]. Examples include the works of Cross [34], Cheng *et al.* [25], Honda *et al.* [50], Leroy *et al.* [60], and Michael [72]. Instead, in [4], the identification of impact craters was achieved through the analysis of the probability volume created as a result of a template matching procedure, approximating the craters as objects of round shape. That unsupervised method enables the identification of round spatial features. Kim and Muller [54] presented a crater detection method based on texture analysis and ellipse fitting. That method was not robust when applied to optical images. Therefore the authors needed to use also DEM (Digital Elevation Model) data and fuse them with the optical data.

In subsequent work, Kim *et al.* [55] proposed a combination of unsupervised and supervised techniques. In particular, edge detection, template matching, and supervised neural network-based schemes for the recognition of false positives were integrated, in order to automatically detect craters on Mars. In [121], Urbach and Stepinski presented a different approach, which combines unsupervised and supervised techniques, for crater detection in panchromatic PIs. The method in [121]

22

is based on using mathematical morphology for the detection of craters and on supervised techniques to distinguish between objects and false alarms.

Other typical features in PIs are represented by rocks. Rock detection in ground imagery has been addressed in the literature. In particular, in [115] the authors presented a supervised method for segmentation, detection and classification of rocks on data collected by rovers. That approach, based on a probabilistic fusion of data from multiple sensor sources, was tested on Earth data (collected in the Atacama desert in Chile). In [114], the same authors tested different rock detection approaches on Mars Exploration Rover data. In [40], the authors addressed rock detection by using a segmentation method on data collected by the Spirit Mars Rover Planetary Camera. That approach incorporates multiple scale attributes, which include local attributes (e.g., texture), object attributes (e.g., shading), and scene attributes (e.g., illumination direction). Moreover, in [46], the authors proposed an automatic algorithm for rock detection both on ground imagery and on HiRISE data, based on cylinder fitting.

Also, the detection of other types of planetary features, which is not relevant here, has been addressed in the literature (e.g., detection of volcanoes on Venus [15], polygonal patterns on Mars [91], valley networks on Mars [75]).

Each of the previously published methodologies for automatic planetary feature extraction has its advantages and drawbacks. Although the recent approaches show high detection accuracy, the underlying technology is complicated and its robustness to different types of planetary surfaces and to image quality is not totally satisfactory yet.

2.2.2 Proposed Approach for Ellipsoidal Features Extraction

Different types of features are present in the PIs, and their size, shape and position can be estimated. The extracted features can be used for registration purposes.

Here, we focus on detecting features of ellipsoidal shape, such as craters and rocks. Craters are objects of approximately elliptical shape with shadows, due to their depth and uneven illumination. Rocks have small circular or elliptical shape, with almost no shadows. The extraction of these spatial features is a difficult task, because PIs are blurry, quite noisy, present lack of contrast and uneven illumination, and the represented objects are not well defined. For these reasons, a region-based approach that lies on segmentation, has been chosen in order to address such problems. A frequent approach to segmentation introduces a set of characteristic points that are related to the objects to be detected, automatically selected and used as "seed points" to segment the images. Many segmentation approaches have been explored in the literature. Here, the watershed algorithm, presented by Beucher in [7], has been chosen, a method which is automatic, robust and fast. The basic concept of watershed segmentation is giving a topographic representation of a grey-level image (i.e., the grey level of a pixel represents its elevation). A flooding process starts from the minima of the image in terms of elevation, so that the merging of the flooding coming from different sources is prevented. As a result the image is partitioned into two different sets: The catchment basins (i.e., the regions) and the watershed lines (i.e., the region boundaries). The flowchart of the proposed technique for spatial feature extraction is shown in Figure 2.1.

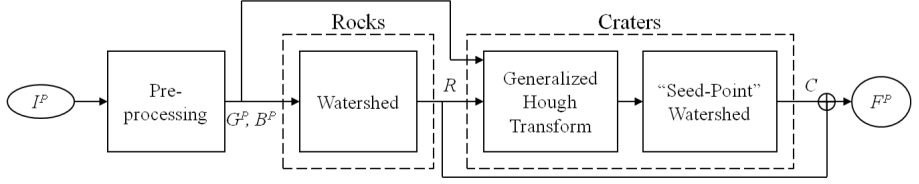Before applying feature extraction techniques, the input image I^P

Figure 2.1: Flowchart of the proposed approach. The original image is first preprocessed, in order to smooth the noise. Then the Canny operator is applied to the smoothed image. In order to detect the rocks, watershed segmentation is applied to the binary image gradient. Crater, which are more complex objects, are detected by using the generalized Hough accumulator: The maxima of the accumulator are used as seed points for the watershed segmentation of the intensity image gradient. The final result is a map of the all the detected features.

needs to be preprocessed. First, the noise is reduced by a smoothing filter. Then, in order to detect edges, the image gradient is computed by using the Canny edge detector [19]. As an intermediate result of this operation an intensity gradient, G^P, is generated. Then, by applying a non-maximum suppression algorithm followed by an hysteresis thresholding to G^P, a binary gradient image, B^P, is obtained but this image shows the contours of the objects represented in the original image.

Rocks generally appear like closed contours in B^P, because of the almost absence of shadows. In order to extract these features, the watershed segmentation algorithm is applied to B^P and closed contours are extracted. All the areas included within a closed contour correspond to "seed point-areas," and are identified as regions. The result of this first step is a binary image R that shows boundaries of small ellipsoidal features of regular shapes, such as rocks.

While rocks generally appear like closed contours and can be easily detected, craters have a more complex structure and, due to their depth and uneven illumination, often exhibit internal shadows. Their borders can be approximated with incomplete non-continuous elliptical curves. A generalized Hough accumulator [120] is used to identify

25

the seed points to detect these structures from B^P. For every pair of pixels that are detected as edge points in B^P and exhibit opposite gradient directions (being the relation of opposition defined with tolerance ϵ), an accumulator, corresponding to the median point between them in the image plane, is incremented by a unit value. The maxima of the accumulator are taken as centers of ellipses. The three parameters describing the ellipse centered in each detected maximum are then computed and a 3D accumulator is used to estimate the two semi-axes and the direction angle of the ellipse from all the pairs of points that contributed to the accumulator in the considered center. The center of each ellipse that has been generated is used as a seed point for segmentation. Starting from all the detected seed points, a watershed algorithm is applied to G^P and the craters are identified. G^P is used in this case because it represents not only the edges but also the elevation information. As a result, a binary image C that shows the boundaries of elliptical features, such as craters, that were not detected by the previous step. In a post-processing step, features are approximated by ellipses and their attributes (i.e., ellipse semi-axes and rotation angle) are estimated. Features with eccentricity $e > 0.6$ are discarded, being features of larger e unlikely to be either craters or rocks. A binary image, F^P, which represents the contours of all detected features, is created. The binary image, F^P, shows the boundaries of the features, identifies their locations and estimates their shapes.

The proposed technique for feature extraction can be used to register image pairs representing the same scene. For registration, two binary images need to be extracted from both images to be registered and their match can be estimated (in Chapter 3 a method for feature matching is proposed, in Chapter 5 an example of the application of the proposed feature extraction approach to image registration is presented).

2.2.3 Proposed Approach for Crater Detection

Different types of spatial features are present in the PIs, but the most evident ones are generally craters, i.e., objects of approximately elliptical shapes with shadows.

In order to detect craters on planetary surfaces, an approach based on a Marked Point Process (MPP) is investigated here. MPPs enable the modeling of the distribution of complex geometrical objects in a scene and have been exploited for different applications in image processing. Marked point processes have been successfully applied to address different problems in terrestrial remote sensing, among which road network extraction [36] and building extraction in dense urban areas [22], [82], [94]. Moreover, in forestry applications, marked point processes have been used to reproduce the spatial distribution of the stems [87]. Here, the method is applied to the detection of craters in PIs.

The context is stochastic and the goal is to minimize an energy on the state space of all possible configurations of objects, using a Markov Chain Monte-Carlo (MCMC) algorithm and a Simulated Annealing (SA) scheme. More properly, a novel MPP is introduced here to model the structure of the crater edges in the image.

The overall architecture of the proposed approach for crater detection is shown in Figure 2.2. First, the noise is reduced by applying a
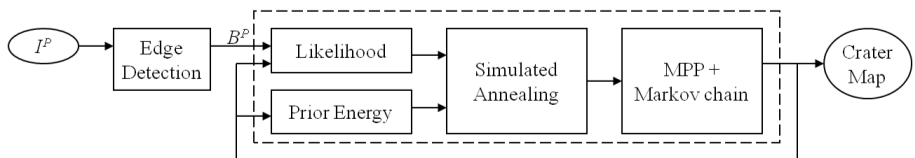

Figure 2.2: Flowchart of the proposed approach.

smoothing filtering operation. Then, in order to produce a binary edge map B^P, showing the contours of the objects represented in the original

27

image, the Canny edge detector [19] is applied. The Canny detector has been chosen because it guarantees a low error rate, the obtained edge points are well localized, and the width of each detected edge is one pixel.

The result of this first step, B^P, is a binary image that shows the object boundaries. Craters have a complex structure and, due to their depth and uneven illumination, exhibit shadows. Their borders can be approximated with incomplete non-continuous elliptical curves.

B^P is modeled as a configuration of objects whose positions and attributes are a realization of an MPP X [89]. The MPP X is a process whose realizations are random configurations x of several objects, each belonging to a space $S = P \times K$, where P is the position space, and K the space of the marks, i.e., set of parameters that fully describe each object. Here, the 2D model, used to extract the features of interest, consists of an MPP of ellipses, and each ellipse is represented by a 5-tuple (u, v, a, b, θ), taking values in the set space

$$S = \overbrace{[0, M] \times [0, N]}^{P} \times \overbrace{[a_m, a_M] \times [b_m, b_M] \times [0, \pi]}^{K}, \qquad (2.4)$$

where $(u, v) \in [0, M] \times [0, N]$ are the coordinates of the ellipse center (M and N being the width and height of B^P), a and b are the ellipse axes (ranging in $[a_m, a_M]$ and $[b_m, b_M]$, respectively), and $\theta \in [0, \pi]$ is the ellipse orientation angle.

The probability distribution of this stochastic process is uniformly continuous [100] with respect to a suitable Poisson measure on S. Operatively, this means that it may be characterized by a density f with respect to this measure. Similarly, the posterior distribution of x conditioned to B^P can also be characterized by a density function f_p with respect to the same measure and a Gibbs formulation is proven to hold

for f_p [82]. Hence, one may introduce an energy function U such that

$$f_p(x|B^P) = \frac{1}{c} \exp\{-U(x|B^P)\}, \tag{2.5}$$

where c is a normalizing constant. Hence, in order to minimize this posterior distribution, U will be minimized on the space of all configurations x in the feature extraction process.

The Proposed Energy Function

The energy function takes into account the interactions between the geometric objects $x_1, x_2, ..., x_n$ in the configuration x (the prior energy U_P), and the way they fit to the data (the likelihood energy U_L)

$$U(x|B^P) = U_P(x) + U_L(B^P|x). \tag{2.6}$$

The prior term characterizes the general aspect of the desired solution. According to the geometric properties of the configurations of craters, a basic rule is imposed on the prior term of our model. The prior energy, U_P, penalizes overlapping objects in x, which are very unlikely, by adding a repulsion between objects which intersect. The prior energy of our model is

$$U_P(x) = \frac{1}{n} \sum_{x_l \star x_m} \varphi(x_l, x_m), \tag{2.7}$$

where φ is a repulsion coefficient, which penalizes each pair of overlapping objects (denoted as $x_l \star x_m$) in the configuration x. The repulsion coefficient φ is calculated as follows

$$\varphi(x_l, x_m) = \frac{x_l \cap x_m}{x_l \cup x_m}, \tag{2.8}$$

where $x_l \cap x_m$ denotes the overlapping area between the two objects x_l and x_m in the configuration $(l, m = 1, 2, ..., n, \ l \neq m$) and $x_l \cup x_m$ indicates the sum of the areas covered by the two objects x_l and x_m.

Then, the likelihood term U_L is defined as

$$U_L(B^P|x) = U_S(B^P|x) + U_D(B^P|x), \tag{2.9}$$

where U_S measures the similarity between the configuration and the data, whereas the data term U_D measures the distance between the objects in the configuration and the contours of the data. Different formulations for the likelihood energy, which have been proposed in previous work on MPP [87,89], have proven to be unfeasible for planetary data. Hence, a new formulation for U_L, more appropriate for the analyzed data, is proposed here.

In particular, the similarity energy U_S between the data B^P and the current configuration x is defined as a correlation measure[1]

$$U_S(B^P|x) = \frac{|\{(u, v) : B^P(u, v) = 1 \ \& \ \Pi(u, v|x) = 1\}|}{|\{(u, v) : B^P(u, v) = 1\}|}, \tag{2.10}$$

where u and v are the spatial coordinates in the image plane; $\Pi(\cdot|x)$ is the projection of the configuration x such that $\Pi(u, v|x) = 1$ if (u, v) belongs to the boundary of at least one ellipse in the configuration x (i.e., if there exists $i \in \{1, 2, ..., n\}$ such that (u, v) is on the boundary of x_l), and $\Pi(u, v|x) = 0$, otherwise. Consequently, U_S expressed as (2.10) is equivalent to the definition of a correlation function between the binary images B^P and $\Pi(\cdot|x)$, representing the extracted and the modeled edges, respectively. According to the correlation definition, in the binary case, only nonzero pixels from both images contribute to the

---

[1]Given a finite set A, we denote by $|A|$ the cardinality (i.e., the number of elements) of A.

value of the correlation. This energy term, which is novel with respect to the MPP literature, resembles analogous correlation measures that have been used for registration purposes [67]. The correlation measure in (2.10) is considered to be appropriate here because it enables to estimate the match between two binary images (B^P and Π) in a fast and accurate way.

Then, the data energy U_D is calculated at the object level: For each object x_l in the current configuration x a weight parameter ψ_l, proportional to the distance from the closest detected edge pixel in the data B^P with respect to its dimension, is calculated, i.e.,

$$\psi_l = \frac{\inf\{\sqrt{(u - u')^2 + (v - v')^2} :\ B^P(u, v) = 1\ \&\ \Pi(u', v'|x_l) = 1\}}{\max(a_l, b_l)},$$

$$(2.11)$$

where $\Pi(\cdot|x_l)$ has a meaning similar to above and a_l and b_l are the two ellipse axes associated to the object x_l $(i = 1, 2, ..., n)$.

The resulting data energy will be

$$U_D(B^P|x) = \frac{1}{n}\sum_{i=1}^{n}\psi_l. \qquad (2.12)$$

Then, objects with a low value of ψ will be favored in the configuration.

Energy Minimization and Crater Mapping

A Markov Chain Monte-Carlo (MCMC) algorithm [43], coupled with a Simulated Annealing (applied with a given annealing schedule $T(\cdot)$), is used in order to find the configuration x which minimizes U. We stress here that this minimization is carried out with respect to not only the locations and marks of the objects in the MPP realization but also the number of objects, i.e., the proposed method also automatically optimizes the choice of the number of detected craters. In particular,

the marked point process X, defined by f, is sampled by using a random jump MCMC algorithm: It allows to build a Markov chain X_k ($k = 0, 1, ...$), which jumps between the different dimensions of the space of all possible configurations and, in the ideal case, ergodically converges to the optimum distribution x^* [97]. The final configuration of convergence does not depend on the initial state. The flowchart of the minimization scheme is shown in Figure 2.3.
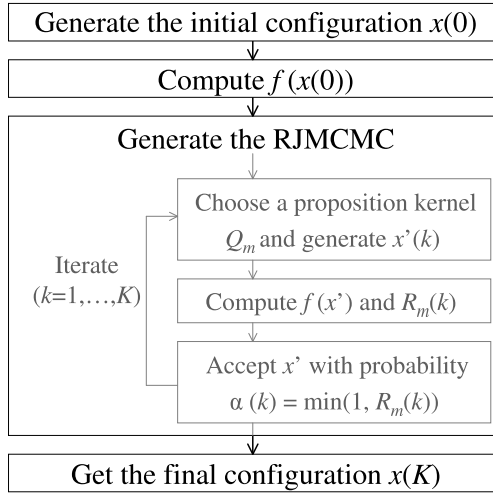
Figure 2.3: Flowchart of the proposed minimization scheme.

At each step, the transition of this chain depends on a set of "proposition kernels", which are random changes proposed to the current configuration. In order to find the configuration maximizing the density $f_p(\cdot)$ on S, we sample within a Simulated Annealing scheme (SA), which gives us the MAP estimator. SA is an iterative algorithm where at each iteration k a perturbation is proposed to the current configuration at temperature $\Gamma(k)$, $k = 1, 2, ..., K$). This perturbation is accepted or rejected with a probability which ensures that the probability distribution of the Markov chain ergodically converges to

$$f_p(x)^{\frac{1}{\Gamma(k)}}. \tag{2.13}$$

32

Here, the annealing schedule, $\Gamma(\cdot)$, is defined as

$$\Gamma(k) = \Gamma_I \cdot \left(\frac{\Gamma_F}{\Gamma_I}\right)^{\frac{k}{K}}, \tag{2.14}$$

where Γ_I and Γ_F are the initial and the final temperatures, respectively, and K is the total number of allowed iterations. In practice, in order to cope with too long computational times, the decrease of the temperature is geometric (as usual in SA for Markov random fields) and does also not imply the ergodic convergence to a probability distribution localized at the minima of $U(x|B^P)$, in contrast, it follows the adaptive approach developed in [88].

The set of proposition kernels are birth and death, translation, dilation, and rotation [48]. For each proposition kernel m, a Green ratio $R_m(x, x')$ is defined, that tunes the likelihood of replacing configuration x by configuration x' at each SA iteration. More precisely, the birth and death kernel consists in proposing, with probability p_B, to uniformly add in S an object to the current configuration x or, with probability $p_D = 1 - p_B$, to remove a randomly chosen object of x.

2.2.4 Conclusions

Here, two different methods for planetary feature extraction have been proposed. First, a segmentation technique, based on a novel combination of the Canny operator, the Generalized Hough Transform (GHT), and the watershed, has been investigated to identify and reconstruct the shape of ellipsoidal features. The proposed approach for ellipsoidal feature extraction can be used for registration purposes, as it will be shown in Chapter 5.

Moreover, a novel crater detection approach, based on the combination of an edge detector and a marked point process, has been proposed.

The MPP approach, which was developed in the context of computer vision and previously used in many different applications (e.g., tree crown identification, road network detection, building extraction), is for the first time applied to PI analysis.

Both methods are tested on images of Mars, acquired by the THEMIS instrument flying on the Mars Odyssey spacecraft. Moreover the first of the proposed methods, aimed at segmenting ellipsoidal features, was tested on HiRISE images collected by the HiRISE camera flying on the Mars Reconnaissance Orbiter. For both approaches, the accuracy of the detection is assessed by comparison to a manually generated reference map (results are presented in Chapter 5).

The proposed approaches can be adopted as the first important step in several applications dealing with all the various data that are being collected during the current and future planetary missions. Among them selecting safe landing sites, identifying planetary resources, and preparing for subsequent planetary exploration by humans and robots.

In our future work we plan to integrate the shadow information around the features in order to improve the reliability of the edge detection and reduce the false alarms in the contour map. Illumination correction, based on the knowledge of the orbital angle and the acquisition time, will be useful to improve the reliability of the detection and reduce the bias in the reconstruction of the exact feature shape.

The proposed approaches will also be applied to the registration of multisensor and multitemporal images, by performing feature matching.

Finally, the proposed methods could be used to extract other features of elliptical shape, such as volcanoes. Additionally, features of other shapes, such as ridges or polygonal patterns among others, could be extracted, by adapting either the generalized Hough transform and the marked point process to the detection of the shape of interest.

Chapter 3

Image Registration

Registration is a fundamental task in image processing in order to compare images acquired under different conditions. It is the process of spatially aligning different images and it is used to match two or more pictures taken, for example, at different times, from different sensors, or from different viewpoints. The problem of registering two or more images is indispensable in diverse applications of computer vision and medical image analysis. For example, temporal registration is necessary when analyzing multitemporal images.

In this work we deal with multitemporal Retinal Image (RI) pairs, hence, image registration is addressed in order to perform their temporal analysis. The approach that will be proposed is general and can be applied to the registration of Planetary Images (PIs) as well.

These applications are diverse and, therefore, it is important to review the basic concepts underlying image registration theory which will be used to formulate the addressed problem.

This chapter is organized as follows: The general theory about image registration is outlined in Section 3.1. Then, an overview of previous work on RI registration is presented in Section 3.1.1. Finally, the proposed approach for the automatic registration of image pairs is

methodologically described in Section 3.2.

3.1 Definition

Image registration can be defined as a mapping between two images both spatially and with respect to intensity. Defined these images as 2-D matrices, denoted by I_{ref} and I_{input}, where $I_{\text{ref}}(i, j)$ and $I_{\text{input}}(i, j)$ represent their respective intensity values, the mapping between images can be expressed as:

$$I_{\text{ref}}(i, i) = g(I_{\text{input}}(T(i, j))), \qquad (3.1)$$

where T is a 2-D spatial coordinate transformation, i.e.,

$$(i', j') = T(i, j) \qquad (3.2)$$

and g is 1-D intensity or radiometric transformation.

The registration problem is the task involved in finding the optimal spatial and intensity transformations so that the images are matched with regard to the misregistration source [9]. Here, only the spatial or geometric transformation will be evaluated.

It can be assumed that any new incoming input image, I_{input}, is being registered with respect to a known reference image, I_{ref}. According to Brown [9], image registration can be viewed as the combination of four components:

1. Feature space, i.e., the set of characteristics extracted from reference and input data that are used to perform the matching.

2. Search space, i.e., the class of potential transformations that establish the correspondence between input data and reference data.

3. Similarity metric, which evaluates the match between input data and transformed reference data for a given transformation chosen in the search space.

4. Search strategy, which is used to choose which transformations have to be computed and evaluated.

3.1.1 Previous Work

Image registration is a difficult task in image processing because correspondence problem is not straightforward. As a consequence, several different registration algorithms have been investigated.

The existing registration methods can be classified into two broad groups: interactive and automatic techniques.

Human-interactive methods have been considered as a reference among the existing methods. Human-involvement neither necessarily achieves the highest accuracy nor reproducibility, but it has been used to prevent catastrophic failures, which are possible with automatic registration methods. The earliest studies of image registration in the ocular imaging area were based on a human interaction [3,86,90]. However, manual registration is time-consuming, often prone to human error, and requires specialized knowledge.

Automatic registration methods have been widely investigated in the last decades. The existing automatic techniques may be sub-classified into different categories based on the image data used, the considered measure of similarity, the selected transformation model, and the method employed for the parameter search [9, 127]. However, in the context of fundus images, registration techniques can be simply sub-classified into feature-based and area-based methods [28].

Feature-based methods are somewhat similar to manual registration. In fact, these techniques are based on the extraction of features

37

in the images to be registered. Features include the vascular structure [17, 52, 110], the optic disc location and boundary [42, 51, 64] and the macula [92]. The ocular blood vessels or their crossing points are commonly used for registration. The registration process is performed by maximizing a similarity measure computed from the correspondences between the extracted features. These approaches assume that feature/point correspondences are available in both images, and their performance largely depends on sufficient and/or reliable correspondences, especially, when the overlapping part of an image pair is very limited or when there are mismatched correspondences. In [85] blood vessels were selected by an adaptive thresholding technique and their correspondence was established by using a sequential similarity detection method. In [45], matched filters were used to detect vessel junctions and correspondences were determined by a local cross-correlation. A group of papers extracted the bifurcations points of the vessels by means of mathematical morphology [126] or Forster detector [38] and then they matched corresponding points. In [18] vascular landmarks are automatically detected and aligned using a hierarchical estimation technique. An iterative method, called dual bootstrap iterative closest point, is presented in [112]: An initial transformation, which is only accurate in a small region (the "bootstrap region") of the mapped image, is estimated and iteratively expanded it into a global transformation estimate.

Area-based techniques are generally based on all pixel intensities within both images to be registered, in order to determine a single best set of transformation parameters for the analyzed image pair. The transformation can be either found by correlation or by optimization, in the spatial or in the frequency domain. Phase correlation [58] has been widely used to estimate translation misalignments, as proposed in [20]. This work was extended in [21] to estimate not only translation but

also rotational parameters: Many incrementally rotated images were generated from the original and correlated. In [96], mutual information was used as a similarity measure and simulated annealing was employed as a searching technique. Butz and Thiran [16] maximized the mutual information of the gradient images.

Among the two classes of automatic image registration techniques, feature-based methods are difficult to generalize, because they are usually based on rules for both identification of features and determination of correspondences. Area-based methods, on the other hand, are free of decision processes and can be easily generalized. However, efficient techniques can be applied only when translation is the only deformation between the analyzed images. The proposed solutions to deal with both translation and rotation are often computationally very expensive [28].

3.2 Proposed Approach

Here, an automatic registration approach based on global optimization techniques is proposed. In particular, in order to estimate the optimum transformation between the input and the base image, a Genetic Algorithm (GA) is used to optimize the match between previously extracted maps of curvilinear structures in the images to be registered (such structures being represented by the vessels in the human retina).

The reference and input images (denoted by I_{ref} and I_{in}, respectively) are previously segmented (e.g., by using the blood vessel extraction approach proposed in Chapter 2 for Retinal Images, RI) in order to extract the correspondent binary feature maps F_{ref} and F_{in}. Such binary images are fed as inputs to an optimization module, aiming at maximizing a suitably defined objective function. In fact, the transformation matrix has to be optimized. Its goodness is evaluated by an objective function that quantifies the matching between the two feature

maps as a function of the unknown transformation (Sec. 3.2). The optimization is achieved here by applying a genetic algorithm. After the optimum matrix has been estimated, it is applied to the original input image, which is translated and interpolated in order to obtain the final registered image. The architecture of the proposed registration process is shown by the block diagram in Fig. 3.1.
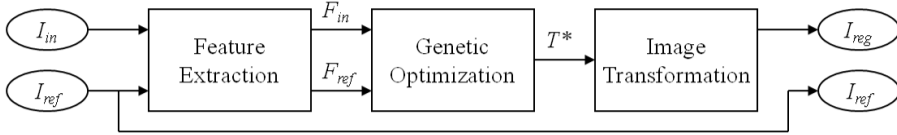
Figure 3.1: Block diagram of the registration process: Both the reference and the input images (I_{ref} and I_{in}) are segmented, in order to obtain their binary vessel maps (F_{ref} and F_{in}), used by the objective function to calculate the measure of match (MOM). The genetic algorithm estimates the optimum transformation (genetic optimization block), which is then applied to the input image, I_{in}, in order to achieve the registered image, I_{reg}.

Measure of Match

After segmentation, two binary feature maps are obtained, F_{in} and F_{ref}, from the input and reference image, respectively. The problem is formulated as determining a transformation T^* such that, when T^* is applied to the first image, F_{in}, the best match with the second one, F_{ref}, is achieved. The problem can be mathematically formulated as the maximization of the following objective function:

$$MOM(T) = \frac{1}{n} \sum_{(i,j):F_{ref}(i,j)\neq 0} F_{in}(T(i,j)), \qquad (3.3)$$

where MOM (Measure Of Match) denotes the objective function, T is the transformation for the i and j coordinates in the image plane, and n

is the number of nonzero pixels of F_{ref} itself. An affine transformation model, which exhibits six independent parameters, is employed.

Equation (3.3) is equivalent to the definition of the correlation function for the binary images F_{in} and F_{ref}. According to the correlation definition, in the binary case, only nonzero pixels from both images contribute to the value of the correlation. The function used, as described in (3.3) is normalized, so that the absolute maximum value is unitary; but in general, the achieved maximum value is significantly lower. The reason is not the optimization method inefficiency, but the fact that the two feature maps are in most of the cases not identical due to noisy pixels and changes.

Genetic Algorithm

The determination of the transformation parameters strongly depends on the objective function, as well as on the images to be registered. The search based methods, provide a solution, based on the optimization of a MOM between the original and the transformed images, with respect to the transformation parameters.

Generally, the MOM has multiple extremes, hence the most attractive search methods are based on global optimization techniques. Here, a genetic algorithm is adopted (as proposed in [118]), since it ensures, under mild assumptions, convergence to a global maximum of the adopted matching functional.

The independent parameters of T are defined over a wide range of values to achieve robustness. The values of the parameters are converted to binary digits and concatenated in a single string, called individual. Each real parameter is encoded as a binary number, with a precision that depends on the number of digits used.

The process begins with the preliminary random definition of the first population individuals and algorithm parameters, as well as of

41

individual and population dimensions (i.e., the number of bits in each string), minimum number or generations, mutation and crossover probabilities. First, the population is evaluated by calculating the fitness of each individual. According to the principle of the survival of the fittest, pairs of fit individuals are selected to recombine their encoded parameters in order to produce offspring, according to the following steps:

1. The fittest individuals are kept in the next generation without being changed, by elitism.

2. The other individuals are selected by tournament selection, according to their fitness. In particular, for each individual a random number r_n is uniformly drawn in [0,1] and the first individual (after sorting) with a cumulative probability above r_n is chosen.

3. Crossover is applied to each pair of individuals with a fixed probability.

4. Mutation is applied to each single individual, with a fixed probability.

In this way a new generation of solutions, which replaces the previous one, is produced. Its fitness is calculated and a new selection is performed, until the convergence of the MOM is achieved [74]. The final transformation matrix is calculated, by decoding the fittest individual of the last population and the input image is registered.

3.3 Conclusions

In this chapter, a technique is proposed that automatically registers pairs of multitemporal images. The registration is achieved by using a method based on a genetic optimization technique.

Before the algorithm can be used to estimate the optimum transformation, the images has to go through a segmentation stage, aimed at obtaining feature maps from which a matching measure (adopted as optimization functional) is extracted. Once the optimum transformation is obtained, it can be used to register the input image respect to the reference one.

The proposed method has been first investigated in order to register multitemporal RIs, by matching the correspondent vessel maps extracted using the approach proposed in Chapter 2. Subsequently, the proposed registration approach has also been applied to the registration of PIs, by matching the feature maps extracted using the methods proposed in Chapter 2.

A manual registration process is carried out for comparison purposes. Further conclusions about performances of the proposed approach will be drawn in Chapter 5, where the experimental evaluation of the registration technique is presented.

Chapter 4

Change Detection

Change detection is the process of identifying differences in the state of an object or phenomenon, by observing it at different times, often through remote sensors [107]. The object, as named in this definition, is meant in a very general and abstract sense: It can be a physical object, as well as a geographical region or a monitored area of an underground station, etc.

In this chapter, the problem of detecting changes in pairs of multi-temporal images is addressed. In particular, two different methods are proposed to detect temporal changes in Retinal Images (RIs) that can occur due to retinopathy.

First, an introduction of the change detection problem is outlined in Section 4.1. Subsequently, an overview of the approaches in the literature is given in Section 4.2. Finally, two novel approaches for change detection in RIs are proposed in Section 4.3.

4.1 Definition

Essentially, change detection involves the ability to extract quantita-tive information about temporal effects using multitemporal data sets,

which express the observations concerning the object/phenomenon under investigation. These observations are typically represented by data (images) of the object/phenomenon, acquired at two or more distinct times. Each image can be a scalar grey level image, as well as a color image, or, in general, a multispectral image (i.e., a vector-valued image, whose components consist of views of the object/phenomenon, corresponding to different acquisition bands).

Hence, given two multispectral, equal sized images I_1 and I_2 of the object/phenomenon, acquired at times t_1 and t_2, respectively ($t_1 > t_2$), the purpose of a change detection algorithm is to identify the difference (i.e., the "changes") between I_1 and I_2. In the simplest case, a change detector is concerned to identify if a change has occurred at a given pixel. In a more sophisticated context, the algorithm may try to draw conclusions about what kind of change has occurred at that pixel. In both cases, the algorithm produces a change map, i.e., an output image CM expressing the changes occurred at each pixel from I_1 to I_2. When the algorithm only detects if a change has happened, the change map is a binary image, where, for instance, a white pixel denotes "change" and a black one denotes "no-change." On the other hand, a discrete multi-level change map is obtained when different typologies of change are taken into account and suitably distinguished from one another.

4.2   Previous Work

Change detection approaches can be divided into two broad families: Supervised and unsupervised. The former family is based on supervised classification methods, which require the availability of a suitable training set for the learning process of the classification algorithm. The latter assumes no training data to be available at any observation date

and usually performs the change detection by transforming the two analyzed images into a single image in which changed areas are emphasized and can be successively detected.

From an operational perspective, in order to generate maps in which "change" and "no-change" classes are discriminated, completely unsupervised approaches are generally preferred, as they do not require the difficult and (time- and possibly cost-) expensive process of training data collection. When using these methods, no prior information about the statistics of the aforesaid classes is available to the classification algorithm.

A significant variety of change detection approaches have been proposed in the literature to deal with change detection in different fields. The traditional approaches to change detection in remote sensing include image differencing [35], image ratioing [81], image regression, Change Vector Analysis (CVA), methods based on Principal Component Analysis (PCA), multitemporal coherence analysis [95], integration of segmentation with multilayer-perceptron and Kohonen neural networks [125], fuzzy-rule-based analysis [61], multisource and multitemporal data fusion [11], spatio-temporal contextual classification [68], [70], and likelihood ratio tests [30], [63].

One of the most widely used change detection method is image differencing, according to which the images acquired at two different dates are subtracted pixel-by-pixel in order to generate a "difference image." This method relies on the assumption that in the "difference image," the values of the pixels associated with changes present values significantly different from those of the pixels associated with unchanged areas. Changes are then identified by analyzing the "difference image."

Another commonly used change detection method is the image ratioing approach, which generates a ratio image by dividing pixel-by-pixel the gray levels at one date by the gray levels at another date.

46

The detection of changes is performed by analyzing the "ratio image." This approach is usually preferred to image differencing when multiplicative noise affects the input images (e.g., in the case of radar or sonar imagery).

Both image differencing and image ratioing involve the critical problem of selecting an optimal threshold value to be applied to the single image that has been generated (i.e., difference or ratio) to separate "change" from "no-change." "Trial-and-error" procedures are typically adopted to this end [37,62,81,107]. Rosin [98,99] surveyed and reported experiments on many different criteria for choosing the threshold at which the image should be binarized. Smits and Annoni [109] discussed how the threshold can be chosen to achieve application-specific requirements for false and misses alarms [93]. However, such manual operations typically turn out to be time consuming. In addition, the quality of their results critically depends on the visual interpretation of the user. The decision rule in many change detection algorithms is cast as a statistical hypothesis test. The decision as to whether or not a change has occurred at a given pixel corresponds to choosing one of two competing hypotheses, corresponding to "change" and "no-change" decisions [53]. In [77], the problem of automating the threshold selection task is addressed by proposing an unsupervised technique that integrates image ratioing with a generalization of the Kittler and Illingworth minimum-error thresholding algorithm (K&I) [56]. The change-detection method (proposed in [76] and [69] with regard to optical remote sensing imagery) that integrates K&I with image differencing is modified in [77] by developing a new version of K&I, which is suited to image ratioing and to the specific non-Gaussian statistics of the analyzed ratio images. There are several methods that are closely related to image differencing and image ratioing. For example, in CVA [12, 13, 29, 65], which is an

approach often used for multispectral images, a feature vector is generated for each pixel in the image by considering several spectral channels. The modulus of the difference between the two feature vectors at each pixel gives the values of the "difference image." Di Stefano *et al.* [111] performed simple differencing on subsampled "gradient images."

Although change detection techniques have been widely explored for remote sensing imagery, few efforts have been undertaken in the temporal analysis of medical images. In particular, only a few methods have been described in the literature for quantifying the dynamic nature of diabetic retinopathy from a time series of images. In [101] the images are compared by computing their difference and the presence or absence of progressive changes is empirically decided.

Berger *et al.* [6] introduced the dynamic flicker animation as a tool for visualizing changes in the retinal fundus. In this method, the two registered images are displayed in rapid succession, usually a few seconds apart. Changed regions in the image appear to flicker, whereas unchanged regions appear steady.

Cree *et al.* [31] defined a region of interest around the fovea, and used matched filtering followed by thresholding and region growing to find the microaneurysms. They also registered images from multiple time points, to study the turnover of microaneurysms. In [32], methods are described to find leakage of fluorescein in blood vessels by looking at restored images from an angiographic sequence over time and finding areas that do not have a particular pattern of intensity changes.

Studies of microaneurysm turnover were also made by Goatman *et al.* [44]. They detected microaneurysms from baseline and follow-up angiograms, registered the images, and categorized the microaneurysms into three classes namely, static, new, and regressed. A disadvantage of these methods was that the processing was limited to a small region of interest centered on the fovea. Sbeh and Cohen [104] segmented drusen

based on geodesic reconstruction algorithms. They used the method to study the evolution of drusen by registering two images that were widely spaced in time. Each of the methods described above studies the changes associated with only one kind of lesion. Furthermore, they are all susceptible to errors in segmentation of the lesions that leads to accumulation of change analysis errors over time.

All the described methods are specific to one type of lesion or region of the retina: The detection is performed by segmenting the lesions in each image and analyzing the segmentation results, instead of directly comparing multi-temporal images. Hence, they are susceptible to errors in change detection resulting from segmentation errors.

A rare example of a study for change detection in RIs was presented in [79]. In that paper, the "change" areas are detected by using a supervised thresholding technique applied to the sum square of the image difference; the detected changes are classified into different typologies by using a Bayesian approach. This method is completely automatic; however, a training set, in which "change" and "no-change" classes are manually labeled, is required for the thresholding process. In a further study [80] the same method was applied for the detection of vascular changes.

4.3   Proposed Approaches

In the application of change detection techniques to RIs, we assume that variations in light due to retinal changes are larger than the variations due to other factors, such as sensor noise, different optical illuminance, differences in field angle or in patient position, etc. [49]. The impact of these "perturbing" factors might be partially reduced through the selection of appropriate data. For instance, problems arising from field angle differences can be dealt with by selecting data acquired at the

49

same angle level set by the ophthalmologist.

Here, we focus on unsupervised approaches, due to the lack of *a priori* information about the shapes and the statistics of the change areas. In particular, two different approaches for change detection in RIs are proposed and compared, through the evaluation of the experimental results (see Chapter 5). The first approach, which lies on the application of an automatic thresholding technique to an appropriate difference image, is presented in Section 4.3.1. In particular, a consolidated approach for change detection in remote sensing data is applied here to RIs. More details can be found in Appendix A. The second approach, which is based on the innovative combination of the previous thresholding technique and a novel multiple classifier approach, is investigated in Section 4.3.2. More details can be found in the paper reported in Appendix B. Both approaches generate a change map. The detected changes can be further classified by a subclassification stage (see Section 4.3.3).

4.3.1 Thresholding Approach

Given the registered RIs I_{ref}^{R} and I_{reg}^{R} of the human retina, acquired during two consecutive medical visits, out purpose is to identify the meaningful differences (i.e., the "changes") that occurred due to retinopathy.

The block diagram in Fig. 4.1 synthesizes the basic steps of the method. After a preprocessing step(described in Section 4.3.1), the two images to be analyzed, having been co-registered, are converted into two grey level images by applying a ratio of their green and red channels (see Section 4.3.1). These two new grey level images are compared in order to generate two further images ("difference images"). The difference images are obtained by subtracting pixel-by-pixel the γ/ρ ratio at the second acquisition date from the γ/ρ ratio at the first date (where γ
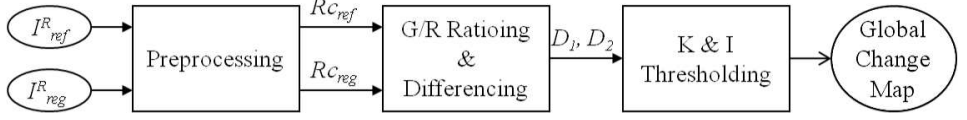
Figure 4.1: Block diagram of the proposed change-detection approach based on K&I.

and ρ denote the green and red channels, respectively). Therefore, in the difference images, pixels associated with retinal changes show grey level values significantly different from those of pixels associated with unchanged areas. Then the proposed algorithm is applied in order to automatically detect the change pixels by using a decision threshold to the histogram of the difference image. The selection of the decision threshold is of major importance, as the accuracy of the final change map strongly depends on this choice. This last step is highly critical in the development of completely automatic and unsupervised techniques for the detection of retinal changes [10].

Both I_{ref}^R and I_{reg}^R are converted to a gray level image by computing the ratios of their green and red channels (see Section 4.3.1). These two new gray level images are compared, pixel by pixel, in order to generate two further images ("difference images") obtained by a pixel-by-pixel subtraction of the reference image from the registered one, and viceversa. A difference image is computed in such a way that pixels associated with retinal changes present gray-level values that are significantly different from those of pixels associated with unchanged areas.

The Kittler and Illingworth thresholding algorithm (K&I) [56] is applied in order to automatically estimate the optimal threshold, based on the analysis of the histogram of the difference image. The threshold is

51

then applied to the difference image, in order to detect the changes. The selection of the decision threshold is of major importance, as the accuracy of the final change-detection map strongly depends on this choice. This last step is highly critical in the development of completely automatic and unsupervised techniques for the detection of changes [10]. Consequently, the algorithm applies again the K&I method to the blue feature in the "change" decision region to distinguish the typology of change that occurred (red vs white spots). We use this unsupervised approach by assigning the "white spot" and the "red spot" labels, when the intensity in the blue feature is above or below the K&I optimal threshold, respectively. In fact, the blue channel of this typology of image data has proven to be effective to distinguish the two classes [78].

Preprocessing Step

Before applying an unsupervised approach to detect changes between two different images, a preprocessing step is usually necessary to make the two images comparable in both the spatial and spectral domains. Concerning the former, the registration has been automatically performed, as described in Chapter 3. With regard to the spectral domain, changes in light, in field angle and in the absorption of the mydriatic drop between the two acquisition times may be potential sources of errors. This problem is mitigated by performing radiometric calibration of the images, here performed by automatic histogram matching [47], based on a linear rescaling.

Furthermore, the detection of the optic disc in the human retina is very important and mandatory for our approach to the detection of exudates, because the optic disc has similar attributes in terms of brightness, color and contrast. The optic disc appears in color fundus images as a bright yellowish or white region. Especially the blue channel of the image acquired at each date turns out to be discriminant for its

detection. In fact, in fundus images, the blue feature is significantly non-zero only in bright regions corresponding to the exudates and the optic disc; the latter can be identified based on its size and shape. The detection and removal of the optic disc has been automatically performed, by using the approach described in Chapter 2.

Consequently, illumination inhomogeneities are corrected by using a homomorphic filtering technique [117]. For Lambertian surfaces, an observed image I_O can be modeled as a composition of a luminance component, Lc, and a reflectance component, Rc (i.e., $I_O = Lc \cdot Rc$). This imaging model holds for RIs due to the diffusive characteristics of the fundus. An exception for this model is the optic disc, which has to be excluded from the computation. The luminance component can be assumed to vary slowly over space, whereas the reflectance component contains also medium and high frequency details [8]. By first applying the logarithm, we transform the multiplicative relation between I_O, Lc and Rc to an additive one, i.e.:

$$log(I_O) = log(Lc) + log(Rc). \qquad (4.1)$$

After applying the logarithm, the image is low-pass filtered, by using a Gaussian filter, and, then, subtracted from the logarithmic original, yielding a high-pass component (i.e., $log(Rc)$). Exponentiation of both high-pass and low-pass components approximately separates the image into luminance and reflectance components. Next processing steps are applied to the latter component.

Feature Transformation

The three RGB channels of fundus images contain different information: The red channel is usually the brightest channel but exhibits a very narrow dynamic range; the green channel has the best contrast (the

edge of retinal features such as exudates, optic disc, and blood vessels are brighter than in the other channels); the blue channel is non-zero mostly in the areas of the optic disc or of the white spots (see also above).

Given the reflectance component of an RGB fundus image $Rc = \{u_{ij} \in \mathbb{R}^3 : i = 0, 1, \ldots, M, j = 0, 1, \ldots, N\}$ of size $M \times N$, in order to generate a gray-level image to be processed, a band ratioing γ/ρ between green channel γ and red channel ρ is applied. Ratioing γ and ρ emphasizes different features. In fact, after the application of this operator, vessels and blood regions are darker than the background while white spots are brighter.

Thresholding Method for Change Detection

In order to automatically detect changes in color RIs, a threshold selection task is addressed by adopting an automatic change-detection technique, which integrates the image-differencing approach (see Section 4.3.1) with a generalization of the K&I's unsupervised minimum-error thresholding algorithm [56].

A thresholding approach is a simple classification procedure involving only one input feature, namely, the grey level of a scalar image. Here, this operator is applied to two "difference images," that are obtained by subtracting pixel-by-pixel the γ/ρ ratio of I_{reg}^R by the one of I_{ref}^R, and viceversa. Adopting this approach, the key issue is to choose the threshold in order to keep the number of misclassified pixels as low as possible. We define the prior probabilities P_1 and P_2 and the parameters of the conditioned probability density functions (pdfs) p_1 and p_2 of the difference image z, conditional to the classes $\omega_1 = $ "no-change" and $\omega_2 = $ "change." Since we operate in an unsupervised fashion, P_1, P_2, p_1, and p_2 cannot be estimated through a training set. As a consequence,

in place of the global intensity pdf of z, i.e.:

$$p_z(Z) = P_1 p_1(Z) + P_2 p_2(Z), \quad Z \in \mathbb{R}, \qquad (4.2)$$

the histogram $\{h(Z), Z = 0, ..., L - 1\}$ of the difference image is computed and utilized (L denotes the number of quantization levels in the difference image). The selection of an appropriate threshold τ is based on the optimization of a given predefined criterion function $J(\tau)$ which averages a cost function $\Sigma(\cdot, \tau)$ over the feature histogram $h(\cdot)$ [26]. Kittler and Illingworth proposed a thresholding algorithm [56], [26] whose cost function is based on the Bayes decision theory. In particular, they adopted the classification rule for minimum error, under the Gaussian assumption for the class-conditional pdfs (i.e., $p_i(\cdot) = N(m_i, \sigma_i^2)$, where m_i and σ_i^2 are the ω_i-conditional mean and variance, respectively; $i = 1, 2$). Under this hypothesis, the only parameters to be estimated are the class prior probabilities P_1 and P_2, the class means m_1 and m_2, and the class variances σ_1^2 and σ_2^2.

According to the MAP (Maximum A-posteriori Probability) rule, which is equivalent to the minimum error rule [39], we need to maximize the posterior probability $P(\omega_i|Z)$ ($i = 1, 2$). This task is formulated by the K&I method in terms of the threshold τ, by introducing the following cost function [56]:

$$\Sigma(Z, \tau) = \frac{[Z - \hat{m}_i(\tau)]^2}{2\hat{\sigma}_i^2(\tau)} - 2 \ln \frac{\hat{P}_i(\tau)}{\hat{\sigma}_i(\tau)}, \qquad (4.3)$$

with $i = 1$ for $z \leq \tau$ and $i = 2$ for $z > \tau$. $\hat{P}_i(\tau)$, $\hat{m}_i(\tau)$ and $\hat{\sigma}_i^2(\tau)$ are histogram-based estimates of the class parameters, which depend on τ

$(i = 1, 2)$ [56]. The resulting criterion function is:

$$J(\tau) = 1 + 2 \sum_{i=1}^{2} \hat{P}_i(\tau) \ln \frac{\hat{\sigma}_i(\tau)}{\hat{P}_i(\tau)}. \qquad (4.4)$$

The optimal threshold τ^* is chosen as to minimize $J(\cdot)$; this aims at minimizing the classification error between ω_1 and ω_2. The behavior of the criterion function is strongly related to the scene characteristics, which are represented by the histogram. Typically, only one minimum is present in the interval $[0, L-1]$, which implies histogram bimodality and reflects the presence of two natural classes (e.g., "change" and "no-change") in the scene.

4.3.2 Multiple Classifier Approach

In order to compensate for the problems due to different angles of illumination in the two acquisitions, which cause local illumination variation not compensated by the homomorphic filtering, an innovative approach based on multiple classifiers is proposed here. In particular, the change-detection method proposed in Section 4.3.1 in integrated within a multiple classifier approach, which combines different spatial classifiers.

The architecture of the proposed multiple-classifier approach is shown by the block diagram in Fig. 4.2. After a preprocessing step(described
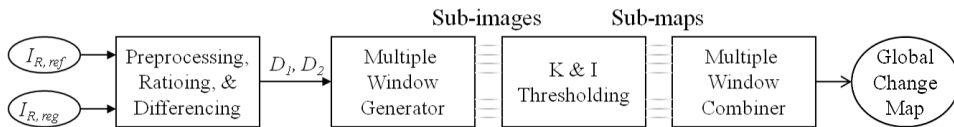

Figure 4.2: Block diagram of the proposed change-detection approach based on multiple classifiers.

in Section 4.3.1), the two images to be analyzed, having been co-registered, are converted into two grey level images by applying the γ/ρ ratio between their green and red channels (see Section 4.3.1). These two new grey level images are subtracted pixel-by-pixel in order to generate two further images ("difference images"). Then, the proposed multiple classifier approach is applied in order to automatically detect the change pixels.

The thresholding approach for the detection of temporal changes (as described in Section 4.3.1) is not applied to the whole difference image but to a set of randomly selected sub-images, which can be considered as single classifiers. Each sub-image is selected by a using a Random Window Generator (RWG). RWG generates square windows in a random way: They are centered in randomly generated pixels, which are uniformly distributed in all the image but the dark background. As a result, the windows partially overlap.

In the adopted multiple classifier voting approach, each window corresponds to a single classifier: The thresholding approach (described in Section 4.3.1) is applied to each sub-image and a change sub-map is obtained. The information stored in each change sub-map needs to be combined in a global change map. For each pixel of the image, all the corresponding classifiers (i.e., the windows that include that pixel) vote for "change" or "no-change" and the classification decision is taken using a weighted sum of the votes. Here, we chose to use a majority vote (i.e., we sum the vote of each classifier with the same weight).

This method compensates for the local differences in illumination between the two images to be compared and improves the accuracy of the change detection, especially in the external regions of the image, which are generally darker and, hence, provide poor information.

The dimension of the windows is an important parameter to set: In fact, the windows should be large enough to completely include each

change area; at the same time, they should be small enough to avoid illumination inhomogeneities. Another parameter to set is the number of windows to be used, which influences the average number of sub-images that include a single pixel. As the number of sub-images per pixel increases, the performance of the method improves.

4.3.3   Subclassification

In a subclassification stage, the change map obtained by applying one of the previous approaches is further classified into different categories, which correspond to the different typologies of change that occurred (red vs white spots). Here, the aim is to detect certain types of pigmentation changes that are clinically relevant for diabetic retinopathy. The considered types of color changes are: Appearing/disappearing red spots, which generally corresponds to the appearance or the disappearance of a bleeding/microaneurysm, and appearing/disappearing white spots, generally due to the appearance or the disappearance of exudates/cotton wool spots (we will refer to these typologies as to new/old red and white spots).

To this end, each pixel is described by a set of features. Here, the feature space consists of the green/red ratio, γ/ρ, and the green channel, γ, for both images. The "white spot" and the "red spot" labels are assigned based on the intensities of these features, which are compared to corresponding thresholds. The architecture of the proposed subclassification step is shown by the block diagram in Fig. 4.3.

The thresholds in this diagram are selected by using an interactive approach, starting from the average values of the corresponding features, which are calculated on the entire image excluding the dark background. A trial-and-error approach is used by varying the threshold, starting from the average value, with an excursion of 30% of the
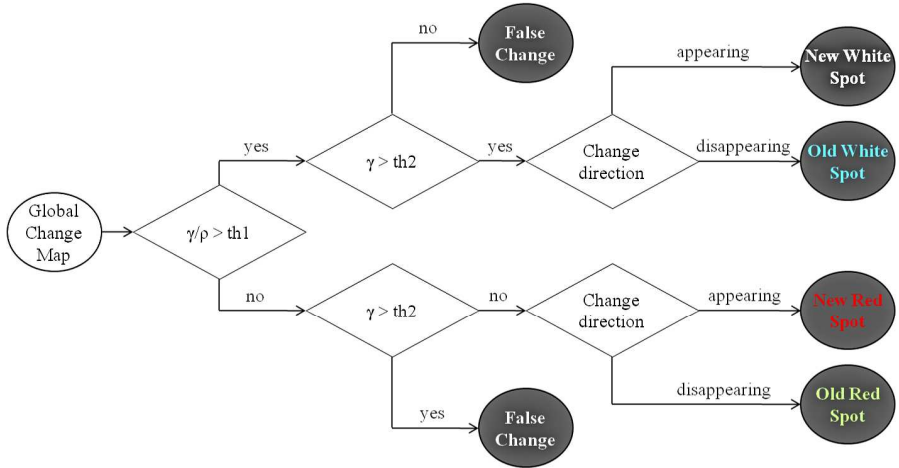
Figure 4.3: Block diagram of the architecture of the proposed subclassification approach.

average value, in order to optimize the results from a visual point of view.

The method proposed here is both simple and interactive: Few parameters have to be set by a human expert. This approach is preferable to a supervised classification, which excludes the data interpretability.

4.4 Conclusions

The purpose, here, is to contribute to the development of a system able to automatically detect temporal changes in color fundus images.

The Kittler & Illingworth's thresholding technique (K&I), which was developed in the context of computer vision and previously applied to change detection problems on other typologies of images [69], [77], is applied here to RIs. The K&I is effective when it is locally applied to the analyzed images. A multiple classifier approach for change detection (based on the K&I applied to randomly selected windows) is proposed

59

to compensate the problem of local illumination inhomogeneities.

Moreover, thresholding is a very fast approach: No iterations are needed, but only the calculation of a criterion function, which is defined for L values (e.g., $L = 256$). Given the histogram, the computation time is also independent of the image size. The use of the multiple classifier approach increases the computational time of the method (from few dozens of seconds per image pair up to about 1 minute) but at the same time makes it more robust.

The subclassification stage, in which temporal changes are classified into different typologies, enables the identification of certain types of pigmentation changes that are clinically relevant for the diagnosis and the monitoring of diabetic retinopathy.

In the future, the multiple classifiers approach could be further investigated. Possible directions could be assigning different weights to the different classifier votes and using windows of variable size to improve the accuracy.

Further conclusions about the performance of the proposed techniques will be drawn in the following chapter, where the experimental evaluation of the proposed change-detection methods is presented.

Chapter 5

Experimental Results

In this chapter the proposed methods for segmentation, registration, and change detection, described in Chapters 2, 3, and 4, are experimentally evaluated. First, the results of planetary image segmentation are presented in Section 5.1. Then segmentation and registration of retinal images are experimentally evaluated in Section 5.2.1. Finally, the experimental results of change detection in retinal images are presented in Section 5.2.2.

5.1   Planetary Images

Experiments were carried out using Mars data, collected both by the THermal EMission Imaging System (THEMIS), an instrument on board the Mars Odyssey spacecraft and by the High Resolution Imaging Science Experiment (HiRISE) camera flying on the Mars Reconnaissance Orbiter (MRO). THEMIS combines a 5-band visual imaging system with a 10-band infrared imaging system [27]. Both visible (VIS) and infrared (IR) THEMIS images, with a resolution of 18 meters and 100 meters per pixel, respectively, were used to test the proposed approach. For the experiments 5 VIS and 7 IR images were selected. Moreover,

9 HiRISE images (HR) were used, with resolution of 0.25 meters per pixel.

Reference data were generated by manually analyzing each image of the data set and identifying all the craters and rocks that are present. Only objects completely included within the images were considered (i.e., objects cut by the borders of the image were discarded). No limits were imposed on the minimum dimensions of the features to be detected. A quantitative assessment of the obtained results by the proposed method was performed using these reference data. This was accomplished by comparing the obtained results with the labeled features in the correspondent Reference Map (RM), by the similarity measure proposed in [103].

The Detection percentage D, the Branching factor B, and the Quality percentage Q were computed as follows:

$$D = \frac{100 \cdot TP}{TP + FN}; \qquad B = \frac{FP}{TP}; \qquad Q = \frac{100 \cdot TP}{TP + FP + FN}, \quad (5.1)$$

where True Positive (TP) is the number of detected features that correspond to labeled objects in RM, False Positive (FP) is the number of features detected by the proposed approach, which do not correspond to any object in RM, and False Negative (FP) is the number of objects in RM that have not been detected by the proposed approach.

5.1.1 Results for Elliptical Feature Extraction

First, the method for the extraction of ellipsoidal features, which was described in Section 2.2.2, is experimentally evaluated.

The global values of D, B, and Q and the total number of TP, FP, and FN obtained by the proposed approach for VIS, IR, and HR data are shown in Table 5.3.

The global values of D for VIS data, IR data, and HR data were

Table 5.1: Average numerical performance of the proposed approach as measured by Detection percentage (D), Branching factor (B) and Quality percentage (Q).

Param	VIS	IR	HR	Overall	Rock	Crater
D	82%	78%	83%	81%	80%	81
B	0.03	0.05	0.06	0.05	0.04	0.07
Q	81%	75%	79%	77%	78%	77%

about 82%, 78%, and 83%, respectively; these high values indicate a good detection rate (because of the high number of TP). B was about 0.03 for VIS, 0.05 for IR, and 0.06 for HR, which indicate a small amount of false detections with respect to the true detections in both cases, thanks to the small number of FP. Finally, relatively high Q values (i.e., about 81%, 75%, and 79% for VIS, IR, and HR, respectively) reflect a good overall algorithm performance. In summary, the overall values of D, B, and Q obtained by testing the proposed approach on all the data sets were about 81%, 0.05%, and 77%, respectively. The same evaluation parameters are also expressed separately for rock and crater detection. The crater detection performance of the proposed approach in terms of D, B, and Q compares favorably with most of the results previously published for automatic crater detection methods [14, 55, 121].

Visual results are shown for a partition of a single band VIS image (Figure 5.1-a). The grey level image is first preprocessed in order to reduce the noise. In particular, Gaussian and median filtering operations are applied in a cascade [106] in order to reduce the noise and, at the same time, preserve the edges. The Canny operator is applied to the smoothed image. Subsequently, in order to extract the rocks, a watershed algorithm is applied to the binary image gradient B. Rock segmentation results are shown in Figure 5.1-b. Then, the generalized

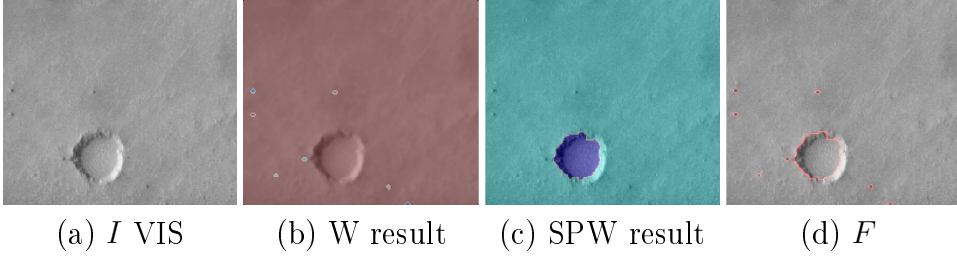(a) I VIS   (b) W result   (c) SPW result   (d) F

Figure 5.1: Experimental results obtained by applying the proposed method to a VIS image. (a) Original image, (b) watershed segmentation applied to B, (c) watershed segmentation, using the maxima of the Hough accumulator as "seed points", and (d) detected features. Each color in the segmentation map denotes a different region.

Hough transform is computed (with $\epsilon = 5°$) and a watershed segmentation is applied, starting the flooding process from the ellipse centers and leading to the detection of the craters. The segmentation results are shown in Figures 5.1-c. Finally, the extracted features, including both rocks and craters, are combined into a binary map and shown in Figure 5.1-d, transparently superimposed to the original image. By a visual inspection, it is possible to appreciate the accuracy of both the detection and the reconstruction of the feature shape.

Visual results are also shown for a partition of the first band of an IR image (Figure 5.2-a). Figure 5.2-b shows the segmentation results when watershed is applied to B. Figure 5.2-c shows the crater segmentation results. The different extracted features are combined and shown in Figure 5.2-d. In this example, not all the features are detected. This is because their contours were not extracted by the Canny operator. A modified edge detection approach which may improve the accuracy of the proposed method is currently under investigation. On the other hand, it is shown below that the detected features are enough to achieve an accurate registration.

Finally, visual results are also shown for different partitions of HR

64

(a) I IR   (b) W result   (c) SPW result   (d) F
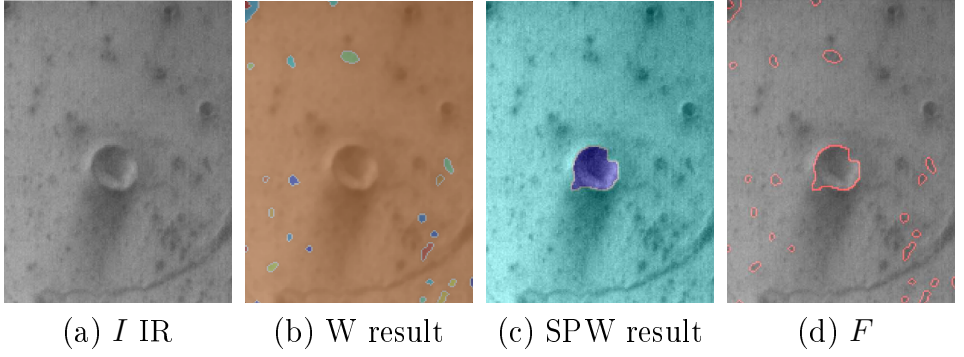
Figure 5.2: Experimental results obtained by applying the proposed method to the first band of an IR THEMIS image.

images. Figures 5.3-a to 5.3-f show the input data and Figures 5.3-g to 5.3-l show the contour maps in red superimposed on the correspondent inputs.

(a) I 1   (b) I 2   (c) I 3   (d) I 4   (e) I 5   (f) I 6

(g) F 1   (h) F 2   (i) F 3   (j) F 4   (k) F 5   (l) F 6
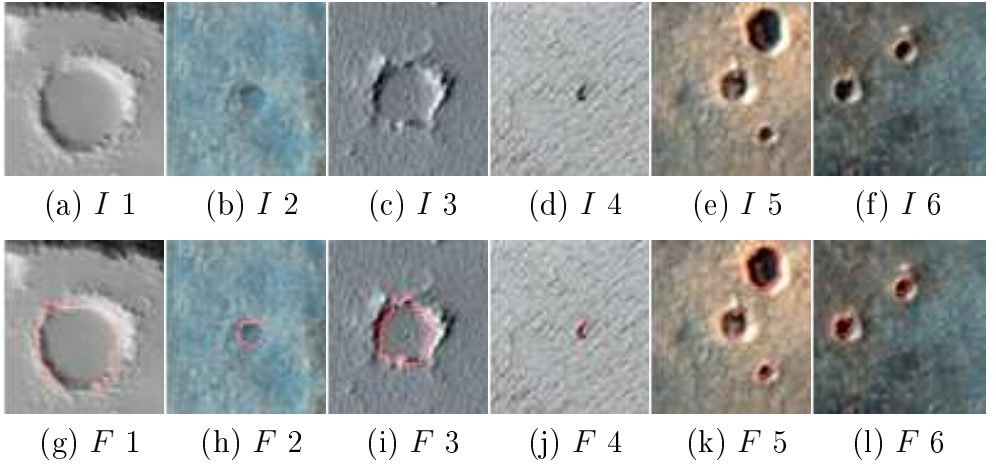
Figure 5.3: Experimental results obtained by applying the proposed method to HR images.

To demonstrate the applicability of the proposed method to registration, two different non-registered bands of an IR image are used as reference I_{ref} and input I_{in} images. In order to show the results, the same
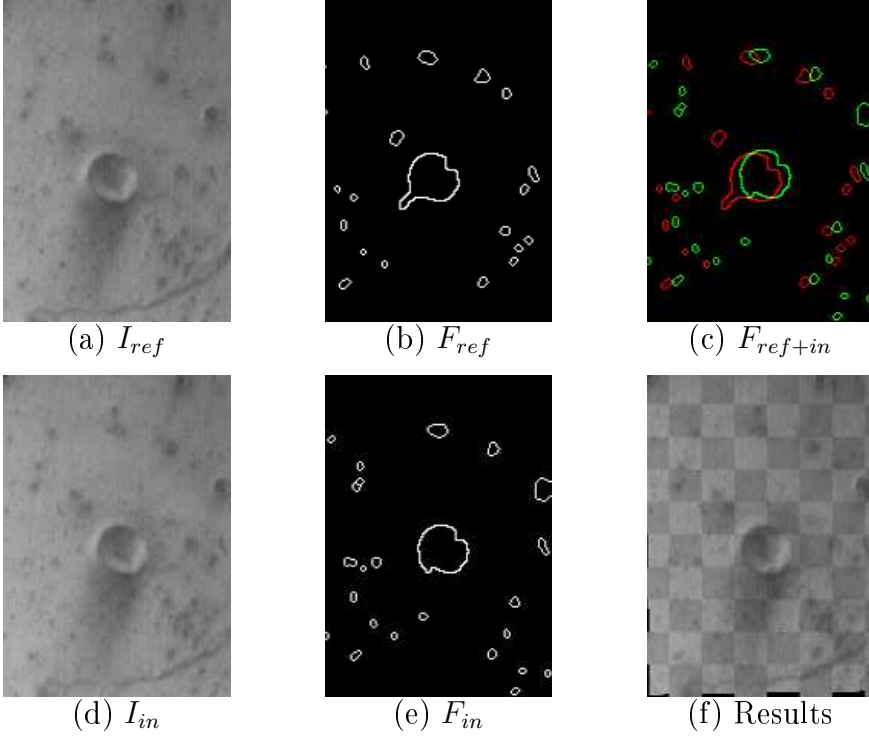
(a) I_{ref} (b) F_{ref} (c) F_{ref+in}

(d) I_{in} (e) F_{in} (f) Results

Figure 5.4: Experimental registration results for a partition of (a) the 4th and (d) the 5th bands of an IR image. (b) and (e) feature contours extracted from (a) and (d), respectively. (c) Feature contours superimposed and represented in a false-color composition (i.e., the green plane is (b), the red plane is (e), and the blue plane is identically zero). (f) Registration results, by using a checkerboard representation.

partition of Figure 5.2-a is used; in particular, the 4th and 5th bands were selected (Figures 5.4-a and 5.4-b, respectively). For both images, craters and rocks are detected and their contours are represented in binary feature images, F_{ref} and F_{in}, as shown in Figures 5.4-c and 5.4-d, respectively. The rotation and translation between the two bands are visible by looking at Figure 5.4-e, in which the two non-registered feature images are superimposed in a false-color representation. The features extracted from I_{ref}, F_{ref}, are represented in green, whereas the I_{in} features, F_{in}, are shown in red. The registration scheme used in this

phase was based on a global optimization technique aimed at estimating the optimum parameters of an image transformation model. The contour images, which represent the features of the two input image bands, were fed as inputs to an optimization module. The transformation matrix was to be optimized: Its goodness was evaluated by an objective function and its optimization was achieved by applying a genetic algorithm [73]. After the optimum matrix was estimated, it was used to transform and interpolate one of the two bands with respect to the other one. The co-registered bands are shown in Figure 5.4-f, by using a checkerboard representation: Each tile of the board represents the registered input band and the reference band, alternately. The registration accuracy can be evaluated by looking at the continuity of the features at the borders of the tiles. The visual analysis of Figure 5.4-f suggests that the registration performed very well; craters and ridges appear continuous at the borders, i.e., the points of overlap.

5.1.2   Results for Crater Detection by MPPs

The method for crater detection, based on a marked point process, which was described in Section 2.2.3, is experimentally evaluated.

In a preliminary evaluation stage, few parameters of the proposed method had to be assigned, concerning both the MPP state space S and the MCMC sampler. Let recall that $S = P \times K$, where $P = [0, M] \times [0, N]$ corresponds to the size of the image (I_g). The resolution r varies for the two different types of images used, hence the total area A of interest is $A = M \cdot N \cdot r^2$ [m^2]. The parameters of K (i.e, a_m, a_M, b_m, and b_M) depend on the size of the objects that need to be detected. In this study, the minimum size for both semi-axes was fixed to 3 pixels (i.e., $a_m = b_m = 3$) and the maximum size to 100 pixels (i.e.,

$a_M = b_M = 100$). The eccentricity e of each object, defined as

$$e = \sqrt{1 - \left(\frac{min(a,b)}{max(a,b)}\right)^2},\qquad(5.2)$$

was constrained to $e \in [0, 0.6]$ (i.e., $min(a,b) \geq 0.8 \cdot max(a,b)$), being craters of bigger e unlikely.

Sampler probabilities needed to be assigned as well. In particular, the global parameters that correspond to the probability of choosing the proposition kernel m were fixed to $p_m = 0.25$, where $m \in \{Tranlation, Rotation, Scaling, Birth\&Death\}$. The probabilities p_B and p_D regulating the birth and death kernel, were fixed to $p_B = p_D = 0.5$.

For comparison purposes, a method for ellipse detection based on a Generalized Hough Transform (GHT) [120] has been implemented and tested on our data set. With this method, for every pair of pixels that were detected as edge points in the Canny gradient and exhibit opposite gradient directions, an accumulator, corresponding to the median point between them in the image plane, is incremented by a unit value. The maxima of the accumulator are taken as centers of ellipses. Then, the three parameters describing the ellipse centered in each detected maximum are computed and a 3D accumulator is used to estimate the two semi-axes and the direction angle of the ellipse from all the pairs of points that contribute to the accumulator in the considered center. The results obtained by the proposed approach and by GHT were compared. This particular approach was chosen for comparison, being a standard technique for the detection of round and elliptical objects, commonly used for crater detection [72], [50], [60], [119].

The global values of D, B, and Q obtained by the proposed approach (MPP) and the standard method used for comparison (GHT) both for

Table 5.2: Average numerical performance of both the proposed approach (MPP) and a standard method (GHT) as measured by Detection percentage (D), Branching factor (B) and Quality percentage (Q).

Data	Method	D	B	Q	Method	D	B	Q
VIS	GHT	73%	0.24	62%	MPP	82%	0.22	71%
IR	GHT	78%	0.14	70%	MPP	89%	0.13	79%
Average	GHT	75%	0.20	65%	MPP	85%	0.18	74%

VIS and IR data are shown in Table 5.2. The global values of D for VIS data and IR data obtained by the proposed approach were about 82% and 89%, respectively. These high values indicate a good detection rate (because of the high number of TP). B was about 0.22 for VIS and 0.13 for IR, which indicate a small amount of false detections with respect to the true detections in both cases, thanks to the small number of FP. The results obtained by applying the proposed approach are more accurate when compared to the performance of the implemented standard technique based on the GHT. In particular, the average value of the detection rate D improved from 75% for the GHT to 85% for the MPP. This is explained by the increase in true detections with respect to the reference map. Similarly, the quality percentage Q. A relatively smaller improvement in the branching factor B is due to the fact that the number of FP was already small when applying GHT.

Moreover, the detection performance of the proposed approach in terms of D, B, and Q also compares favorably with most of the results previously published for automatic crater detection methods [4, 5, 14, 121]. Ideally, the performance of the proposed approach should be compared with the results obtained by the previously published methods when applied to the same data. Unfortunately, the performance of each published approach has been assessed on different sites and distinct types of data (e.g., panchromatic images, topographic data). The most direct performance comparison can be made with the method

proposed by Barata *et al.* in [5]. That approach was tested on images acquired by the Mars Orbiter Camera (MOC). The method in [5] identified 546 craters, with $TP = 171$, $FN = 93$, and $FP = 282$. Hence, the resulting assessment factors were about $D = 65\%$, $B = 1.65$, and $Q = 31\%$. Bandeira *et al.* [4] proposed an unsupervised approach for crater detection from MOC data based on template matching. The average performance indicators fof that approach gave about $D = 86\%$ and $Q = 84\%$. However, they tested their algorithm on images having resolution of 200-300m/pixel. The high performances obtained in [4] may be attributed to the fact that large craters in the sites of analysis have a very regular shape and are relatively easy to identify by template matching. The performance of that approach for the detection of small and irregular craters is unknown. Bue and Stepinski [14] proposed a supervised approach for crater detection from topographic data. The average performance indicators for that approach gave about $D = 74\%$, $B = 0.29$, and $Q = 61\%$. The evaluation factors increased to $D = 92\%$, $B = 0.29$, and $Q = 73\%$ if degraded craters, which the method was not able of detecting, were excluded. That approach is not fully comparable with the proposed method, being supervised. Urbach and Stepinski [121] proposed a supervised approach for crater detection from panchromatic images. The performance factors of their method were about $D = 68\%$, $B = 0.29$, and $Q = 57\%$, when detecting craters of diameter greater that 200m, and lower when taking into account also craters of smaller dimensions. However, a full comparison with our approach is again not possible. In general, the results obtained by the proposed approach are comparable to, and in some cases better than results obtained by methods reported in the literature in terms of the assessment factors. Unfortunately, a full comparison is not possible, because the methods were applied to different data.

Visual results of the feature extraction are shown for the first band

of a visible image (Fig. 5.5(a)). The image is first preprocessed, in order to reduce the noise. In particular, Gaussian filtering and median filtering operations are applied in a cascade [106] in order to reduce the noise and preserve the edges at the same time. The Canny edge detector is applied to the smoothed image and the binary gradient I_g is shown in Fig. 5.5-b. The estimated optimum configuration of the MPP x^*, which identifies the feature contours, is shown in Fig. 5.5-c. The optimum configuration x^* is represented in red, transparently superimposed to the original image. By a visual inspection, it is possible to appreciate the accuracy of the detection, even when many false alarms are present in the binary image gradient I_g. Also the reconstruction of the feature shape is very accurate.

(a) Original image   (b) Image edges   (c) Crater contours

Figure 5.5: Experimental results obtained by applying the proposed method to the first band of a visible image. (a) Original image, (b) Canny gradient, and (c) detected crater contours in red, transparently superimposed to the original image.

Then, visual results obtained by applying the proposed approach to the eighth band of an infrared image (Figure 5.6-a) are presented. In particular, the Canny gradient I_g is shown in Fig. 5.6-b and the estimated x^* is shown in Figure 5.6-c, transparently superimposed to

the original image. The contours of the represented crater appear non-continuous in the binary image gradient I_g, due to the uneven quality of the image. Anyway, the feature is correctly detected and its shape reconstructed.

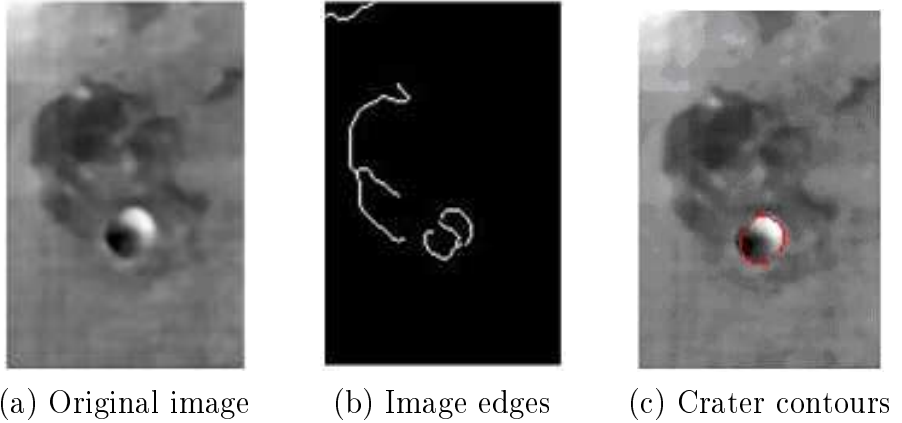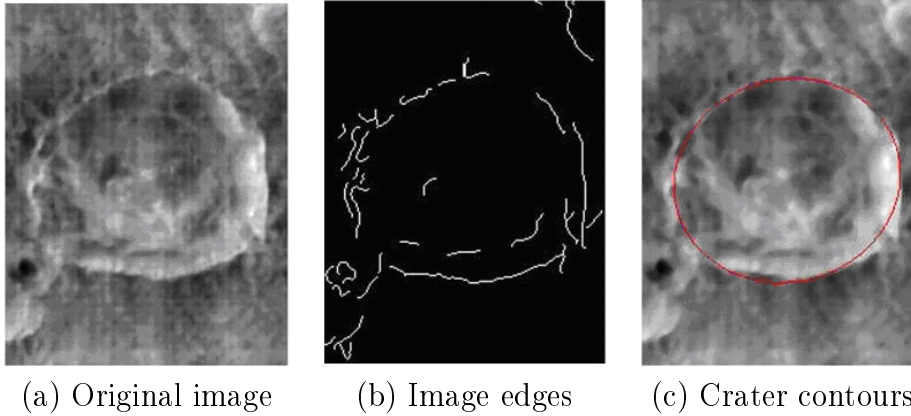(a) Original image   (b) Image edges   (c) Crater contours

Figure 5.6: Experimental results obtained by applying the proposed method to the eighth band of an infrared image. (a) Original image, (b) Canny gradient, and (c) detected crater contours in red, transparently superimposed to the original image.

A visual analysis of the detection results obtained with other planetary images (see Fig. 5.7) confirms that the proposed method is able to correctly identify the location and shape of the imaged craters, even though the input edge map detected only part of the crater borders, included many spurious contours unrelated with the craters, and was severely affected by the shadows in the crater area.

5.1.3 Discussion

Here, the two different methods for planetary feature extraction presented in Chapter 2 have been experimentally evaluated.

Both methods have been tested on different types of images of Mars,

(a) VIS 1   (b) VIS 2   (c) VIS 3   (d) VIS 4   (e) IR 1

(f) Edges 1   (g) Edges 2   (h) Edges 3   (i) Edges 4   (j) Edges 5

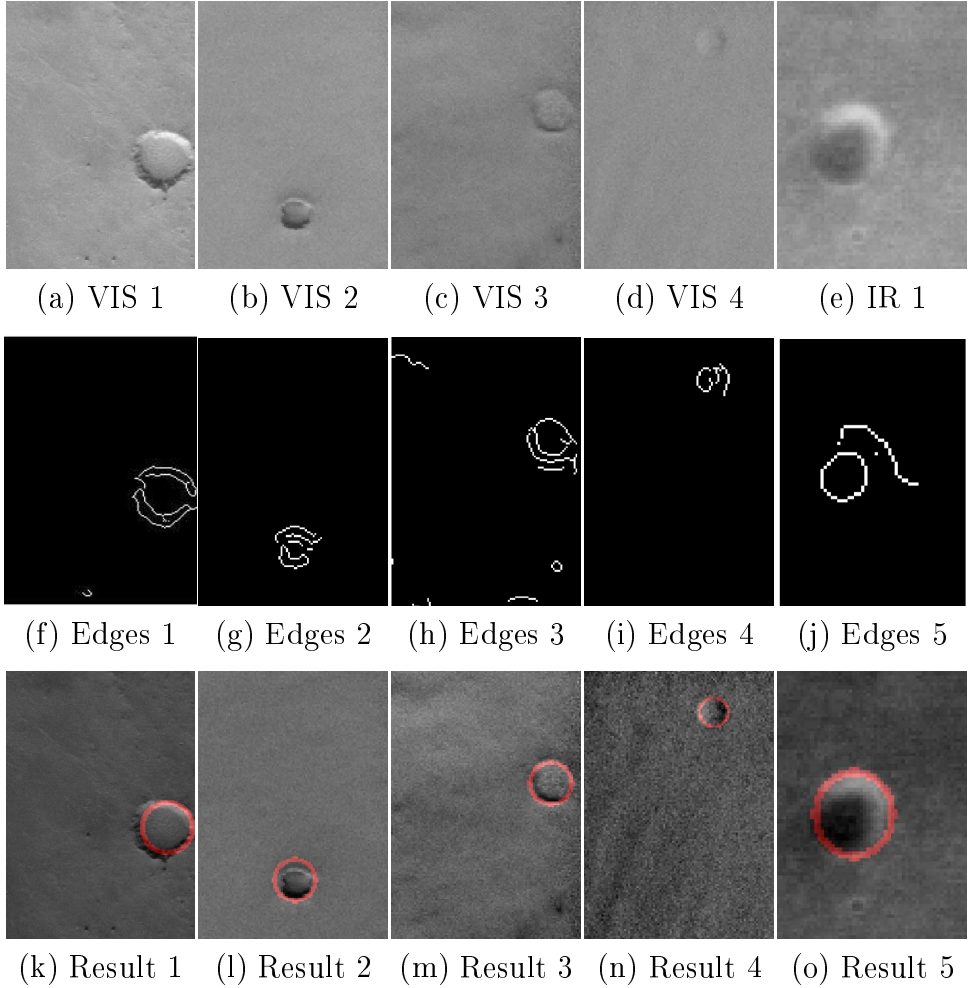(k) Result 1   (l) Result 2   (m) Result 3   (n) Result 4   (o) Result 5

Figure 5.7: Examples of experimental results obtained by the proposed method. (a), (b), (c), (d), (e) Original data, (f), (g), (h), (i), (j) respective edge maps, and (k), (l), (m), (n), (o) detected crater contours in red.

acquired both by the THEMIS and the HiRISE camera. For both approaches, the accuracy of the detection has been assessed by comparison to a manually generated reference map. First, the proposed approach for ellipsoidal feature extraction, based on the Hough transform and the watershed, has been experimentally evaluated. The features to be extracted are not as well contrasted nor defined as for Earth data. However, by applying the proposed approach, small rocks, which are not affected by uneven illumination, can easily be detected. Crater detection is more difficult than rock detection, because of their depth and spatial extent and, consequently, their contours are often blurry and not continuous. Nevertheless, we showed in Section 5.1.1 that their identification can be achieved and the proposed approach provided quite accurate results. The results in terms of several indices based on true and false positives compared favorably to previously proposed approaches. Moreover, it has been shown that the features extracted by the proposed approach can be used to accurately register pairs of images acquired from the same sensor.

The MPP approach has proven to be effective in order to extract elliptical features, such as craters, in planetary images. Again, planetary features are not as well contrasted nor defined as for Earth data. Nevertheless, in Section 5.1.2 it has been demonstrated that their identification can be accurately achieved. The method outperformed a standard method for crater detection based on a generalized Hough transform. Moreover, the obtained results compare favorably to most previously proposed approaches, when performances reported in the literature are considered for the same indices. Finally, a visual inspection of the detection results confirmed that the proposed method was also able to correctly identify the location and shape of the detected craters.

5.2 Retinal Images

Twenty-two images of the posterior pole in which haemorrhages, microaneurysms or exudates are present are selected for analysis. These images of Icelandic patients attending a retinopathy screening service are captured by using a ZEISS FF 450plus IR Fundus Camera, which is connected to a JVC digital camera. The output image is an 8-bit color image of size 1280×1024 pixels. In our testing phases no data on age and ethnicity, duration or type of retinopathy was available. The approaches for registration and change detection, described in Chapters 3 and 4, respectively, have been tested on the 22 fundus multitemporal data sets. As a convention, each data set is named with a consecutive number, with no reference to the corresponding patient for privacy reasons.

5.2.1 Registration Results

This section shows the results of the image registration step. The 22 image pairs to be registered were preprocessed and the vessel maps, of both input and reference image, were extracted. Some differences in the maps, due to different illuminations, determined a low value of matching. Results of the second pair of images are shown in Fig. 5.8; such a pair presents differences in illumination and point of view. Spots also appeared from the first visit to the second one. Consequently, the vessel maps (b) and (c) exhibit large differences, but still the measure-of-match convergence is steadily achieved, as shown in (a). The illumination of the two images is quite different. Therefore, the squares of the checkerboards, shown in (d) and (e), present different intensity values. However, analyzing them in detail, one may note very good vessel continuity in border regions between a square and its neighbors (i.e., where the vessel maps overlap).

Comparable results were achieved for the other image pairs. Automatic registration results are shown for three additional data sets in Fig. 5.8. For all the 22 image pairs, a correct registration was achieved by the proposed method, in spite of a low value of the MOM parameter at convergence.

5.2.2 Change Detection Results

The proposed algorithm for change detection has been tested on the 22 registered image pairs. In order to compare the results obtained by the algorithm with the performance of a human grader, a test map was created for each pair, with the support of a specialist.

For comparison purposes, a method for change detection based on a Bayesian Algorithm (BA) for adaptive change detection proposed in [79] has been implemented and tested on our data set. This method is based on the assumption that the difference values follow a Gaussian distribution. The change map were obtained by comparing the normalized sum square of the differences within a neighborhood [1] (see [79] for more details). The results obtained by the proposed approach and by BA are compared. This particular approach was chosen for comparison, being the only image processing technique proposed in the literature for the detection of retinal changes. Moreover, the results obtained by using the proposed approach based on multiple classifiers (MC) were also compared with the change maps obtained by applying the K&I thresholding technique to the entire image (KEI). The quantitative evaluation of the results in terms of Sensitivity and Specificity obtained by BA, KEI, and MC are shown in Table 5.3. The values of Specificity (Sp) obtained by applying either BA, KEI and MC are generally very high also because the number of true negatives is always high. On the other hand, Sn is more variable because it strictly

76

Table 5.3: Performances of BA, KEI, and MC applied to image pairs, in terms of SnP, Sp, and SnR.

Method	BA	BA	BA	KEI	KEI	KEI	MC	MC	MC
Param.	SnP	Sp	SnR	SnP	Sp	SnR	SnP	Sp	SnR
Average	57%	87%	91%	54%	91%	94%	58%	92%	96%

depends on the quality and similarities in luminance of the input images and is thus affected by sharp differences in the image dynamics at the two dates. The average values of Sensitivity (Sn), assessed both in terms of correctly classified pixels (SnP) and correctly classified regions (SnR), produced by both KEI and the proposed MC method are much higher than the ones obtained by applying BA. Moreover, the MC approach improves the performance in terms of Sn if compared to the values obtained by using the KEI technique. In fact, the use of multiple classifiers avoids the presence of wide false alarm areas, otherwise caused by differences in luminance. In all cases, the values of Sn are higher in the evaluation in terms of regions. In fact, the presence and the position of most "change" areas are correctly detected, even when their shape is not perfectly reconstructed.

The change maps generated by KEI and by the proposed multiple classifier approach when applied to the first data set (Figs. 5.10(a) and (b)) are shown in Figs. 5.10(d)-(e), respectively. Several typologies of change are present in this data set, including new and old spots of both types: The related test map is shown in Fig. 5.10(c). A lower value of Sn is obtained in this case (about 76.5%), due to several missed alarms where edges between "change" and "no-change" are present.

Change detection results obtained by applying MC to the fifth data set (Figs. 5.11(a) and (b)) are also shown in Fig. 5.11(d). The related test map is shown in Fig. 5.11(c).

5.2.3   Discussion

Twenty-two different data sets, including changes of different types of images, including changes of different sizes and typologies, were taken into account in order to test the performances of the method. The proposed approach provided quite accurate results. The accuracy of the registration step, as compared to manual registration, has been evaluated by visual inspection of the results. A correct registration was obtained for all the image pairs with both the automatic and the manual methods.

The results obtained by applying the Kittler & Illingworth thresholding algorithm to the entire image were quite accurate. In fact, accuracy in comparison to human grader has been evaluated on our data base, which comprises images of variable quality. In addition, the proposed multiple classifier approach based on random windows gives more accurate results, meaning that this approach, which locally analyzes the images, proves to be much more robust to differences in illumination.
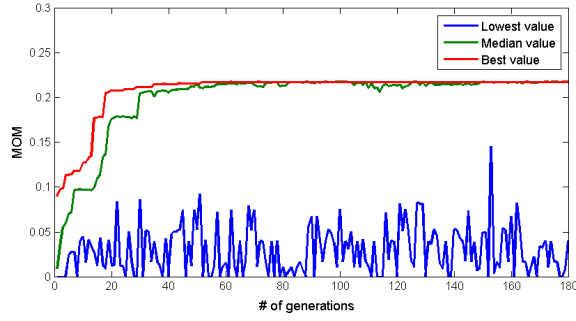
(a) MOM
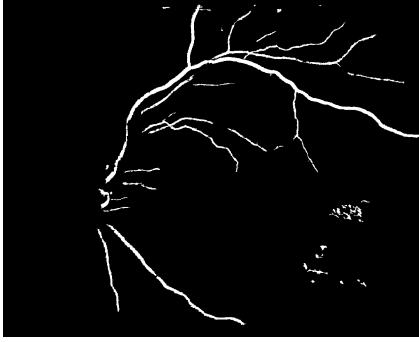
(b) F_{ref}
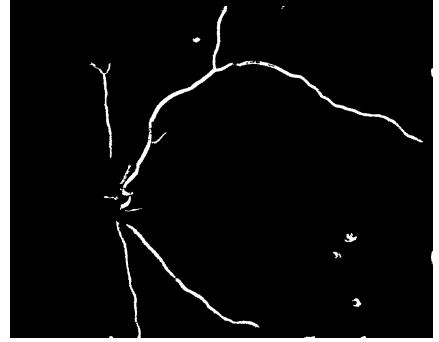
(c) F_{in}
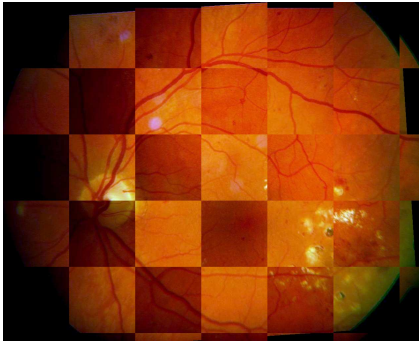
(d) Manual reg.
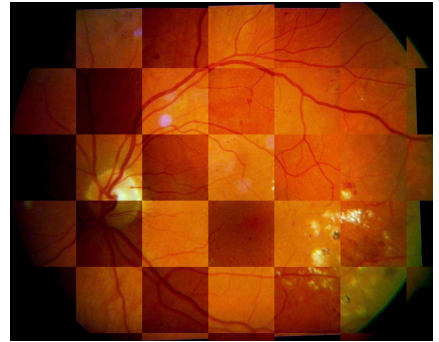
(e) Automatic reg.

Figure 5.8: First data set.(a) Measure Of Match (MOM) of the individuals among the generations, for a population of 50 individuals, with $p_c = 0.5$ and $p_m = 0.01$. The blue, the green, and the red line represent respectively the lowest, the median, and the highest value in the population. Vessel maps of (b) the input and (c) the reference images. (d) Manual and (e) automatic registration of the image pair shown by using a checkerboard representation, in which checkers are alternately taken from the reference and the registered images.

(a) Data set 2   (b) Data set 3   (c) Data set 3
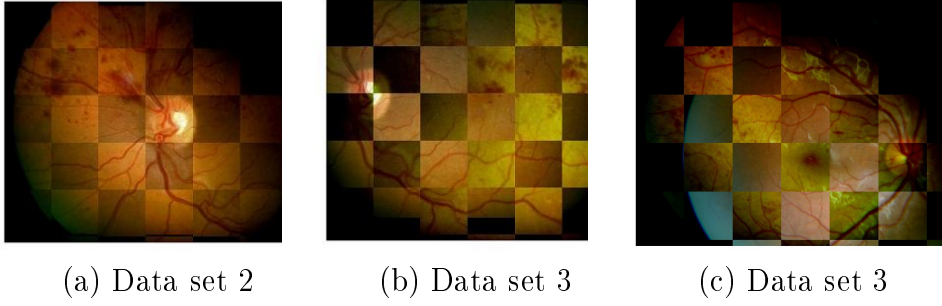
Figure 5.9: Registration results for (a) the second, (b) the third, and (c) the forth data set, shown by using a checkerboard representation.

(a) First Image   (b) Second Image

(c) Test map   (d) KEI map   (e) MC map
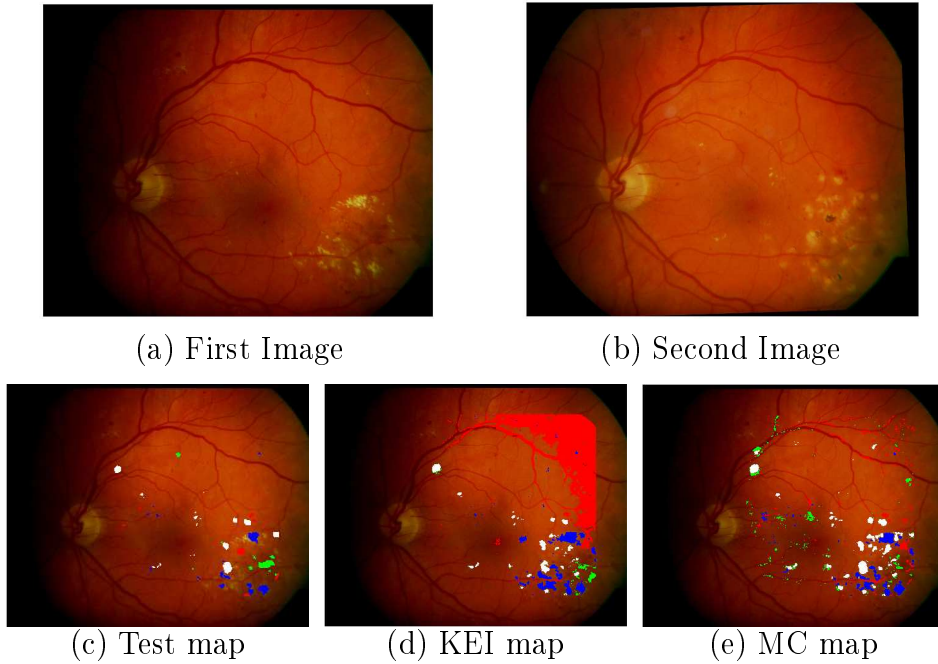
Figure 5.10: First data set: (a) and (b) registered input images acquired from the same eye in June 4, 2003 and in January 24, 2005. (c) Test map, (d) change map generated by KEI, and (e) change map generated by MC. In order to visualize the different change typologies, for each method two change maps are shown, transparently superposed to the first image. Map legend: White = old white spots, red = old red spots, blue = new white spots, green = new red spots, background = "no-change".

(a) First Image

(b) Second Image

(d) Test map

(f) KEI map
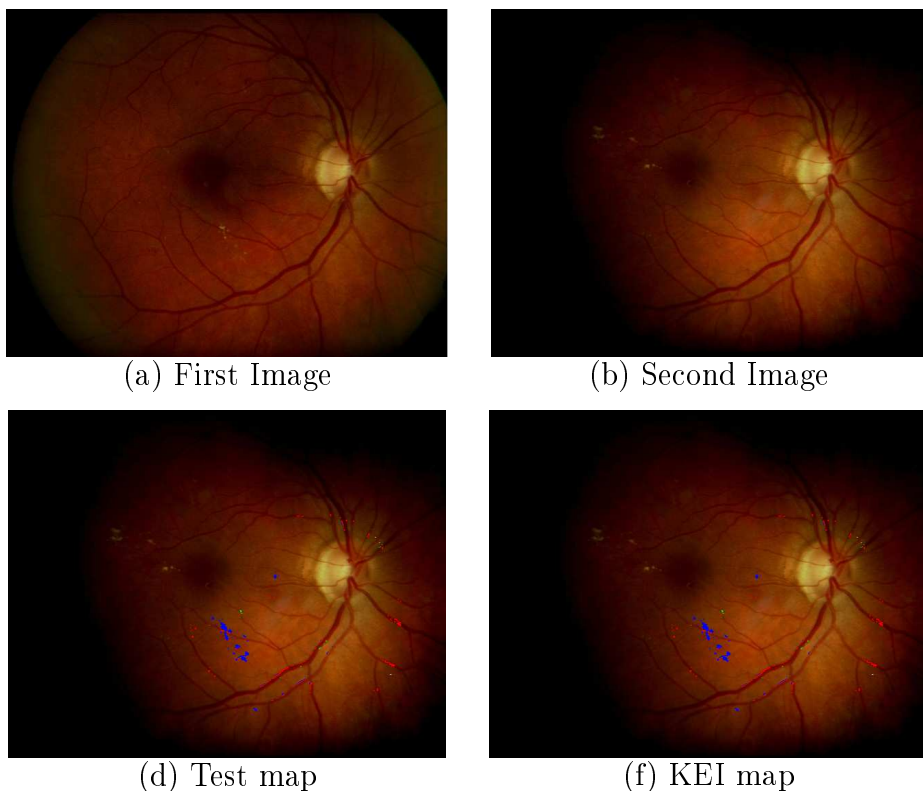
Figure 5.11: Fifth data set: (a) and (b) registered input images acquired from the same eye in acquired on June 6, 2003 and in September 22, 2004, respectively. (c) Test map, (d) change map generated by KEI, and (e) change map generated by MC. In order to visualize the different change typologies, for each method two change maps are shown, transparently superposed to the first image. Map legend: White = old white spots, red = old red spots, blue = new white spots, green = new red spots, background = "no-change".

Chapter 6

Conclusions

Image analysis has become a critical component in contemporary science and technology and has extensive applications, which are continuously expanding through many different areas.

In this thesis, several image analysis problems have been addressed by proposing different image-processing techniques, in order to extract useful information from different typologies of images. The proposed methods aim at providing feasible solutions to several open problems in different fields of image analysis, taking into account the specific issues involved by the typology of data to be analyzed. With the progresses in the image acquisition procedures in all fields, the amount of data available for analysis is continuously increasing. The acquired images need to be analyzed, preferably by automatic processing techniques because of the huge amount of data. Automatic and advanced technique to analyze the data collected are of high relevance.

The next section summarizes the main contributions of this thesis, thus explaining how we met our objectives, and perspectives for future work.

6.1 Contributions and Perspectives

The methodological issues that have been addressed in this thesis are image segmentation, image registration, and change detection of different types of data (i.e., retinal and planetary images). In the following paragraphs, the main conclusions about all the addressed topics are drawn, separately for each type of analyzed data. Detailed comments about each proposed approach can be found in Section "Conclusions" of each of the previous methodological chapters.

Retinal Image Analysis

In diagnostic ophthalmology a multitude of image devices, among which fundus cameras, have been brought into clinical practice. These devices produce a large amount of images that need to be analyzed in order to detect abnormalities.

The problem of analyzing retinal images has been addressed and the aim was to contribute to the development of a system that automatically detects the temporal changes in retinal images, as a support for the diagnosis of retinopathy. To this end, retinal image segmentation has been addressed, in order to identify peculiar structures in the fundus of the eye, such as blood vessels and optic disc. Hence, registration of multitemporal retinal image pairs has been tackled as well. Finally, change detection has been addressed and different approaches have been investigated, in order to detect temporal changes in pairs of registered images acquired during different medical visits.

The main novelty of the proposed system, in terms of application, lies in the proposal of a method that combines an automatic image registration technique and an automatic change detection approach. Pairs of retinal images (taken of the same patient) can be compared and temporal changes, which may occur between different medical visits,

can be detected without the supervision of the ophthalmologists. A specialist will be consulted only in the case that temporal changes are detected by the proposed method.

Moreover, methodologically, a novel approach for change detection, based on multiple classifiers, is proposed here. As far as we know, the idea of combining multiple classifiers with different spatial location, in order to overcome local illumination differences, is new in the contest of multiple classifier approaches and it has demonstrated to be effective when analyzing retinal images.

It is worth noting that the methodologies presented in this thesis were developed and tested in a laboratory operational framework, in which we focused on solving specific problems by proposing innovative and advanced approaches. The applicability of the proposed approaches to the clinical practice would require a further extensive phase of clinical validation, over larger data sets and in close contact with ophthalmologists. Interesting developments would concern addressing such issue in order to further optimize the developed techniques and apply them in the operational context.

Planetary Image Analysis

The growing availability of planetary imagery, collected by several planetary missions, provides a huge potential for the study of the planet surface, but also claims for accurate automatic processing techniques.

The problem of analyzing planetary images has been addressed, as well. In this case, the aim was to contribute to the development of a system that automatically identifies planetary spatial features and reconstructs their shape. In particular, two different methods were proposed, the first one aimed at identifying ellipsoidal features, such as craters and rocks, and a second one specifically aimed at the detection of craters. The proposed approaches represent the first important step

for many applications dealing with all the various data that are being collected by different planetary missions, among which image registration and image analysis, with the aim of selecting safe landing sites, identifying lunar resources, and preparing for subsequent explorations of the Moon and Mars by both robots and humans.

The main contribution of the first method for ellipsoidal feature extraction lies in the proposal of a novel chain, which combines well-known and robust image processing operators in order to achieve accurate results. On the other hand, the main contribution of the second approach is a novel unsupervised method for crater detection, based on a very promising stochastic modeling technique. Indeed, marked point processes provide a powerful and methodologically rigorous framework to efficiently map and detect objects in an image. They have been used in different areas of terrestrial remote sensing, but have been applied here for the first time to planetary image analysis. The use of the proposed approaches provides an accurate analysis of planetary data, which is exploitable and helpful for analysts. Key point is that the methodologies can be applied to different types of optical data.

The application of the proposed methodologies to the analysis of planetary data still presents many open issues, from both an application and a scientific viewpoint. For instance, the methodologies proposed here were developed and tested in a laboratory operational situation. Their applicability in integrated systems to large-scale imagery in operational situations would require an extensive phase of adaptation and optimization of the proposed approaches. In addition, further experimental validation would be required. Interesting developments would concern addressing such open issues, also in order to optimize further the developed techniques, aiming at their practical application in operational context and allowing a further complete assessment of their processing capabilities.

6.2 List of Publications

Papers submitted to Refereed International Journals

1. G. Troglio, J. A. Benediktsson, G. Moser, S. B. Serpico, and E. Stefansson. "Unsupervised Multiple Classifiers for Retinal Change Detection," *Pattern Recognition Letters*, submitted.

2. G. Troglio, J. Le Moigne, J. A. Benediktsson, G. Moser, and S. B. Serpico. "Automatic Extraction of Ellipsoidal Features for Planetary Image Registration," *IEEE Geoscience and Remote Sensing Letters*, submitted.

3. G. Troglio, J. A. Benediktsson, J. Le Moigne, G. Moser, and S. B. Serpico. "Unsupervised Detection of Planetary Craters by a Marked Point Process," *IEEE Trans. on Geoscience and Remote Sensing*, submitted.

Book Chapters

1. G. Troglio, J. A. Benediktsson, G. Moser, S. B. Serpico, and E. Stefansson. "Automatic Registration and Change Detection of Retinal Images," *Multi-Modality Medical Image Segmentation and Registration Techniques* (edited by A. S. El-Baz), Springer-Verlag.

2. G. Troglio, J. A. Benediktsson, G. Moser, and S. B. Serpico "Crater Detection based on Marked Point Processes," *Signal and Image Processing for Remote Sensing*, 2nd edition (edited by Prof. C.H. Chen), CRC Press Publication, in print.

International Conference Papers:

1. G. Troglio, J. A. Benediktsson, G. Moser, and S. B. Serpico. Crater Detection based on Marked Point Processes. *In Proceedings of the 2010 IEEE Geoscience and Remote Sensing Symposium (IGARSS 2010)*, Honolulu, Hawaii, July 25-30, 2010. Selected for the Paper Student Contest (selection rate 20%).

2. G. Troglio, M. Alberti, J. A. Benediktsson, G. Moser, S. B. Serpico, E. Stefansson. Unsupervised Change-Detection in Retinal Images by a Multiple-Classifier Approach. *In Proceedings of the Ninth Workshop on Multiple Classifier Systems (MCS 2010)*, Cairo, Egypt, 2010, pp. 94-103, Springer-Verlag, Berlin 2010. Oral Presentation.

3. G. Troglio, J. A. Benediktsson, G. Moser, S. B. Serpico, E. Stefansson. Automatic Change Detection of Retinal Images. *In Proceedings of the 11th International Conference of the IUPESM Medical Physics and Biomedical Engineering - World Congress 2009*, Munich Germany, Sept. 8-12, 2009, pp. 281-284. Springer-Verlag, Berlin 2009. Oral Presentation.

4. G. Troglio, J. L. Moigne, J. A. Benediktsson, G. Moser, and S. B. Serpico. Automatic extraction of planetary image features. *In Proceedings of the IEEE International Conference on Space Mission Challenges for Information Technology (SMC-IT 2009)*, Pasadena U.S.A., July 19-23 2009, pp. 211-215 (Digital Object Identifier 10.1109/SMC-IT.2009.32). Oral Presentation.

5. G. Troglio, J. A. Benediktsson, S. B. Serpico, G. Moser, R. A. Karlsson, G. H. Halldorsson, and E. Stefansson. Automatic registration of retina images based on genetic techniques. *In Proceedings of the IEEE Engineering for Medicine and Biology Conference,*

Vancouver, Canada, August 20-24 2008, pp. 5419Ũ5424. Oral Presentation.

International Conference Abstracts:

1. G. Troglio, J.A. Benediktsson, G. Moser, S. B. Serpico, and E. Stefansson. Unsupervised Detection of Temporal Changes in Fundus Images. *Association for Research in Vision and Ophthalmology (ARVO 2010)*, num. 3858, Ft. Lauderdale, Florida, USA, May 2-6, 2010. Oral Presentation.

2. G. Troglio, G.H. Halldorsson, R.A. Karlsson, G. Moser, S.B. Serpico, J.M. Beach, E. Stefansson and J.A. Benediktsson. Automatic Registration of Retinal Images Using Genetic Algorithms. *Association for Research in Vision and Ophthalmology (ARVO 2008)*, Inc. 2008, Ft. Lauderdale, Florida, USA, April 27-May 1, 2008. Poster Presentation.

Bibliography

[1] T. Aach and A. Kaup. Bayesian algorithms for adaptive change detection in image sequences using markov random fields. *Signal Processing: Image Communication*, 7(2):147–160, 1995.

[2] K. Akita and H. Kuga. A computer method of understanding ocular fundus images. *Pattern Recognition*, 15(6):431–443, 1982.

[3] V. R. Algazi, J. L. Keltner, and C. A. Jonhson. Computer analysis of the optic cup in glaucoma. *Investigative Ophthalmology and Visual Science*, 26:1759–1770, 1985.

[4] L. Bandeira, J. Saraiva, and P. Pina. Impact crater recognition mars based on a probability volume created by template matching. *IEEE Transactions on Geoscience and Remote Sensing*, 45:4008–4015, 2007.

[5] T. Barata, E. I. Alves, J. Saraiva, and P. Pina. *Automatic Recognition of Impact Craters on the Surface of Mars*, volume 3212. Springer-Verlag, Berlin, Germany, 2004.

[6] J. W. Berger, T. R. Patel, D. S. Shin, J. R. Piltz, and R. A. Stone. Computerized stereo chronoscopy and alternation flicker to detect optic nerve head contour change. *Ophthalmology*, 107:1316–1320, 2000.

[7] S. Beucher. The watershed transformation applied to image segmentation. *Scanning Microscopy Int.*, 6, 1992.

[8] B. Brinkmann, A. Manduca, and R. Robb. Optimized homomorphic unsharp masking for mr grayscale inhomogeneity correction. *IEEE Transactions on Medical Imaging*, 17(2):161–171, 1998.

[9] L. Brown. A survey of images registration techniques. *ACM Computing Surveys*, 24(4), 1992.

[10] L. Bruzzone and R. Cossu. *Analysis of multitemporal remote-sensing images for change detection: Bayesian thresholding approaches*, pages 203–230. in C.H.Chen, Ed., "Geospatial Pattern Recognition",editor: E. Binaghi, P.A. Brivio and S.B. Serpico, Alphen aan den Rijn, Netherlands, 2002.

[11] L. Bruzzone, D. F. Prieto, , and S. B. Serpico. A neural-statistical approach to multitemporal and multisource remote-sensing image classification. *IEEE Transactions on Geoscience and Remote Sensing*, 37:1350–1359, 1999.

[12] L. Bruzzone and D. F. Prieto. Automatic analysis of the difference image for unsupervised change detection. *IEEE Transactions on Geoscience and Remote Sensing*, 38:1171–1182, 2000.

[13] L. Bruzzone and D. F. Prieto. An adaptive semiparametric and context-based approach to unsupervised change detection in multitemporal remote-sensing images. *IEEE Transactions on Image Processing*, 11:452–466, 2002.

[14] B. D. Bue and T. F. Stepinski. Machine detection of martian impact craters from digital topography data. *IEEE Transactions on Geoscience and Remote Sensing*, 45:265–274, 2007.

[15] M. C. Burl, L. Asker, P. Smyth, U. Fayyad, P. Perona, J. Aubele, and L. Crumpler. *Machine Learning*, volume 30, chapter Learning to Recognize Volcanoes on Venus, pages 165–195. Kluwer Academic Publishers, Boston, USA, 1998.

[16] T. Butz and J.-P. Thiran. Affine registration with feature space mutual information. In W. J. Niessen and M. A. Viergever, editors, *Medical Image Computing and Computer-Assisted Intervention*, volume 2208 of *Lecture Notes in Computer Science*, pages 549–556. Springer-Verlag, Berlin, 2001.

[17] A. Can, H. Shen, J. N. Turner, H. L. Tanenbaum, and B. Roysam. Rapid automated tracing and feature extraction from live high-resolution retinal fundus images using direct exploratory algorithms. *IEEE Transactions on Information Technology in Biomedicine*, 3:125–Ű138, 1999.

[18] A. Can, C. Stewart, B. Roysam, and H. Tanenbaum. A feature-based, robust, hierarchical algorithm for registering pairs of images of the curved human retina. *IEEE Transactions on Pattern Analysis and Machine Intelligence*, 24(3):347–364, 2002.

[19] J. Canny. A computational approach to edge detection. *IEEE Transactions on Pattern Anal. Mach. Intell.*, 10(6), 1986.

[20] E. D. Castro, G. Cristini, A. Martelli, C. Morandi, and M. Vascotto. Compensation of random eye motion in television ophthalmoscopy: Preliminary results. *IEEE Transactions on Medical Imaging*, 6:74–81, 1987.

[21] E. D. Castro and C. Morandi. Registration of translated and rotated images using finite fourier transforms. *IEEE Transactions on Pattern Analysis and Machine Intelligence*, 9:700–703, 1987.

[22] F. Cerdat, X. Descombes, and J. Zerubia. Urban scene rendering using object description. In *IEEE International Geoscience and Remote Sensing Symposium*, volume 1, pages 62–64, 2003.

[23] J. Chanussot, G. Mauris, and P.Lambert. Fuzzy fusion techniques for linear features detection in multitemporal SAR images. *IEEE Transactions on Geoscience and Remote Sensing*, 37(3), May 1999.

[24] S. Chaudhuri, S. Chatterjee, N. Katz, M. Nelson, and M. Goldbaum. Detection of blood vessels in retinal images using two-dimensional matched filters. *Medical Imaging, IEEE Transactions on*, 8(3):263–269, 1989.

[25] Y. Cheng, A. E. Johnson, L. H. Matthies, and C. F. Olson. Optical landmark detection for spacecraft navigation. In *13th Annu. AAS/AIAA Space Flight Mech. Meeting*, Feb. 2002.

[26] Z. Chi, H. Yan, and T. Pham. *Fuzzy Algorithms: with Applications to Image Processing and Pattern Recognition*. World Scientific Publishing, Singapore, 1996.

[27] P. Christensen, B. M. Jakosky, H. H. Kieffer, M. C. Malin, H. Y. Mcsween, K. Nealson, G. L. M. S. H. Silverman, S. Ferry, M. Caplinger, and M. Ravine. The thermal emission imaging system for the mars 2001 odyssey mission. *Space Sci. Rev.*, 100:85–130, 2004.

[28] A. V. Cideciyan. Registration of ocular fundus images by cross-correlation of triple invariant image descriptors. *IEEE Engineering for Medicine and Biology Magazine*, 14:52Ű–58, 1995.

[29] J. E. Colwell and F. P. Weber. Forest change detection. In *15th International Symposium on Remote Sensing of Environment*, pages 839–852, 1981.

[30] K. Conradsen, A. A. Nielsen, J. Schou, and H. Skriver. A test statistic in the complex wishart distribution and its application to change detection in polarimetric sar data. *IEEE Transactions on Geoscience and Remote Sensing*, 41:4–19, 2003.

[31] M. J. Cree, J. A. Olson, K. C. McHardy, P. F. Sharp, and J. V. Forrester. A fully automated comparative microaneurysm digital detection system. *Eye*, 11:622–628, 1997.

[32] M. J. Cree, J. A. Olson, K. C. McHardy, P. F. Sharp, and J. V. Forrester. The preprocessing of retinal images for the detection of fluorescein leakage. *Physics in Medicine and Biology*, 44:293–308, 1999.

[33] J. Crespo, J. Serra, and R. Schafer. Theoretical aspects of morphological filters by reconstruction. *Signal Processing*, 47:201–225, 1985.

[34] A. M. Cross. Detection of circular geological features using the Hough transform. *Int. J. Remote Sens.*, 9:1519–1528, 1988.

[35] P. Deer and P. Eklund. Values for the fuzzy c-means classifier in change detection for remote sensing. In *9th International Conference On Information Processing and Management of Uncertainty, IPMU 2002*, pages 187–194, 2002.

[36] X. Descombes and J. Zerubia. Marked point processes in image analysis. *IEEE Signal Proces. Mag.*, 19(5):77–84, 2002.

[37] W. Dierking and H. Skriver. Change detection for thematic mapping by means of airborne multitemporal polarimetric SAR imagery. *IEEE Transactions on Geoscience and Remote Sensing*, 40(3):618–636, 2002.

[38] J. Domingo, G. Ayala, A. Simo, and E. de Ves. Irregular motion recovery in fluorescin angiograms. *Pattern Recognition Letters*, 18:805–821, 1997.

[39] R. Duda, P. Hart, and D. Stork. *Pattern Classification*. 2nd edition, Wiley, New York, 2001.

[40] H. Dunlop, D. Thompson, and D. Wettergreen. Multi-scale features for detection and segmentation of rocks in mars images. In *IEEE Conf. on Compu. Vision and Pattern Recognition*, pages 1–7, 2007.

[41] A. Flores-Mendez. *Crater Marking and Classification using Compu. Vision*, volume 2905. Springer-Verlag, New York, 2003.

[42] M. Foracchia, E. Grisan, and A. Ruggeri. Detection of optic disc in retinal images by means of a geometrical model of vessel structure. *IEEE Transactions on Medical Imaging*, 23:1189–1195, 2004.

[43] C. Geyer and J. Moller. Likelihood inference for spatial point processes. *Stochastic Geometry Likelihood Comput.*, 1998.

[44] K. A. Goatman, M. J. Cree, J. A. Olson, J. V. Forrester, and P. F. Sharp. Automated measurement of m microaneurysm turnover. *Investigative Ophthalmology and Visual Science*, 44:5335–5341, 2003.

[45] M. H. Goldbaum, V. Kouznetsova, B. L. Cote, W. E. Hart, and M. Nelson. Automated registration of digital ocular fundus images for comparison of lesions. In *SPIE Conference on Ophthalmic Technologies III*, volume 1877, pages 94–99, 1993.

[46] M. P. Golombek, R. E. Arvidson, T. Heet, L. Barry, J. R. Matijevic, and A. S. McEwen. Size-frequency distributions of rocks on the northern plains of mars in hirise images with special reference to phoenix landing sites. In *LPSC*, volume 1405, TX, 2007.

[47] R. C. Gonzalez and R. E. Woods. *Digital Image Processing*. Prentice Hall Inc., Englewood Cliffs N.J., second edition, 2001.

[48] P. Green. Reversible jump Markov chain monte carlo computation and Bayesian model determination. *Biometrika*, 82:711Ǔ–732, 1995.

[49] G. H. Haldorsson. *Automatic registration of spectrophotometric retina images*. M.Sc. dissertation in Electrical and Computer Engineering, University of Iceland, 2003.

[50] R. Honda, Y. Iijima, and O. Konishi. Mining of topographic feature from heterogeneous imagery and its application to lunar craters. In S. Arikawa and A. Shinohara, editors, *Progress in Discovery Sci.*, volume 2281 of *Lecture Notes in Compu. Sci.*, pages 27–44. Springer Berlin / Heidelberg, 2002.

[51] A. Hoover and M. Goldbaum. Locating the optic nerve in a retinal image using the fuzzy convergence of the blood vessels. *IEEE Transactions on Medical Imaging*, 22:951–958, 2003.

[52] A. Hoover, V. Kouznetsova, and M. Goldbaum. Locating blood vessels in retinal images by piecewise threshold probing of a

matched filter response. *IEEE Transactions on Medical Imaging*, 19:203–210, 2000.

[53] S. M. Kay. *Fundamentals of Statistical Signal Processing: Detection Theory*. Prentice-Hall, 1993.

[54] J. R. Kim and J.-P. Muller. Impact crater detection optical images and DEM. In *ISPRS*, Houston, TX, 2003.

[55] J. R. Kim, J.-P. Muller, S. van Gasselt, J. G. Morley, and G. Neukum. Automated crater detection, a new tool for mars cartography and chronology. *Photogrammetric Eng. Remote Sens.*, 71(10):1205–1217, 2005.

[56] J. Kittler and J. Illingworth. Minimum error thresholding. *Pattern Recognition*, 19:41–47, 1986.

[57] J. K. Kristinsson, M. S. Gottfredsdottir, and E. Stefansson. Retinal vessel dilatation and elongation precedes diabetic macular oedema. *British Journal of Ophthalmology*, 81:274–278, 1997.

[58] C. Kuglin and D. Hines. The phase correlation image alignment method. In *International Conference on Cybernetics and Society*, pages 163–165, 1975.

[59] M. Lalonde, L. Gagnon, , and M.-C. Boucher. Non-recursive paired tracking for vessel extraction from retinal images. In *Conference Vision Interface*, 2000.

[60] B. Leroy, G. Medioni, A. E. Johnson, and L. H. Matthies. Crater detection for autonomous landing on asteroids. *Image Vision Comput.*, 19:787–792, 2001.

[61] X. Li and A. G. Yeh. Multitemporal sar images for monitoring cultivation systems using case-based reasoning. *Remote Sensing of Environment*, 90:524–534, 2004.

[62] S. C. Liew, S.-P. Kam, T.-P. Tuong, P. Chen, V. Q. Minh, and H. Lim. Application of multitemporal ers-1 synthetic aperture radar in delineating rice cropping systems in the mekong river delta, vietnam. *IEEE Transactions on Geoscience and Remote Sensing*, 36:1412–1420, 1998.

[63] P. Lombardo and T. M. Pellizzeri. Maximum likelihood signal processing techniques to detect a step pattern of change in multitemporal sar images. *IEEE Transactions on Geoscience and Remote Sensing*, 40:853–870, 2002.

[64] J. Lowell, A. Hunter, D. Steel, A. Basu, R. Ryder, E. Fletcher, and L. Kennedy. Optic nerve head segmentation. *Medical Imaging, IEEE Transactions on*, 23(2):256–264, 2004.

[65] W. A. Malila. Change vector analysis: an approach for detecting forest changes with landsat. In *6th Annual Symposium on Machine Processing of Remotely Sensed Data*, pages 326–335, 1980.

[66] R. Martins, P. Pina, J. S. Marques, and M. Silveira. Crater detection by a boosting approach. *IEEE Geoscience and Remote Sensing Lett.*, 6:127–131, 2009.

[67] G. Matsopoulos, N. Mouravliansky, K. Delibasis, and K. Nikita. Automatic retinal image registration scheme using global optimization techniques. *IEEE Transactions on Information Technology in Biomedicine*, 3(1):47–60, 1999.

[68] F. Melgani. Classification of multitemporal remote-sensing images by a fuzzy fusion of spectral and spatio-temporal contextual

information. *International Journal of Pattern Recognition and Artificial Intelligence*, 18:143–156, 2002.

[69] F. Melgani, G. Moser, and S. B. Serpico. Unsupervised change detection methods for remote sensing images. *Optical Engineering*, 41(12):3288–3297, 2002.

[70] F. Melgani and S. B. Serpico. A statistical approach to the fusion of the spectral and spatio-temporal contextual information for the classification of remote sensing images. *Pattern Recognition Letters*, 23:1053–1061, 2002.

[71] F. Mendels, C. Heneghan, and J. P. Thiran. Identification of the optic disc boundary in retinal images using active contours. In *Irish Machine Vision Image Processing Conference*, pages 103–115. Springer Berlin / Heidelberg, 1999.

[72] G. G. Michael. Coordinate registration by automated crater recognition. *Planetary and Space Sci.*, 51:563–568, 2003.

[73] Z. Michalewicz. *Genetic Algorithms + Data Structures = Evolution Programs*. Springer Verlag, Berlin, 3rd edition, 1999.

[74] Z. Michalewicz. *Genetic Algorithms + Data Structures = Evolutiona Programs*. Springer Verlag, Berlin Heidelberg, third edition, 1999.

[75] I. Molloy and T. F. Stepinski. Automatic mapping of valley networks on mars. *Compu. & Geosci.*, 33(6):728–738, 2007.

[76] G. Moser, F. Melgani, and S. Serpico. *Advances in unsupervised change detection*, pages 403–418. in "Frontiers of Remote Sensing Information Processing," editor: C. H. Chen, World Scientific Publishing, Singapore, 2003.

[77] G. Moser and S. Serpico. Generalized minimum-error thresholding for unsupervised change detection from sar amplitude imagery. *IEEE Transactions on Geoscience and Remote Sensing*, 44(10):3695–3705, 2006.

[78] A. Nappo, J. A. Benediktsson, S. B. Serpico, S. J. Joelsson, G. Moser, R. A. Karlsson, G. H. Halldorsson, S. H. Hardarsson, and E. Stefansson. Unsupervised change detection in color fundus images of the human retina. In *Proceedings of the Norsig Conference 2006*, pages 134–137, Reykjavik, 2006.

[79] H. Narasimha-Iyer, A. Can, B. Roysam, C. Stewart, H. Tanenbaum, A. Majerovics, and H. Singh. Automated analysis of longitudinal changes in color retinal fundus images for monitoring diabetic retinopathy. *IEEE Transactions on Biomedical Engineering*, 53(6):1084–1098, 2006.

[80] H. Narasimha-Iyer, A. Can, B. Roysam, H. Tanenbaum, and A. Majerovics. Integrated analysis of vascular and non-vascular changes from color retinal fundus image sequences. *IEEE Transactions on Biomedical Engineering*, 54:1436–1445, 2007.

[81] C. Oliver and S. Quegan. *Understanding Synthetic Aperture Radar Images*. Artech House, Norwood, MA, 1998.

[82] M. Ortner, X. Descombes, and J. Zerubia. A marked point process of rectangles and segments for automatic analysis of digital elevation models. *IEEE Transactions on Pattern Anal. Mach. Intell*, 30(1):105–119, 2008.

[83] A. Osareh, M. Mirmehdi, B. Thomas, and R. Markham. Classification and localisation of diabetic-related eye disease. In A. Heyden, G. Sparr, M. Nielsen, and P. Johansen, editors, *Computer*

Vision, volume 2353 of *Lecture Notes in Computer Science*, pages 325–329. Springer Berlin / Heidelberg, 2006.

[84] T. Pappas and J. Lim. A new method for estimation of coronary artery dimensions. *IEEE Transactions on Acoustics, Speech and Signal Processing*, 36(9):1501–1513, 1988.

[85] E. Peli, R. A. Augliere, and G. T. Timberlake. Feature-based registration of retinal images. *IEEE Transactions on Medical Imaging*, 6:272–278, 1987.

[86] E. Peli and M. Lahav. Drusement measurement from fundus photographs using computer image analysis. *Opthalmology*, 93:1575–1580, 1986.

[87] G. Perrin, X. Descombes, and J. Zerubia. Tree crown extraction using marked point processes. In *EUSIPCO Conf.*, Vienna, Austria, 2004.

[88] G. Perrin, X. Descombes, and J. Zerubia. Adaptive simulated annealing for energy minimization problem in a marked point process application. In *EMMCVPR Conf.*, Saint Augustine, FL, 2005.

[89] G. Perrin, X. Descombes, and J. Zerubia. A marked point process model for tree crown extraction in plantations. In *IEEE ICIP*, pages 661–664, 2005.

[90] R. P. Phillips, T. Spencer, P. G. Ross, P. F. Sharp, and J. V. Forrester. Quantification of diabetic maculopathy by digital imaging of the fundus. *Eye*, 5:130–137, 1991.

[91] P. Pina, J. Saraiva, L. Bandeira, and T. Barata. Identification of martian polygonal patterns using the dynamics of watershed

contours. In A. Campilho and M. Kamel, editors, *Int. Conf. Image Anal. Recognition*, volume 4142 of *Lecture Notes in Compu. Sci.*, pages 691–699. Springer Berlin / Heidelberg, 2006.

[92] A. Pinz, S. Bernogger, P. Datlinger, and A. Kruger. Mapping the human retina. *IEEE Transactions on Medical Imaging*, 17:606–620, 1998.

[93] H. V. Poor. *An Introduction to Signal Detection and Estimation.* Springer-Verlag, 2nd edition, 1994.

[94] M. Quartulli and M. Datcu. Stochastic geometrical modeling for built-up area understanding from a single sar intensity image with meter resolution. *IEEE Transactions on Geoscience and Remote Sensing*, 42(9):1996–2003, 2004.

[95] E. J. M. Rignot and J. J. V. Zyl. Change detection techniques for ERS-1 SAR data. *IEEE Transactions on Geoscience and Remote Sensing*, 31(4):896–906, 1993.

[96] N. Ritter, R. Owens, J. Cooper, R. Eikelboom, and P. V. Saarloos. Registration of stereo and temporal images of the retina. *IEEE Transactions on Medical Imaging*, 18:404–418, 1999.

[97] C. Robert and G. Casella. *Monte Carlo statistical methods.* Springer-Verlag, New York, 1999.

[98] P. Rosin and E. Ioannidis. Evaluation of global image thresholding for change detection. *Pattern Recognition Letters*, 24:2345–2356, 2003.

[99] P. L. Rosin. Thresholding for change detection. *Computer Vision and Image Understanding*, 86(2):79–95, 2002.

[100] W. Rudin. *Principles of Mathematical Analysis.* 2nd edition, McGraw-Hill, New York, 1976.

[101] S. Sakuma, T. Nakanishi, Y. Takahashi, Y. Fujino, S. Ohtsuka, A. Tomono, N. Nakanishi, T. Tsubouchi, and T. Tanino. Image registration, color correction, and change detection based on value of difference in sequential ocular fundus images. *Systems and Computers in Japan*, 37:100–112, 2006.

[102] G. Salamuniccar and S. Loncaric. Method for crater detection from martian digital topography data using gradient value/orientation, morphometry, vote analysis, slip tuning, and calibration. *IEEE Transactions on Geoscience and Remote Sensing*, 48:2317–2329, 2010.

[103] G. Salamuniccar and S. Loncaric. Open framework for objective evaluation of crater detection algorithms with first test-field subsystem based on mola data. *Adv. Space Res.*, 42:6–19, 2010.

[104] Z. B. Sbeh, L. D. Cohen, G. Mimoun, and G. Coscas. A new approach of geodesic reconstruction for drusen segmentation in eye fundus images. *IEEE Transactions on Medical Imaging*, 20:1321–1333, 2001.

[105] J. Serra. *Image Analysis and Mathematical Morphology.* Academic Press, London, 1982.

[106] L. G. Shapiro and G. C. Stockman. *Computer Vision.* Prentice Hall, 2001.

[107] A. Singh. Digital change detection techniques using remotely-sensed data. *International Journal of Remote Sensing*, 10:989–1003, 1989.

[108] C. Sinthanayothin, J. F. Boyce, H. L. Cook, and T. H. Williamson. Automated localisation of the optic disc, fovea, and retinal blood vessels from digital color fundus images. *British Journal of Ophthalmology*, 83:902–910, 1999.

[109] P. Smits and A. Annoni. Toward specification-driven change detection. *IEEE Transactions on Geoscience and Remote Sensing*, 38:1484–1488, 2000.

[110] J. Staal, M. Abramoff, M. Niemeijer, M. Viergever, and B. van Ginneken. Ridge based vessel segmentation in color images of the retina. *IEEE Transactions on Medical Imaging*, 23:501Ũ509, Apr. 2004.

[111] L. D. Stefano, S. Mattoccia, and M. Mola. A change-detection algorithm based on structure and colour. *IEEE Conference on Advanced Video and Signal-Based Surveillance*, pages 252–259, 2003.

[112] C. V. Stewart, C. L. Tsai, and B. Roysam. The dual-bootstrap iterative closest point algorithm with application to retinal image registration. *IEEE Transactions on Medical Imaging*, 22(11):1379–1394, 2003.

[113] S. Tamura, Y. Okamoto, and K. Yanashima. Zero-crossing interval correction in tracing eye-fundus blood vessels. *Pattern Recogn.*, 21:227–233, 1988.

[114] D. Thompson and R. Castano. Performance comparison of rock detection algorithms for autonomous planetary geology. In *IEEE Aerosp. Conf.*, pages 1–9, 2007.

[115] D. Thompson, S. Niekum, T. Smith, and D. Wettergreen. Automatic detection and classification of features of geologic interest. In *IEEE Aerosp. Conf.*, pages 366–377, 2005.

[116] Y. Tolias and S. Panas. A fuzzy vessel tracking algorithm for retinal images based on fuzzy clustering. *Medical Imaging, IEEE Transactions on*, 17(2):263–273, 1998.

[117] D. Toth, T. Aach, and V. Metzler. Illumination-invariant change detection. In *IEEE Southwest Symposium Image Analysis and Interpretation*, pages 3–7, 2000.

[118] G. Troglio, J. A. Benediktsson, S. B. Serpico, G. Moser, R. A. Karlsson, G. H. Halldorsson, and E. Stefansson. Automatic registration of retina images based on genetic techniques. In *Proceedings of the IEEE Engineering for Medicine and Biology Conference*, pages 5419–5424, Vancouver, BC, 2008.

[119] G. Troglio, J. L. Moigne, J. A. Benediktsson, G. Moser, and S. B. Serpico. Automatic extraction of planetary image features. In *IEEE Int. Conf. SMC-IT*, pages 211–215, Pasadena, CA, 2009.

[120] S. Tsuji and F. Matsumoto. Detection of ellipses by a modified Hough transformation. *IEEE Transactions on Comput.*, 27, 1978.

[121] E. R. Urbach and T. F. Stepinski. Automatic detection of sub-km craters in high resolution planetary images. *Planetary Space Sci.*, 57:880–887, 2009.

[122] T. Vinogradova, M. Burl, and E. Mjolsness. Training of a crater detection algorithm for mars crater imagery. In *IEEE Aerospace Conference Proceedings*, volume 7, pages 3201–3211, 2002.

[123] P. Viola and M. Jones. Robust real-time face detection. *Int. J. Compu. Vision*, 57:137–154, 2004.

[124] P. G. Wetzler, B. Enke, W. J. Merline, C. R. Chapman, and M. C. Burl. Learning to detect small impact craters. In *IEEE WACV*, volume 1, pages 178–184, 2005.

[125] R. G. White. Change detection in sar imagery. *International Journal on Remote Sensing*, 12:339–360, 1990.

[126] F. Zana and J. Klein. A multimodal registration algorithm of eye fundus images using vessels detection and hough transform. *IEEE Transactions on Biomedical Engineering*, 18(5):419–428, May 1999.

[127] B. Zitova and J. Flusser. Image registration methods: a survey. *Image and Vision Computing*, 21:977–1000, 2003.

Part II

Collection of Publications

Appendix A

Paper 1

G. Troglio, J. A. Benediktsson, G. Moser, S. B. Serpico, and E. Stefansson. "Automatic Registration and Change Detection of Retinal Images," *Multi-Modality State-of-the-Art Medical Image Segmentation and Registration Methodologies* (edited by A. S. El-Baz), Springer-Verlag.

Chapter 11
Unsupervised Change Detection in Multitemporal Images of the Human Retina

**Giulia Troglio, Jon Atli Benediktsson, Gabriele Moser,
Sebastiano Bruno Serpico, Einar Stefansson**

Abstract. Diabetes is a growing epidemic in the world, due to population growth, aging, urbanization, and increasing prevalence of obesity and physical inactivity. Diabetic retinopathy is the leading cause of blindness in the western working age population. Early detection can enable timely treatment minimizing further deterioration. Clinical signs observable by digital fundus imagery include microaneurysms, hemorrhages, and exudates, among others. In this chapter, a new method to help the diagnosis of retinopathy and to be used in automated systems for diabetic retinopathy screening is presented. In particular, the automatic detection of temporal changes in retinal images is addressed. The images are acquired from the same patient during different medical visits by a color fundus camera. The presented method is based on the preliminary automatic registration of multitemporal images, and the detection of the temporal changes in the retina, by comparing the registered images. An automatic registration approach, based on the extraction of the vascular structures in the images to be registered and the optimization of their match, is proposed. Then, in order to achieve the detection of temporal changes, an unsupervised approach, based on a minimum-error thresholding technique, is proposed. The algorithm is tested on color fundus images with small and large changes.

Keywords Retinal imaging, Change detection, Image registration, Segmentation

G. Troglio
Department of Ophthalmology, University of Iceland, Hjardaragi 6,
107 Reykjavik, Iceland
and
Department of Biophysical and Electronic Engineering, University of Genoa,
Via all'Opera Pia 11a, 16145 Genoa, Italy
e-mail: git2@hi.is

1 Introduction

In ophthalmology, diagnosis of retinal diseases is based on the analysis of the changes in the retina that can occur during time. The analysis of multitemporal images is an important diagnostic tool. Fundus images may be used to diagnose many diseases that affect the vascular structure by revealing the changes that have occurred in it during the period between two consecutive medical visits.

During the last few years an intensified effort has been undertaken in developing tools to assist in the diagnosis of retinopathy [1, 2, 3, 4]. A multitude of image devices have been brought into clinical practice, by facilitating visual access to different parts of the eye. In particular, fundus cameras have been commonly used over the last decades. These devices produce a large amount of images that need to be visually inspected by ophthalmologists to diagnose abnormalities.

Therefore, automatic methods of retina analysis have been acquiring a growing interest in order to support the diagnosis [5]. In particular, the detection of pathologies, such as microaneurysms, hemorrhages, and edema has been addressed.

This Chapter summarizes current research in algorithms for the analysis of multitemporal retinal images. Furthermore, a novel method for image registration and change detection with this type of images is proposed. Registration is a fundamental underlying technology for many prospective applications of retinal image analysis and has been widely explored. It consists in aligning pairs of images, in order to put them into the same coordinate systems: It is thus essential for any further analysis of image series. Lesion detection has been carried out in many different studies by analysing single retinal images. However, a fully unsupervised method for comparison and change detection in multitemporal images has not been presented yet.

Here, an automatic approach for the registration of retinal images, based on optimization techniques, is proposed. The process of image registration can be formulated as a problem of optimization of a functional that quantifies the matching between the original and the transformed image. As the images present clinical changes and differences in illumination and intensity, the optimum matching is not trivial to be achieved. In order to optimize the robustness of the registration method, the matching is not computed between the two images, but between the maps of structures which are present in the images themselves. According to the specific nature of the considered images (portraying portion of the human retina) maps of vessels are adopted for this purpose. The need for an accurate registration with no human interaction, the absence of clear anatomical regions that can be used for reference, and the low quality of the retinal images, suggest the use of a robust global technique to optimize the matching. In this chapter, a genetic algorithm is proposed, since it ensures, under mild assumptions, convergence to a global maximum of the adopted matching functional. In order to preliminarily map the vessels, a simple thresholding is not sufficient, since retinal vessels and background structures are of comparable intensity. Therefore, a preprocessing approach based on the use of morphological techniques is proposed to accomplish the vessel-extraction task.

The adopted technique to detect changes in the registered colour fundus images is based on the unsupervised thresholding method proposed by Kittler and Illingworth (K&I) [6], originally designed for computer vision purposes, and recently extended to multispectral and radar remote-sensing images. The key idea of the method is to model the "change" and "no-change" pixels of a pair of multitemporal images by two Gaussian-distributed classes and to discriminate between such classes by applying a thresholding technique to a suitably defined "difference image". In particular, the K&I method allows the threshold-selection task to be formalized in an unsupervised framework as the minimization of a criterion function was

defined according to the Bayes decision theory. After the change-detection stage, the present work aims at classifying the detected change regions into four different categories of change, which are relevant to diabetic retinopathy, by exploiting two features relevant to the typology of change.

The main body of the chapter starts with background on retinal image analysis and its associated challenges (Section 2). It then proceeds to present an automatic and unsupervised method for registration and change detection in retinal images (Section 3) and to show the results obtained by applying the proposed approaches (Section 4). Finally, concluding remarks are drawn (Section 5).

2 Previous Work

In this section, an overview over the existing methods for temporal analysis of retinal images is presented. In particular, Section 2.1 focuses on temporal registration of retinal images. The problem of change-detection techniques for the support of the diagnosis of retinopathy is addressed in Section 2.2, where an overview over the existing methods for change detection in image processing is given and, then, the application of change detection to the temporal analysis of retinal images is focused on.

2.1 Registration

Registration is fundamental in order to compare images acquired in different conditions. In particular, temporal registration is necessary when analyzing multitemporal images. It is a difficult task in image processing because correspondence problem is not straightforward. As a consequence, several different registration algorithms have been investigated.

The existing registration methods can be classified into two broad groups: interactive and automatic techniques.

Human-interactive methods have been considered as a reference among the existing methods. Human-involvement necessarily achieves neither the highest accuracy nor reproducibility, but it has been used to prevent catastrophic failures, which are possible with automatic registration methods. The earliest studies of image registration in the ocular imaging area were based on a human interaction [7, 8, 9]. However, manual registration is time-consuming, often prone to human error, and requires specialized knowledge.

Automatic registration methods have been widely investigated in the last decades. The existing automatic techniques may be subclassified into different categories based on the image data used, the considered measure of similarity, the selected transformation model, and the method employed for the parameter search [10, 11]. However, in the contest of fundus images, registration techniques can simply be subclassified into feature-based and area-based methods [12].

Feature-based methods are somewhat similar to manual registration. In fact, these techniques are based on the extraction of features in the images to be registered. Features include the vascular structure [13, 14, 15], the optic disc location and boundary [16, 17, 18], and the macula [19]. The ocular blood vessels or their crossing points are commonly used for registration. The registration process is performed by maximizing a similarity measure computed from the correspondences between the extracted features. These approaches assume that feature/point correspondences are available in both images, and their

113

performance largely depends on sufficient and/or reliable correspondences, especially, when the overlapping part of an image pair is very limited or when there are mismatched correspondences. In [20], blood vessels were selected by an adaptive thresholding technique and their correspondence was established by using a sequential similarity detection method. In [21], matched filters were used to detect vessel junctions and correspondences were determined by a local cross-correlation. A group of papers extracted the bifurcations points of the vessels by means of mathematical morphology [22] or Forster detector [23] and then they matched corresponding points. In [24] vascular landmarks are automatically detected and aligned using a hierarchical estimation technique. An iterative method, called dual bootstrap iterative closest point, is presented in [25]: An initial transformation, which is only accurate in a small region (the "bootstrap region") of the mapped image, is estimated and iteratively expanded it into a global transformation estimate.

Area-based techniques are generally based on all pixel intensities within both images to be registered, in order to determine a single best set of transformation parameters for the analyzed image pair. The transformation can be either found by correlation or by optimization, in the spatial or in the frequency domain. Phase correlation [26] has been widely used to estimate translation misalignments, as proposed in [27]. That work was extended in [28] to estimate not only translation but also rotational parameters: Many incrementally rotated images were generated from the original and correlated. In [29], mutual information was used as a similarity measure and simulated annealing was employed as a searching technique. Butz and Thiran [30] maximized the mutual information of the gradient images. In [31], the measure of match (MOM) was proposed as an objective function and different searching techniques were used to achieve its optimization. Nevertheless, the searching space of transformation models (affine, bilinear, and projective) was huge. The greater the geometric distortion between the image pair, the more complicated the searching space.

Between the two classes of automatic image registration techniques, feature-based methods are difficult to generalize, because they are usually based on rules for both identification of features and determination of correspondences. Area-based methods, on the other hand, are free of decision processes and can be easily generalized. However, efficient techniques can be applied only when translation is the only deformation between the analyzed images. The proposed solutions to deal with both translation and rotation are computationally too expensive [12].

2.2 Change Detection

A change-detection problem can be defined as a classification problem in which "change" and "no-change" classes have to be distinguished, given two input images acquired at different times on the same scene or object.

Change-detection approaches can be divided into two broad families: Supervised and unsupervised. The former family is based on supervised classification methods, which require the availability of a suitable training set for the learning process of the classification algorithm. The latter assumes no training data to be available at any observation date and usually performs the change detection by transforming the two analyzed images into a single image in which changed areas are emphasized and can be successively detected.

From an operational perspective, in order to generate maps in which "change" and "no-change" classes are discriminated, completely unsupervised approaches are generally preferred, as they do not require the difficult and (time- and possibly cost-) expensive process

of training data collection. When using these methods, no prior information about the statistics of the aforesaid classes is available to the classification algorithm.

A significant variety of change-detection approaches have been proposed in the literature to deal with change detection in different fields. The traditional approaches to change detection in remote sensing include image differencing [32], image ratioing [33], image regression, Change Vector Analysis (CVA), methods based on Principal Component Analysis (PCA), multitemporal coherence analysis [34], integration of segmentation with multiplayer-perceptron and Kohonen neural networks [35], fuzzy-rule-based analysis [36], multisource and multitemporal data fusion [37], spatio-temporal contextual classification [38], [39], and likelihood ratio tests [40], [41].

One of the most widely used change-detection method is image differencing, according to which the images acquired at two different dates are subtracted pixel-by-pixel in order to generate a "difference image". This method relies on the assumption that in the "difference image" the values of the pixels associated with changes present values significantly different from those of the pixels associated with unchanged areas. Changes are then identified by analyzing the "difference image".

Another commonly used change-detection method is the image ratioing approach, which generates a ratio image by dividing pixel-by-pixel the gray levels at one date by the gray levels at another date. The detection of changes is performed by analyzing the "image ratio". This approach is usually preferred to image differencing when multiplicative noise affects the input images (e.g., in the case of radar or sonar imagery).

Both image differencing and image ratioing involve the critical problem of selecting an optimal threshold value to be applied to the single image that has been generated (i.e.: difference or ratio) to separate "change" from "no-change." "Trial-and-error" procedures are typically adopted to this end [33], [42], [43], [44]. Rosin [45], [46] surveyed and reported experiments on many different criteria for choosing the threshold at which the image should be binarized. Smits and Annoni [47] discussed how the threshold can be chosen to achieve application-specific requirements for false alarms and misses (i.e. the choice of point on a receiver-operating-characteristics curve [48]). However, such manual operations typically turn out to be time-consuming. In addition, the quality of their results critically depends on the visual interpretation of the user. The decision rule in many change-detection algorithms is cast as a statistical hypothesis test. The decision as to whether or not a change has occurred at a given pixel corresponds to choosing one of two competing hypotheses, corresponding to "change" and "no-change" decisions [49]. In [50], the problem of automating the threshold selection task is addressed by proposing an unsupervised technique that integrates image ratioing with a generalization of the Kittler and Illingworth minimum-error thresholding algorithm (K&I) [6]. The change-detection method (proposed in [51] and [52] with regard to optical remote-sensing imagery) that integrates K&I with image differencing is modified in [50] by developing a new version of K&I, which is suited to image ratioing and to the specific nonGaussian statistics of the analyzed ratio images. There are several methods that are closely related to image differencing and image ratioing. For example, in CVA [53], [54], [55], [56], which is an approach often used for multispectral images, a feature vector is generated for each pixel in the image by considering several spectral channels. The modulus of the difference between the two feature vectors at each pixel gives the values of the "difference image". DiStefano et al. [57] performed simple differencing on subsampled "gradient images".

Although change-detection techniques have been widely explored for remote-sensing imagery, few efforts have been undertaken in the temporal analysis of medical images. In particular, only a few methods have been described in the literature for quantifying the dynamic nature of diabetic retinopathy from a time series of images.

In [58], the images are compared by computing their difference and the presence or absence of progressive changes is empirically decided.

Berger *et al.* [59] introduced the dynamic flicker animation as a tool for visualizing changes in the retinal fundus. In this method, the two registered images are displayed in rapid succession, usually a few seconds apart. Changed regions in the image appear to flicker, whereas unchanged regions appear steady.

Cree *et al.* [60] defined a region of interest around the fovea, and used matched filtering followed by thresholding and region growing to find the microaneurysms. They also registered images from multiple time points, to study the turnover of microaneurysms. In [61], methods are described to find leakage of fluorescein in blood vessels by looking at restored images from an angiographic sequence over time and finding areas that do not have a particular pattern of intensity changes.

Studies of microaneurysm turnover were also made by Goatman *et al.* [62]. They detected microaneurysms from baseline and follow-up angiograms, registered the images, and categorized the microaneurysms into three classes, namely, static, new, and regressed. A disadvantage of these methods was that the processing was limited to a small region of interest centered on the fovea. Sbeh and Cohen [63] segmented drusen based on geodesic reconstruction algorithms. They used the method to study the evolution of drusen by registering two images that were widely spaced in time. Each of the methods described above studies the changes associated with only one kind of lesion. Furthermore, they are all susceptible to errors in segmentation of the lesions that lead to accumulation of change analysis errors over time.

All the described methods are specific to one type of lesion or region of the retina: The detection is performed by segmenting the lesions in each image and analyzing the segmentation results, instead of directly comparing multitemporal images. Hence, they are susceptible to errors in change detection resulting from segmentation errors.

A first study for change detection in retinal images was presented in [64]. In that paper, the "change" areas are detected by using a supervised thresholding technique applied to the sum square of the image difference; the detected changes are classified into different typologies by using a Bayesian approach. This method is completely automatic; however, a training set, in which "change" and "no-change" classes are manually labeled, is required for the thresholding process. In a further study [65] the same method was applied for the detection of vascular changes.

3 Methods

The method proposed here for temporal analysis of color fundus images involves two successive processing sequences: The registration of pairs of images acquired at different times and the detection of temporal changes in the registered images. Temporal registration is a fundamental task in the approach. Actually, in general, such a preprocessing step is usually necessary in order to make the two images comparable in the spatial domain, before an unsupervised approach is applied to detect changes in two different retinal images.

In this chapter, an automatic registration approach based on global optimization techniques is proposed (see Section 3.1). In particular, in order to estimate the optimum transformation between the input and the base image, a Genetic Algorithm (GA) is used to optimize the match between previously extracted maps of curvilinear structures in the images to be registered (such structures being represented by the vessels in the human retina). Then, in

order to achieve the detection of temporal changes within the registered images, a fully unsupervised approach, based on a minimum-error thresholding technique, is proposed (see Section 3.2). In particular, K&I thresholding method proposed in [41] is chosen here, since it enables to differentiate "change" and "no-change" areas, by analyzing a suitably defined difference image, with no need of training information about the statistic of the changed areas and since it has already been found effective when applied to change-detection problems with different typologies of input image (i.e., multispectral [51] and synthetic aperture radar [50] remote-sensing images).

3.1 Registration

The vascular structure covers the entire retina and is relatively stable over time. Thus, it appears that a solution to the retinal image registration problem can be driven by using the ocular blood vessels [66]. Some difficulties arise in this process, due to both the surface of the retina, which is curved but not perfectly spherical [67], and the overlap of the images which can be small due to large changes in the viewpoint between images. In fact, during imaging, a patient's pupil is dilated and his/her forehead is held against a harness. Small shifts in the position of the patient's head are likely to induce translations and rotations of the eye. Eye movements, which are incompletely constrained during diagnosis or surgery, are almost exclusively rotational and occur about two axes at rates of up to 180° per second [68]. Significantly, neither axis of rotation is the optical axis. Moreover, except for detached retinas, it may be reasonably assumed that the retina is rigidly attached to the back of the eye. Together, these observations imply that the apparent motion of the retina should be modeled as a general rigid motion. They also imply, however, that some components of the motion (i.e., rotation about the camera's optical axis in particular) will be small [67]. Consequently, an affine transformation, which exhibits six independent parameters, is applied to overlay image pixels.

Hence, the registration approach proposed here considers an affine transformation model, parameterized by a suitable transformation matrix, and a technique to achieve its optimization, following an initial preprocessing stage. The input images to be registered are first preprocessed, in order to obtain binary images, which show the vessel structure. Such binary images are fed as inputs to an optimization module, aiming at maximizing a suitably defined objective function. In fact, the transformation matrix has to be optimized: Its goodness is evaluated by an objective function and its optimization is achieved by applying a GA. When the optimum matrix is estimated, it is applied to the original input image, which is transformed and interpolated in order to obtain the final registered image. In particular, the *nearest neighbor* interpolation method is chosen, being the computationally least demanding and, above all, the data are not modified (i.e., no new gray levels are introduced).

The first step in the proposed automatic registration method is the extraction of the ocular blood vessels. The input and reference images, denoted by I_1 and I_2 respectively, are preprocessed, in order to obtain binary images I_A and I_B, which show the vessel structure. The vessel extraction is addressed here by using morphological operators [69]. Only the green plane, G, of each RGB image is used in the extraction. G is treated as a gray scale image, because it exhibits the best contrast (the edges of blood vessel are clearer) of all the image planes. To extract vessel segments the method proposed in [70] is used because it is simple and fast. It is unsupervised and also involves very few input parameters (apart from the model dimensions, just one double threshold is involved). A pre-filtering operation is needed in order to remove the background noise. Most of the classical noise smoothers are based on an additive model. Actually, for the addressed problem, the useful information lies in anisotropic

structures, and the preprocessing operator has to preserve them as well as smooth the noise. To remove the structures that are lighter than their surroundings, an opening operator (by reconstruction) is applied, with a flat square structuring element. This is a connected operator[1]. Therefore, it does not introduce any new discontinuities in the image. The removal of nonlinear (or too short) darker objects and the preservation of the others are achieved by taking the minimum of all the possible long directional closings. This minimum is computed using linear structuring elements that are successively oriented in every possible direction. The third operation is the morphological extraction, performed to detect vessel-pixels. The remaining linear objects, which are too wide (more than the vessel width), are removed and the desired structures are extracted. The bottom-hat operator, which is the residue between the current image and its closing, with a flat square structuring element is calculated. The only remaining structures are the wide dark features. Any other pixel is set to zero. The final binary decision (vessel pixel or not) is taken by a double thresholding with reconstruction.

In this way, two binary vessel maps, I_A and I_B, are obtained from the input and reference image, respectively. Such binary images are fed as inputs to an optimization module, aiming at maximizing a suitably defined objective function. In fact, the transformation matrix has to be optimized. Its goodness is evaluated by an objective function and its optimization is achieved by applying a GA.

The problem is formulated as the determination of a geometric transformation T^* such that, when T^* is applied to the first image, I_A, the best match with the second one, I_B is achieved. Mathematically, this problem can be expressed as the maximization of the following objective function:

$$MOM(T) = \frac{1}{n} \sum_{(x,y); I_B(x,y) \neq 0} I_A(T(x,y)), \qquad (1)$$

where MOM denotes the objective function, T is the transformation for the x and y coordinates in the image plane, and n is the number of nonzero pixels of I_B.

The objective function in (1) is normalized, so that the absolute maximum value is unitary; but in general, the achieved maximum value is significantly lower. The reason for that is not the inefficiency of the optimization method, but the fact that the two images are in most of the cases not identical due to noisy pixels and changes.

The determination of the transformation parameters strongly depends on the objective function, as well as on the images to be registered. In the case of retinal images, where MOM has multiple extremes, the most attractive search methods are represented by global optimization techniques. In this work, a GA is adopted (as we proposed in [71]), since it ensures, under mild assumptions, convergence to a global maximum of the adopted matching functional. The aim of the GA is to find the value for the transformation parameters, which maximize the objective function [72]. An affine transformation model, which exhibits six independent parameters, is employed. The values of such parameters are defined over a wide range of values to achieve robustness; they are converted to binary digits and concatenated in a single string, called "individual". Each real parameter is encoded as a binary number, with a precision that depends on the number of digits used. The fitness of each individual (i.e., the goodness of the transformation parameters) is estimated by the objective function calculated over its decoded parameters. The match between the registered and the reference image, $MOM(T_i)$, represents the fitness of the i-th individual. The process begins with the preliminary random definition of the first population individuals. The population is evaluated

---

[1] The connected operators are commonly known as binary opening by reconstruction. They consist in removing the connected components of a binary image that are totally removed by erosion and in preserving the other components.

by calculating the fitness of each individual. According to the principle of the survival of the fittest, pairs of fit individuals are selected to recombine their encoded parameters in order to produce offspring, according to the following steps: First a few fittest individuals are kept in the next generation without being changed, by "elitism". Then, the other individuals are selected by a "tournament selection", two-by-two, according to their fitness. Finally, "crossover" and "mutation" are applied to each pair of individuals with a fixed probability. In this way, a new generation of solutions, which replaces the previous one, is produced: The fitness of the new generation will be calculated and a new selection will be performed, until the convergence of the *MOM* is achieved. At that point the process ends. The final transformation matrix T^* is calculated by decoding the fittest individual of the last population and the input image is registered.

3.2   Change Detection

Given two registered images I_1 and I_2, acquired at times t_1 and t_2, respectively ($t_1 < t_2$), the purpose of change detection algorithms is to identify the meaningful differences (i.e., the "changes") between them.

Here, an unsupervised approach is chosen due to the lack of *a priori* information about the shapes and the statistics of the change areas. Each of the two registered images to be analyzed is converted in a gray-level image by computing the ratios of its green and red channels, *G/R*. These new gray-level images are compared, pixel-by-pixel, in order to generate two further images ("difference images") obtained by a pixel-by-pixel subtraction of the first date image from the second date one, and vice versa. A "difference image" is computed in such a way that pixels associated with retinal changes present gray level values that are significantly different from those of pixels associated with unchanged areas. The K&I algorithm is applied in order to automatically detect the change pixels by applying a decision threshold to the histogram of each "difference image". The selection of the decision threshold is of major importance, as the accuracy of the final change-detection map strongly depends on this choice. This last step is highly critical in the development of completely automatic and unsupervised techniques for the detection of retinal changes [73]. Consequently, the algorithm applies again the K&I method to the ratio of green and red channels, *G/R*, in the "change" decision region to distinguish the typology of change that occurred (red vs. white spots). We use this unsupervised approach by assigning "white spot" and "red spot" labels, when the intensity in *G/R* is above or below the K&I optimal threshold, respectively. In fact, this feature has proven to be effective to distinguish the two classes in this typology of image data (see Section 3.2.2).

3.2.1   Preprocessing

Changes in light, in field angle, and in the absorption of the mydriatic drop between the two acquisition times may be potential sources of errors. This problem is mitigated by performing first a radiometric calibration of the images.

Then the optic disc, which appears in color fundus images as a bright yellowish or white region, has to be identified and removed from the two acquisitions. It is important to remove the optic disc for accurate change detection because it has similar attributes to the exudates in terms of brightness, color, and contrast. Furthermore, its detection is a first step in understanding ocular fundus images: the diameter determines approximately the localization

of the macula [74] the center of vision, which is of great importance as lesions in the macular region affect vision immediately.

The optic disc is the entrance of the vessels and the optic nerve into the retina. It appears in color fundus images as a bright yellowish or white region. Its shape is more or less circular, interrupted by the outgoing vessels. Sometimes the optic disc has the form of an ellipse because of a consistent angle between the image plane and the object plane. Sometimes, the optic disc is even not visible entirely in the image plane, and so the shape is far from being circular or even elliptic.

Here, the optic disc is localized by identifying the area with the highest variation in intensity of adjacent pixels [75]. In fact, the appearance of the optic disc region is characterized by a relatively rapid variation in intensity: The gray-level variation in the papillary region higher than in any other part of the image, because the "dark" blood vessels are beside the "bright" nerve fibres. The variance of intensity of adjacent pixels is used for the localization of the optic disc. In particular, the maximum of the variance image is considered as an estimate of the optic disc center.

3.2.2 Feature Ratio

After a preprocessing step, the two co-registered and radiometrically corrected images to be analyzed are converted in a gray-level image by ratioing different features, in order to emphasize the structures of interest. The three RGB channels of fundus images contain different information: The red channel, R, is usually the brightest channel representing the luminance value but has a very small dynamic range. The green channel, G, has normally the best contrast (the edge of retinal features, such as exudates, optic disc, and blood vessel are clearer than in the other channels) and the blue channel B is present mostly where there are the optic disk or the white spots.

Given the RGB fundus image, I_i, acquired at each considered time t_i, and denoting by G_i, R_i, and B_i the three related channels, a pixel-wise band ratioing between G_i and R_i is applied ($i = 1, 2$). By ratioing these two features, a new gray-level image G_i/R_i is obtained, in which the structures of interest are emphasized. In fact, after the application of this operator, vessel and blood regions are darker than the background, while white spot are brighter.

3.2.3 Thresholding

In order to automatically detect changes in color fundus images, a threshold selection task is addressed. An automatic change-detection technique is proposed, which integrates an image differencing approach with a generalization of the Kittler and Illingworth's unsupervised minimum-error thresholding algorithm (K&I) [41].

A thresholding approach is a simple classification procedure involving only one input feature, namely, the gray level of a scalar image. Adopting this approach, the key issue is to choose the threshold in order to keep the number of misclassified pixels as small as possible, i.e., to select an optimal threshold, according to some appropriate criterion. In a supervised context, this optimal threshold can be easily computed through some decision rule, given the class-conditional probability density function (pdf) of each class [64]. On the contrary, unsupervised threshold selection is a nontrivial task.

Let the pixel intensities in the difference image be modeled as independent samples drawn from a random variable z. We operate in an unsupervised fashion; therefore, the prior

probabilities $P_i = P(\omega_i)$ $(i=1,2)$ of the classes ω_1= "change" and ω_2 = "change", as well as the pdfs $p_i(\cdot) = p_z(\cdot \mid \omega_i)$ of z, conditioned to the two classes (i = 1, 2), are neither known in advance nor can be estimated through a training set. As a consequence, in place of the unconditional gray-level pdf:

$$p_z(Z) = \sum_{i=1}^{2} P_i p_i(Z), \quad Z \in R, \qquad (2)$$

the histogram $\{h(Z) : Z = 0, 1, ..., L - 1\}$ of the difference image is used (L being the related number of quantization levels).

The selection of an appropriate threshold τ is formalized by K&I as the optimization of a predefined criterion function $J(\tau)$ which averages a cost function $c(\cdot, \tau)$ over the feature histogram $h(\cdot)$ [76]. More formally, the threshold is assumed to be fixed at some value $\tau \in \{0,1,...,L-1\}$, and the corresponding decision regions

$$\begin{cases} R_1(\tau) = [0, \tau] \\ R_2(\tau) = [\tau+1, L-1] \end{cases} \qquad (3)$$

are introduced.

A real-valued cost function $c(\cdot, \tau)$ is defined in such a way that $c(Z, \tau)$ measures the cost of classifying a pixel with gray level Z (Z = 0, 1, …, L – 1), by comparing Z with the threshold τ. Then, a criterion function is defined as an histogram-based estimate of the average cost $E\{c(z, \tau)\}$, i.e.:

$$J(\tau) = \sum_{z=1}^{L-1} h(z) c(z, \tau). \qquad (4)$$

Thus, the optimal threshold is defined as the minimum-average-cost threshold, i.e.:

$$\tau^* = \arg \min_{\tau=0,...,L\ 1} J(\tau). \qquad (5)$$

Depending on the specific model adopted for the cost function, several different algorithms can be formalized according to this framework [51], such as K&I, the Huang and Wang's algorithm [77], or the Otsu's method [78]. Here, K&I is adopted, since it was found more effective when applied to change-detection problems in other image-processing fields [50].

The K&I cost function is based on the Bayes classification rule, under Gaussian assumptions for both class-conditional pdfs. Under this hypothesis, the only parameters to be estimated are the class prior probabilities P_1 and P_2, the class-conditional means m_1 and m_2, and the class-conditional variances σ_1^2 and σ_2^2. These parameters are defined as follows:

$$\begin{cases} P_i = P(\omega_i) \\ m_i = E\{z \mid \omega_i\} \\ \sigma_i^2 = E\{(z - m_i)_2 \mid \omega_i\}. \end{cases} \qquad (6)$$

Given the threshold τ, these quantities are estimated by K&I in a histogram-based fashion. Specifically, the prior probability estimate is defined simply as the relative frequency of the pixels above and below the threshold value τ, i.e:

$$\hat{P}_i(\tau) = \sum_{z \in R_i(\tau)} h(z). \qquad (7)$$

Similarly, estimates for the class means and variances are computed from the decision regions in (3):

$$\begin{cases} \hat{m}_i = \dfrac{1}{\hat{P}_i} \sum_{z \in R_i(\tau)} z h(z) \\ \sigma_i^2 = \dfrac{1}{\hat{P}_i} \sum_{z \in R_i(\tau)} [z - \hat{m}_i]^2 h(z). \end{cases} \qquad (8)$$

Hence, given the normality assumptions, conditional pdf estimates are derived ($i = 1, 2$):

$$\hat{p}_i(z,\tau) = \frac{1}{\hat{\sigma}(\tau)\sqrt{2\pi}} \exp\left\{ -\frac{[z - \hat{m}_i]^2}{\hat{\sigma}^2(\tau)} \right\}. \qquad (9)$$

The employed cost function is defined in connection to the Bayes decision theory (hence, the K&I method is also named minimum-error thresholding). Based on the maximum a-posteriori probability (MAP) rule, we should assign each a pixel with grey level Z to the class ω_i corresponding to the maximum posterior probability $P(\omega_i | z = Z)$ ($i = 1, 2$). This task can be formulated in terms of the threshold τ, by introducing the following cost function:

$$c(Z,\tau) = \frac{[Z - \hat{m}_i(\tau)]^2}{2\hat{\sigma}_i^2(\tau)} - 2\ln\frac{\hat{P}_i(\tau)}{\hat{\sigma}_i(\tau)} \quad i = \begin{cases} 1 & \text{for } z \leq \tau \\ 2 & \text{for } z > \tau \end{cases}, \qquad (10)$$

which depends on the threshold parameter τ.

The criterion function resulting from the cost function is:

$$J(\tau) = 1 + 2\sum_{i=1}^{2} \hat{P}_i(\tau) \ln\frac{\hat{\sigma}_i(\tau)}{\hat{P}_i(\tau)}. \qquad (11)$$

and the optimal threshold τ^* is correspondingly chosen as to minimize $J(\tau)$, i.e., as the minimum-error threshold.

According to its definition, $J(\tau)$ is indirectly related to the amount of overlap between the pdf estimates. In fact, these estimates are computed from the class-conditional mean and variance estimates, which are obtained through a histogram truncation at the threshold value τ. But, although the histogram is truncated at τ, the model pdfs $\{\hat{p}_i(\cdot,\tau) : i = 1,2\}$ overlap the same. Actually, the smaller is the overlap, the better is the fit between the data (i.e., the histogram) and the model (i.e., $\hat{p}_1(\cdot,\tau)$ and $\hat{p}_2(\cdot,\tau)$). Moreover, the average classification error is measured by $J(\tau)$, hence, a smaller overlap also implies a lower classification error

In addition, due to the histogram truncation, the tails $\{\hat{p}_1(\cdot,\tau) : Z \leq \tau\}$ and $\{\hat{p}_2(\cdot,\tau) : Z > \tau\}$ of the real conditional pdfs are ignored during the estimation procedure and then they do not

influence the cost and criterion function, at all. As a consequence, the optimal K&I estimates $\left\{\hat{P}_i(\tau^*), \hat{m}_i(\tau^*), \hat{\sigma}_i(\tau^*) : i = 1,2\right\}$ should be considered as biased estimates of the real statistical parameters $\left\{P_i, m_i, \sigma_i : i = 1,2\right\}$. The optimal model pdfs $\left\{\hat{p}_i(\cdot, \tau^*) : i = 1,2\right\}$ are biased estimates of the real ones $\left\{p_i(\cdot) : i = 1,2\right\}$, and, consequently, τ^* is an approximation of the true optimal threshold which could be computed if the true class-conditional pdfs were known.

The criterion function behavior is strongly related to the scene characteristics, which are represented by the histogram. Typically, only one minimum in the interval $[0, L-1]$ implies histogram bimodality, which reflects the presence of two natural classes (e.g., foreground and background, "change" and "no-change") in the scene. In this case, the minimum point for $J(\tau)$ is the optimal threshold τ^*. Correspondingly, the absence of internal minima of $J(\tau)$ in $[0, L-1]$ suggests that the image is homogeneous. Specifically, the output classification map would contain a single class. This behavior is correct from a classification point of view; in fact, a homogeneous image does not exhibit more than one natural class and should not be split according to two classes.

4 Experimental Results

The proposed algorithms have been tested on multitemporal fundus images (RGB 8-bit color images of size 1280×1024 pixels), captured at different times by using a ZEISS FF 450plus IR Fundus Camera with VISUPAC/System 451, which is connected to a JVC digital camera. The images were taken in the same visit or in different dates from Icelandic patients attending a retinopathy screening service and can present haemorrhages, microaneurysm, or exudates. Accordingly, images acquired during the same medical visit are not expected to include changes, whereas changes may be present among different images taken at different times. In our testing phases, no data on age and ethnicity, duration, or type of retinopathy were available.

Here, the proposed methods are experimentally evaluated. In particular, the experimental results obtained by using the proposed approaches for registration and change detection are presented and compared, in Section 4.1 and 4.2, respectively.

4.1 Registration Results

The proposed algorithm for registration has been tested on the available image pairs. First, the choice of the algorithm parameters is justified. Then, the experimental results obtained by using the proposed approaches are presented.

4.1.1 Preliminary Registration Results

In order to choose the parameters of the proposed method, a number of preliminary experiments have been done, using images with no changes. In particular, the first parameters of the genetic algorithm to be assigned are the number of individuals in each population and the minimum number of generations needed to achieve convergence. Then, in the selection

process, the probabilities of crossover and mutation have to be fixed. Finally, the structure and the parameters of the transformation matrix for the registration have to be established.

Choosing the size of the population can be critical since a small population size provides an insufficient sample size over the space of solutions and a large population requires a lot of evaluations, thus resulting in long computation times. Several trials were done in order to estimate the proper number. Different values for the population size were tested: As a tradeoff between accuracy and computational burden, a size of 50 individuals has been chosen in the experiment reported here.

The number of generations necessary to achieve convergence of the algorithm needs to be evaluated. In the experiments, the convergence was achieved before 150 iterations: The generation of a minimum of 180 offsprings was considered to be enough.

Evolution operators are essential to the genetic algorithm. Crossover enables the algorithm to extract the best genes from different individuals and recombine them into potentially superior offsprings. Mutation adds to the diversity of a population and thereby increases the likelihood that the algorithm will generate fitter individuals.

The number of individuals, in each generation, that undergo crossover and mutation depends on their probabilities. In order to find out proper values, both the probability of mutation, p_m, and the probability of crossover, p_c, were varied in wide ranges: p_m in [0.005, 0.25] and p_c in [0.25,1]. In conclusion p_m=0.01 was chosen here, large enough to encourage the exploration of new solutions and, at the same time, small enough not to deteriorate fit individuals. The crossover probability specifies the fraction of the population, other than "elite offsprings", that are generated by crossover. A good value can be selected within the range [0.5,1]: In this work, $p_c = 0.75$.

4.1.2 Experimental Registration Results

This section shows the results of registration of color RGB images.

In order to evaluate the performance of the proposed technique, the resultant registered image is compared to a manually registered one. In particular, a control point method was used. A good point-matching registration process requires a sufficient number of corresponding control points to be present in both images. The control points need to be uniformly distributed and not affected by lesions. An affine transformation was applied in the experiments reported here to overlay the two images. The affine transformation required the selection of at least 3 pairs of control points, which is the minimum value, but more points may be needed to obtain an accurate registration. In the implemented method, at least 6 points were chosen from both the reference and the input image of each pair to be registered.

Then, the automatic registration approach was applied. First, the image pairs to be registered were preprocessed and the vessel maps, of both input and reference image, were extracted. Some differences in the maps, due to different illuminations, determined a low value of matching.

Results of a pair of images are shown in Figure 1; such a pair presents differences in illumination and point of view. Spots also appeared from the first visit to the second one. Consequently, the vessel maps (b) and (c) exhibit large differences, but still the measure-of-match convergence is steadily achieved, as shown (a).
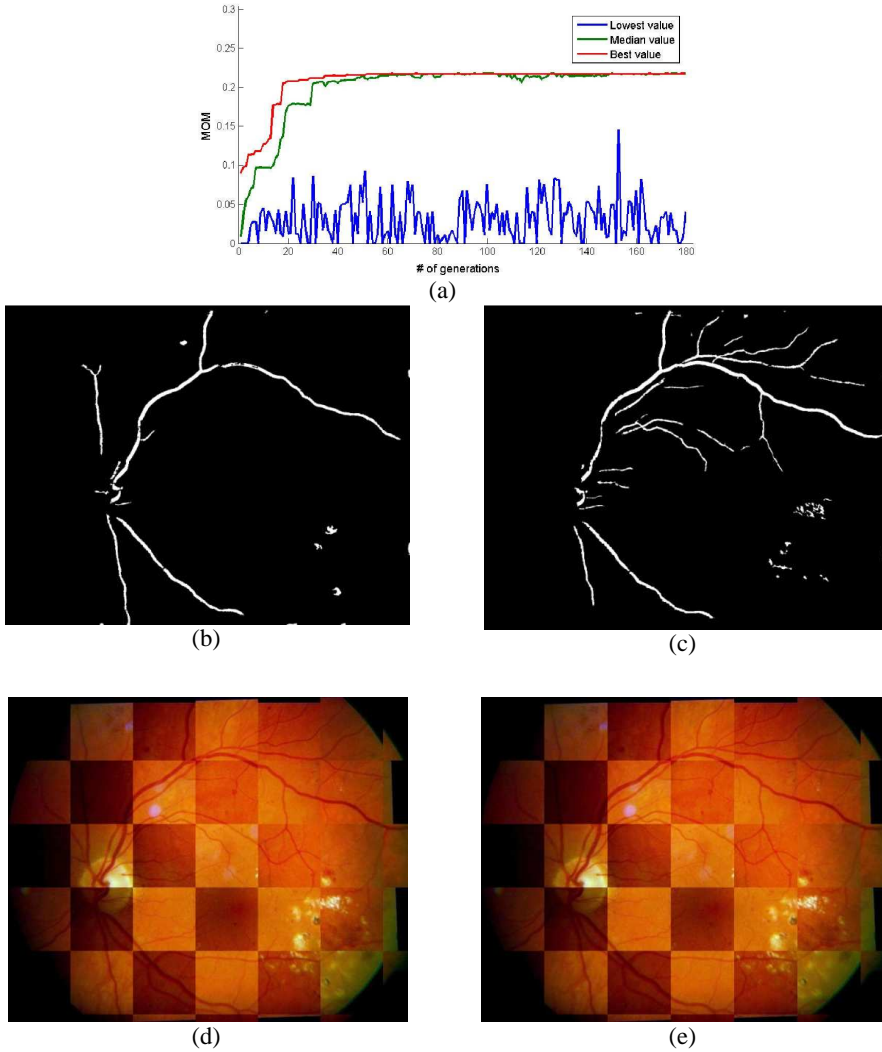
Figure 1. MOM of the individuals among the generations, for one of the data sets used in the experiments are shown in(a). The blue, the green and the red line represent respectively the lowest, the median and the highest value of MOM in the population. Vessel maps of the input image are shown in (b) and the reference image in (c). Manual and automatic registration of the image pair shown in (d) and (e), respectively, by using a checkerboard representation, in which checkers are alternately taken from the reference and the registered images.

The illumination of the two images is quite different. Therefore, the squares in the checkerboards, shown in (d) and (e), present different intensity values. However, analyzing them in detail, one may note very good vessel continuity in border regions between a square and its neighbors (i.e., where the vessel maps overlap).

Comparable results are achieved for the other image pairs.

4.2 Change-Detection Results

The proposed change-detection algorithm has been tested on the registered image pairs. First, the adopted performance measures are explained. Subsequently, the experimental results obtained by using the proposed approaches are presented and compared.

4.2.1   Performance Evaluation

The assessment of the quality of a change-detection system in the medical field is not an easy task; if a human grader does not agree with the algorithm.This can be due either to an error of the human grader or to an error of the algorithm. In order to compare the results obtained by the algorithms with the performance of a human grader, a test map (i.e., a map that displays the actual changed features found in the image pair) was created for each data set, with the support of a specialist.

In this work, we are mainly concerned with the accuracy of the methods, as opposed to execution speed. A quantitative evaluation of the results is performed, in terms of Sensitivity (Sn), Specificity (Sp), User's Accuracy for "change" (UA_{ch}) and User's Accuracy for "no-change" (UA_{nc}).

Sn, also known as "true positive rate", is the percentage of pixels which are correctly labelled as "change" in the change map over the number of actual changed pixels in the test map, as determined by a human observer (i.e., it is an estimate of the detection probability [79]). From a clinical point of view, the sensitivity of a test is an estimate of the probability that the test is positive when given to a group of patients with the disease; high Sn values mean that a negative test can rule out the disease. It can be defined as:

$$Sn = \frac{TP}{TP + FN} \qquad (12)$$

where TP is the number of true positives (i.e., "change" pixels correctly labelled as "change") and FN is the number of false negatives (i.e., "change" pixels wrongly labelled as "no-change", also called "missed alarms").

The specificity, also known as "true negative rate", is the percentage of the pixels that are correctly labeled as "no-change". Therefore, the specificity is an estimate of $(1 - P_F)$, where P_F is the false-alarm probability [79]). The specificity of a medical test is an estimate of the probability that the test will be negative among patients who do not have the disease; therefore, a high Sp value means that a positive test can rule in the disease. It can be defined as:

$$Sp = \frac{TN}{TN + FP} \qquad (13)$$

where TN and FP are the number of true negatives (i.e., "no-change" pixels correctly labelled as "no-change") and false positives (i.e., "no-change" pixels wrongly labelled as "change", also called "false alarms"), respectively.

In this work we favour Sn to Sp. In fact, in order to avoid missed alarms, which play a relevant role from a clinical perspective, we aim at minimizing false negatives. However, it is worth noticing that also false positives need to be minimized, in order to reduce the number of false alarms.

UA_{ch} is the percentage of pixels which are correctly assigned to "change" (*TP*) over the total number of pixels labelled as "change" in the change map. It can be defined as:

$$UA_{ch} = \frac{TP}{TP + FP}$$ (14)

A similar definition holds for UA_{nc}, which is the percentage of pixels which are correctly assigned to "no-change" (*TN*) over the total number of pixels labelled as "no-change" in the change map. It can be defined as:

$$UA_{nc} = \frac{TN}{TN + FN}$$ (15)

4.2.2 Experimental Change-Detection Results

The results obtained for the available data sets endowed with test data are shown in Table 1. The performances of the approach are satisfactory, in terms of both *Sn* and *Sp*.

Table 1: Average performance parameters obtained by applying the KEI approach to all the data sets.

Sn	Sp	UA_{ch}	UA_{nc}
71,20%	99,86%	84,30%	99,80%

Sp is generally very high in part because the number of true negatives (i.e., those pixels that are correctly classified as "no-change") is always high. On the other hand, *Sn* is more variable because it strictly depends on the quality and similarities in luminance of the input images and is thus affected by sharp differences in the image dynamics at the two dates. The average sensitivity is about 71%, which is an acceptable value. The error is due to the unsuccessful detection of some pixels belonging to correctly detected change areas. This is not critical because, here, we aim at detecting the change areas: Their exact shape could be a posteriori reconstructed.

With regard to the user's accuracies, very good values of UA_{nc} were obtained for all data sets, and quite good values of UA_{ch} (average above 84%) were given by the method.

For coherence with Section 4.1.2, the same data set is employed to show the change-detection results (Figure 2). In particular, the input image (a) and the reference image (b) are acquired during two different medical visits, 8 months apart. A lot of typologies of change are present in this data set, including new and old spots of both "red" and "white" types.

(a)   (b)

©   (d)
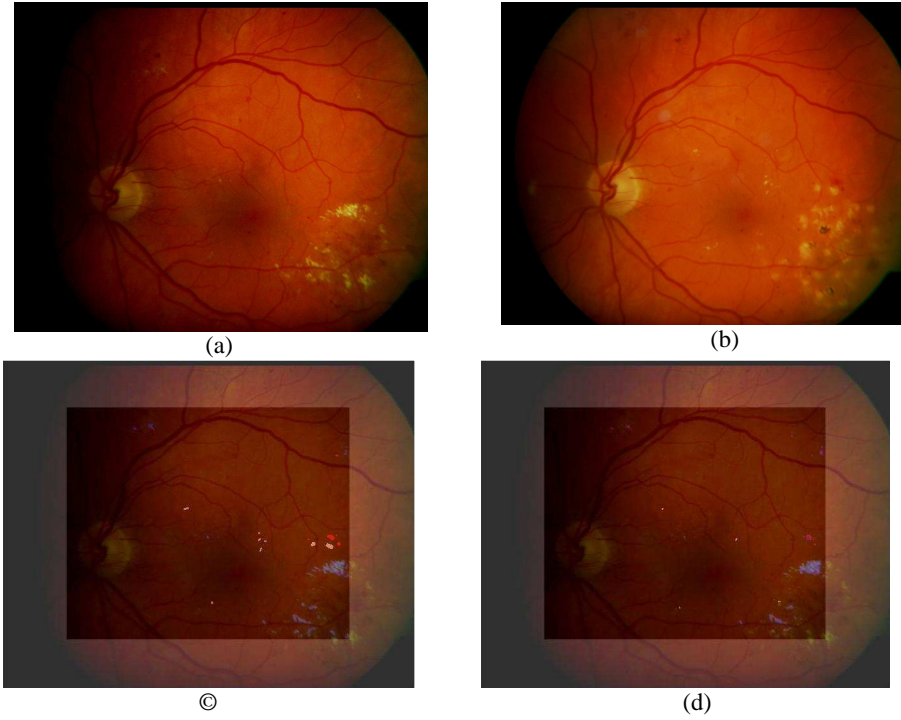
Figure 2: Test map (a) and resulting classification map (b) generated by the proposed approach, when applied to the data set (a) and (b).

In this case, high specificity is obtained (i.e., 99.9%), thanks to the high number of true "no-change" pixels. However, the sensitivity is 62.4%, because the presence and the positions of most "change" areas are correctly detected, but their shape is not perfectly reconstructed. Anyway, the detection of the changes and their classification among the different typologies, which represent clinically relevant information, are achieved.

5 Conclusions

The purpose of this chapter was the development of a technique able to automatically register and detect the temporal changes in retinal images. The registration is achieved by using a method based on a genetic optimization technique; the proposed change-detection approach is based on the Kittler & Illingworth's thresholding algorithm. RGB retina images, captured by a fundus camera, were used.

First, the images were preprocessed, in order to obtain their vessel maps from which a matching measure (adopted as the optimization functional) was extracted. Once the optimum transformation was obtained, it was used to register the input image with respect to the reference one. The reference and the registered images were used as input for the change-detection process.

Different types of images, including changes of different sizes and typologies, were taken into account in order to test the performances of the method. The proposed approach

provided quite accurate results. The accuracy of the registration step, as compared to manual registration, has been evaluated by visual inspection of the results, on a collection of pairs of images of variable qualities. Very good overlapping between the reference and the input images was obtained. The change-detection results obtained by applying the proposed approach were accurate. The K&I technique, which was developed in the context of computer vision and previously applied to change-detection problems on other typologies of images [50], [51], has proven to be effective also when applied to fundus images here.

The main drawback is the possible sensitivity to the presence of undesired modes, such as artifacts and glares, which may occur also as a consequence of a partially inaccurate preprocessing stage. The development and the implementation of a method for the automatic identification of ungradable images may be an important next step of this research. A possible future development of the proposed approach could be the integration of contextual information in the change-detection process: Spatial information may be exploited in the postdetection classification stage, in order to further improve the accuracy of the classification map.

References

1. J. W. Berger and D. S. Shin: Computer vision enabled augmented reality fundus biomicroscopy. *Ophthalmology*, vol. 106, 1999.
2. M. J. Cree, J. A. Olson, K. C. McHardy, P. F. Sharp, and J. V. Forrester: A fully automated comparative microaneurysm digital detection system. *Eye*, vol. 11, pp. 622--628, 1997.
3. D. Usher, M. Dumskyj, M. Himaga, T. H. Williamson, S. Nussey, and J. Boyce: Automated detection of diabetic retinopathy in digital retinal images: a tool for diabetic retinopathy screening. *Diabetic Medicine*, vol. 21, pp. 84--90, 2003.
4. T. Walter, J. C. Klein, P. Massin, and A. Erginary: A contribution of image processing to the diagnosis of diabetic retinopathy – detection of exudates in color fundus images of the human retina. *IEEE Transactions on Medical Imaging*, vol. 21, no. 10, pp. 1236--1243, 2002.
5. F. Laliberté, L. Gagnon, and Y. Sheng: Registration and fusion of retinal images – an evaluation study. *IEEE Transactions on Medical Imaging*, vol. 22, pp. 661--673, 2003.
6. J. Kittler and J. Illingworth: Minimum error thresholding. *Pattern Recognition*, vol. 19, no. 1, pp. 41--47, 1986.
7. V. R. Algazi, J. L. Keltner, C. A. Jonhson: Computer Analysis of the optic Cup in Glaucoma. Investigative Ophthalmology and Visual Science, vol. 26, pp. 1759--1770, 1985.
8. E. Peli and M. Lahav: Drusement Measurement from Fundus Photographs using Computer Image Analysis. *Opthalmology*, vol. 93, pp. 1575--1580, 1986.
9. RP Phillips, T Spencer, PG Ross, PF Sharp, and JV Forrester: Quantification of diabetic maculopathy by digital imaging of the fundus. *Eye,* vol. 5, pp. 130--137, 1991.
10. L. Brown: A survey of images registration techniques. *ACM Computing Surveys*, vol. 24, no. 4, pp. 326-376, 1992.
11. B. Zitova and J. Flusser: Image registration methods: a survey. *Image and Vision Computing*, vol. 21, pp. 977--1000, 2003.
12. A.V. Cideciyan: Registration of ocular fundus images. *IEEE Engineering in Medicine and Biology*, vol. 14, pp. 52--58, 1995.
13. A. Can, H. Shen, J. N. Turner, H. L. Tanenbaum, and B. Roysam: Rapid automated tracing and feature extraction from live high-resolution retinal fundus images using direct exploratory algorithms. *IEEE Transactions on Information Technology in Biomedicine*, vol. 3, no. 2, pp. 125--138, 1999.
14. A. Hoover, V. Kouznetsova, and M. Goldbaum: Locating blood vessels in retinal images by piecewise

threshold probing of a matched filter response. *IEEE Transactions on Medical Imaging*, vol. 19, no. 3, pp. 203--210, 2000.

15. J. Staal, M. Abramoff, M. Niemeijer, M. Viergever, and B. van Ginneken: Ridge based vessel segmentation in color images of the retina. *IEEE Transactions on Medical Imaging*, vol. 23, no. 4, pp. 501—509, 2004.

16. A. Hoover and M. Goldbaum: Locating the optic nerve in a retinal image using the fuzzy convergence of the blood vessels. *IEEE Transactions on Medical Imaging*, vol. 22, no. 8, pp. 951—958, 2003.

17. J. Lowell, A. Hunter, D. Steel, A. Basu, R. Ryder, and E. Fletcher. Optic nerve head segmentation. *IEEE Transactions on Medical Imaging*, vol. 23, no. 2, pp. 256--264, 2004.

18. M. Foracchia, E. Grisan, and A. Ruggeri: Detection of optic disc in retinal images by means of a geometrical model of vessel structure. *IEEE Transactions on Medical Imaging*, vol. 23, no. 10, pp. 1189--1195, 2004.

19. A. Pinz, S. Bernogger, P. Datlinger, and A. Kruger: Mapping the human retina: *IEEE Transactions on Medical Imaging*, vol. 17, no. 4, pp. 606--620, 1998.

20. E. Peli, R. A. Augliere, and G. T. Timberlake: Feature-based registration of retinal images. *IEEE Transactions on Medical Imaging*, vol. 6, no. 3, pp. 272--278, 1987.

21. M. H. Goldbaum, V. Kouznyetsova, B. Cote, M. Nelson, and W. E. Hart: Automated registration of digital ocular fundus images for comparison of lesions. *Proceedings of Ophthalmic Technologies III, SPIE*, vol. 1877, no. 1, pp. 94--99, 1993.

22. F. Zana and J. Klein: A multimodal registration algorithm of eye fundus images using vessels detection and hough transform. IEEE Transactions on Medical Imaging, vol. 18, no. 5, pp. 419--428, 1999.

23. J. Domingo, G. Ayala, A. Simo, and E. de Ves: Irregular motion recovery in fluorescin angiograms. *Pattern Recognition Letters*, vol. 18, pp. 805--821, 1997.

24. A. Can, C. V. Stewart, B. Roysam, and H. L. Tanenbaum: A feature-based, robust, hierarchical algorithm for registering pairs of images of the curved human retina. *IEEE Transactions on Information Technology in Biomedicine*, vol. 3, no. 2, pp. 125--138, 2002.

25. C. V. Stewart, C.-L. Tsai, and B. Roysam: The Dual-Bootstrap Iterative Closest Point Algorithm With Application to Retinal Image Registration. *IEEE Transactions on Medical Imaging*, vol. 22, no. 11, pp. 1379--1394, 2003.

26. C.D. Kuglin and D.C. Hines: The phase correlation image alignment method. *In Proceeding of the International Conference on Cybernetics and Society*, 163--165, 1975.

27. E. De Castro, G. Cristini, A. Martelli, C. Morandi, and M. Vascotto: Compensation of Random Eye Motion in Television Ophthalmoscopy: Preliminary Results. *IEEE Transactions on Medical Imaging*, vol. 6, pp. 74--81, 1987.

28. E. De Castro and C. Morandi: Registration of Translated and Rotated Images Using Finite Fourier Transforms. *IEEE Transactions on Pattern Analysis and Machine Intelligence*, vol. 9, pp. 700--703, 1987.

29. N. Ritter, R. Owens, J. Cooper, R. H. Eikelboom, and P. P. V. Saarloos: Registration of stereo and temporal images of the retina. *IEEE Transactions on Medical Imaging*, vol.18, no. 5, pp. 404--418, 1999.

30. T. Butz and J.-P. Thiran: Affine registration with feature space mutual information. In *Medical Image Computing and Computer-Assisted Intervention*, W. J. Niessen and M. A. Viergever, Eds. 2001, vol. 2208 of *Lecture Notes in Computer Science*, pp. 549--556, Springer-Verlag, Berlin.

31. G. K. Matsopoulos, N. A. Mouravliansky, K. K. Delibasis, and K. S. Nikita: Automatic retinal image registration scheme using global optimisation techniques. *IEEE Transactions On Information Technology in Biomedicine*, vol. 3, no. 1. pp. 47--60, 1999.

32. P. Deer and P. Eklund: Values for the fuzzy C-means classifier in change detection for remote sensing. In *Proceedings of the 9th International Conference On Information Processing and Management of Uncertainty, IPMU 2002*, pp. 187--194, 2002.

33. C. Oliver and S. Quegan: *Understanding Synthetic Aperture Radar Images*. Norwood, MA: Artech House, 1998.

34. E. J. M. Rignot and J. J. Van Zyl: Change detection techniques for ERS-1 SAR data. *IEEE Transactions on Geoscience and Remote Sensing*, vol. 31, no. 4, pp. 896--906, 1993.

35. R. G. White: Change detection in SAR imagery. *International Journal on Remote Sensing*, vol. 12, no. 2, pp. 339--360, 1990.

36. X. Li and A. G. Yeh: Multitemporal SAR images for monitoring cultivation systems using case-based reasoning. *Remote Sensing of Environment*, vol. 90, no. 4, pp. 524--534, 2004.

37. L. Bruzzone, D. F. Prieto, and S. B. Serpico: A neural-statistical approach to multitemporal and multisource remote-sensing image classification. *IEEE Transactions on Geoscience and Remote Sensing*, vol. 37, no. 3, pp. 1350--1359, 1999.

38. F. Melgani: Classification of multitemporal remote-sensing images by a fuzzy fusion of spectral and

spatio-temporal contextual information. *International Journal of Pattern Recognition and Artificial Intelligence*, vol. 18, no. 2, pp. 143--156, 2002.

39. F. Melgani and S. B. Serpico: A statistical approach to the fusion of the spectral and spatio-temporal contextual information for the classification of remote sensing images. *Pattern Recognition Letters*, vol. 23, no. 9, pp. 1053--1061, 2002.

40. K. Conradsen, A. Aasbjerg Nielsen, J. Schou, and H. Skriver: A test statistic in the complex Wishart distribution and its application to change detection in polarimetric SAR data. *IEEE Transactions on Geoscience and Remote Sensing*, vol. 41, no. 1, pp. 4--19, 2003.

41. P. Lombardo and T. Macrí Pellizzeri: Maximum likelihood signal processing techniques to detect a step pattern of change in multitemporal SAR images. *IEEE Transactions on Geoscience and Remote Sensing*, vol. 40, no. 4, pp. 853--870, 2002.

42. A. Singh: Digital change detection techniques using remotely-sensed data. *International Journal of Remote Sensing*, vol. 10, no. 6, pp. 989--1003, 1989.

43. S. C. Liew, S.-P. Kam, T.-P. Tuong, P. Chen, V. Q. Minh, and H. Lim: Application of multitemporal ERS-1 synthetic aperture radar in delineating rice cropping systems in the Mekong River Delta, Vietnam. *IEEE Transactions on Geoscience and Remote Sensing*, vol. 36, no. 5, pp. 1412--1420, 1998.

44. W. Dierking and H. Skriver: Change detection for thematic mapping by means of airborne multitemporal polarimetric SAR imagery. *IEEE Transactions on Geoscience and Remote Sensing*, vol. 40, no. 3, pp. 618--636, 2002.

45. P. Rosin: Thresholding for change detection. *Computer Vision and Image Understanding*, vol. 86, no. 2, pp. 79--95, 2002.

46. P. Rosin and E. Ioannidis: Evaluation of global image thresholding for change detection," *Pattern Recognition Letters*, vol. 24, no. 14, pp. 2345--2356, 2003.

47. P. Smits and A. Annoni: Toward specification-driven change detection. *IEEE Transactions on Geoscience and Remote Sensing*, vol. 38, no. 3, pp. 1484--1488, May 2000.

48. H. V. Poor: An Introduction to Signal Detection and Estimation, 2nd ed. Springer-Verlag, 1994.

49. S. M. Kay: Fundamentals of Statistical Signal Processing: Detection Theory. Prentice-Hall, 1993.

50. G. Moser and S. B. Serpico: Generalized minimum-error thresholding for unsupervised change detection from SAR amplitude imagery. *IEEE Transactions on Geoscience and Remote Sensing*, vol. 44, no. 10, pp. 2972--2982, 2006.

51. F. Melgani, G. Moser, and S. B. Serpico: Unsupervised change detection methods for remote sensing images. *Optical Engineering*, vol. 41, no. 12, pp. 3288--3297, 2002.

52. G. Moser, F. Melgani, and S. B. Serpico: Advances in unsupervised change detection. In *Frontiers of Remote Sensing Information Processing*, C. H. Chen, Ed. Singapore: World Scientific, 2003.

53. L. Bruzzone and D. F. Prieto: Automatic analysis of the difference image for unsupervised change detection. *IEEE Transactions on Geoscience and Remote Sensing*, vol. 38, no. 3, pp. 1171--1182, 2000.

54. L. Bruzzone and D. F. Prieto: An adaptive semiparametric and context-based approach to unsupervised change detection in multitemporal remote-sensing images. *IEEE Transactions on Image Processing*, vol. 11, no. 4, pp. 452--466, 2002.

55. J. E. Colwell and F. P. Weber: Forest change detection. In *Proceeding of the 15th International Symposium on Remote Sensing of Environment*, pp. 839--852, 1981.

56. W. A. Malila: Change vector analysis: an approach for detecting forest changes with Landsat. In *Proceeding of the 6th Annual Symposium on Machine Processing of Remotely Sensed Data*, pp. 326--335, 1980.

57. L. Di Stefano, S. Mattoccia, and M. Mola: A change-detection algorithm based on structure and colour. In *IEEE Conference on Advanced Video and Signal-Based Surveillance 2003*, pp. 252--259, 2003.

58. S. Sakuma, T. Nakanishi, Y. Takahashi, Y. Fujino, S. Ohtsuka, A. Tomono, N. Nakanishi, T. Tsubouchi, and T. Tanino: Image registration, color correction, and change detection based on value of difference in sequential ocular fundus images. *Systems and Computers in Japan*, vol. 37, no. 11, pp. 100--112, 2006.

59. J. W. Berger, T. R. Patel, D. S. Shin, J. R. Piltz, and R. A. Stone. Computerized stereo chronoscopy and alternation flicker to detect optic nerve head contour change. *Ophthalmology*, vol. 107, no. 7, pp. 1316--1320, 2000.

60. M. J. Cree, J. A. Olson, K. C. McHardy, P. F. Sharp, and J. V. Forrester: A fully automated comparative microaneurysm digital detection system. *Eye*, vol. 11, pp. 622--628, 1997.

61. M. J. Cree, J. A. Olson, K. C. McHardy, P. F. Sharp, and J. V. Forrester: The preprocessing of retinal images for the detection of Fluorescein leakage. *Physics in Medicine and Biology*, vol. 44, pp. 293--308, 1999.

62. K. A. Goatman, M. J. Cree, J. A. Olson, J. V. Forrester, and P. F. Sharp: Automated measurement of m microaneurysm turnover. *Investigative Ophthalmology and Visual Science*, vol. 44, pp. 5335--5341, 2003.

63. Z. B. Sbeh, L. D. Cohen, G. Mimoun, and G. Coscas: A new approach of geodesic reconstruction for

drusen segmentation in eye fundus images. *IEEE Transactions on Medical Imaging*, vol. 20, no. 12, pp. 1321--1333, 2001.

64. H. Narasimha-Iyer*,* A. Can*,* B. Roysam, C. V. Stewart, H. L. Tanenbaum, A. Majerovics, and H. Singh: Robust Detection and Classification of Longitudinal Changes in Color Retinal Fundus Images for Monitoring Diabetic Retinopathy. *IEEE Transactions on Biomedical Engineering*, vol. 53, no. 6, 2006.

65. H. Narasimha-Iyer, A. Can, B. Roysam, H.L. Tanenbaum, and A. Majerovics: Integrated Analysis of Vascular and Non-Vascular Changes from Color Retinal Fundus Image Sequences. *IEEE Transactions on Biomedical Engineering*, vol. 54, no. 8, pp. 1436--1445, 2007.

66. F. Laliberté, L. Gagnon, and Y. Sheng: Registration and Fusion of Retina Images - An evaluation study. *IEEE Transactions on Medical Imaging*, vol. 22, no. 5, pp. 661--673, 2003.

67. A. Can, C. V. Stewart, B. Roysam, and H. L. Tanenbaum: A feature-based, robust, hierarchical algorithm for registering pairs of images of the curved human retina. *IEEE Transactions on Information Technology in Biomedicine*, vol. 3, no. 2, pp. 125--138, 2002.

68. K. E. Rayner: Eye Movements and Visual Cognition: Scene Perception and Reading. Springer Verlag, New York, second edition, 1992.

69. J. Serra: Image Analysis and mathematical Morphology. Academic Press, London, 1982.

70. J. Chanussot, G. Mauris, and P.Lambert: Fuzzy fusion techniques for linear features detection in multitemporal SAR images. *IEEE Transactions on Geoscience and Remote Sensing*, vol. 37, no. 3, 1999.

71. G. Troglio, J. A. Benediktsson, S. B. Serpico, G. Moser, R. A. Karlsson, G. H. Halldorsson, and E. Stefansson: Automatic registration of retina images based on genetic techniques. *In Proceeding of the IEEE Engineering for Medicine and Biology Conference*, pp. 5419--5424, 2008.

72. Z. Michalewicz: Genetic Algorithms + Data Structures = Evolution Programs.
Springer Verlag, Berlin Heidelberg, third edition, 1999.

73. L. Bruzzone and R. Cossu: Analysis of multitemporal remote-sensing images for change detection: Bayesian thresholding approaches. In C.H.Chen, Ed., Geospatial Pattern Recognition, pp. 203–230, editor: E. Binaghi, P.A. Brivio and S.B. Serpico, Alphen aan den Rijn, Netherlands, 2002.

74. K. Akita and H. Kuga: A computer method of understanding ocular fundus images. *Pattern Recognition*, vol. 15, no. 6, pp. 431--443, 1982.

75. C. Sinthanayothin, J. F. Boyce, H. L. Cook, and T. H. Williamson: Automated localisation of the optic disc, fovea, and retinal blood vessels from digital color fundus images. *British Journal of Ophthalmology*, vol. 83, no. 8, pp. 902--910, 1999.

76. Z. Chi, H. Yan, and T. Pham. Fuzzy algorithms: with applications to image processing and pattern recognition. World Scientific Publishing, Singapore, 1996.

77. L.-K. Huang and M.-J. J. Wang: Image thresholding by minimizing the measures of fuzziness. *Pattern Recognition*, vol. 28, no. 1, pp. 41--51, 1995.

78. N. Otsu: A threshold selection method from gray-level histograms. *IEEE Transactions on Systems, Man and Cybernetics*, vol. 9, no. 1, pp. 62--66, 1979.

79. R.O. Duda, P.E. Hart, and D.G. Stork: Pattern Classiffcation. Wiley, New York, 2001.

Biography

Giulia Troglio received (*summa cum laude*) the B. S. degree in biomedical engineering and the M. S. degree in bioengineering at the University of Genoa in 2004 and 2007, respectively. At present, she is Ph.D. student in computer and electrical engineering both at the Faculty of Electrical and Computer Engineering of the University of Iceland and at the Department of Biophysical and Electronic Engineering of the University of Genoa. From May to August 2008, she was a Visiting Student with the Goddard Space Flight Center, NASA, USA. Her research activity mainly includes analysis of retinal images, image registration, change detection, remote sensing, segmentation of planetary images. She has been reviewer for different international journals.

Jón Atli Benediktsson received the Cand.Sci. degree in electrical engineering from the University of Iceland, in 1984 and the M.S.E.E. and Ph.D. degrees from Purdue University, West Lafayette, IN, in 1987 and 1990, respectively. He is currently the Vice President for Academic Affairs and Professor of Electrical and Computer Engineering at the University of Iceland. His research interests are in remote sensing, biomedical signal analysis, pattern recognition, data fusion and image analysis. He has published extensively in those fields. Dr. Benediktsson was Editor-in-Chief of the IEEE Transactions on Geoscience and Remote Sensing (TGRS) (2003 -2008) and is currently Associate Editor of TGRS and IEEE GRSL.. He is the IEEE Geoscience and Remote Sensing Society Executive Vice President for 2010–2011. He is a Fellow of the IEEE.

Gabriele Moser received (*summa cum laude*) the M.Sc. degree in telecommunications engineering and the Ph.D. degree in space sciences and engineering from the University of Genoa, Italy, in 2001 and 2005, respectively. Since 2001, he has been a research fellow with the Signal Processing and Telecommunications Research Group of the Department of Biophysical and Electronic Engineering, University of Genoa, in the field of remote-sensing image analysis. From January to March 2004, he was a visiting student at INRIA, Sophia Antipolis, France. His research activity is focused on image-processing and pattern-recognition methodologies for remote-sensing and biomedical data interpretation. He has been a reviewer for several international journals. Since 2008, he has been an Associate Editor of the IEEE Geoscience and Remote Sensing Letters.

Sebastiano B. Serpico received the M. S. degree in electronic engineering and the Ph.D. in telecommunications from the University of Genoa, in 1982 and 1989, respectively. Currently, he is a Full Professor of telecommunications at the University of Genoa where he is the Head of the Signal Processing and Telecommunications laboratory. His current research interests include the application of pattern recognition and image analysis (feature selection, classification, change detection, and data fusion) to remote sensing and biomedical data. He is author or co-author of more than 200 scientific articles. He is the Chairman of the Institute of Advanced Studies in ICT (ISICT). Since 2001, he has been an Associate Editor of IEEE Transactions on Geoscience and Remote Sensing. He is a Fellow of the IEEE.

Einar Stefánsson graduated from the University of Iceland Medical School in 1978 and received the Ph.D. degree in ocular physiology from Duke University in 1981. He is Professor and Chair of the Department of Ophthalmology, at the University of Iceland from 1989. He has served as Vice Dean and Dean of the Faculty of Medicine at the University of Iceland. He is a vitreoretinal surgeon; his main clinical interest is diabetic eye disease. He has published more than 130 peer-reviewed international publications, several hundred abstracts, book chapters and patents. He is Editor-in- Chief of Acta Ophthalmologica Scandinavica, on the editorial boards of the European Journal of Ophthalmology and PRER, board member of EURETINA, NOK and the Michaelson Club. In addition he is a Fellow of the American Academy of Ophthalmology.

Appendix B

Paper 2

G. Troglio, J. A. Benediktsson, G. Moser, S. B. Serpico, and E. Stefansson. "Unsupervised Multiple Classifiers for Retinal Change Detection," *Pattern Recognition Letters*, submitted.

Unsupervised Multiple Classifiers for Retinal Change Detection

Giulia Troglio[a,b,1], Jon A. Benediktsson[a], Gabriele Moser[b], Sebastiano B. Serpico[b],
Einar Stefansson[a]

[a]*Electrical and Computer Engineering Faculty and Ophthalmology Department, University of Iceland,
Reykjavik, Iceland*
[b]*Biophysical and Electronic Engineering Department, University of Genoa, Genova, Italy*

Abstract

Retinal change detection is a powerful tool that can be used as a support for the monitoring of retinopathy in diabetic eye screening. Here, an automatic method is proposed for change detection in multitemporal retinal images, i.e., images acquired by a fundus camera from patients with diabetic retinopathy during different medical visits. The proposed approach is based on the registration of the collected images and on the detection of the changes that can occur in the retina during time. A genetic algorithm is used for the registration. For the change detection, a multiclassifier approach, based on a minimum-error thresholding technique, is proposed. To cope with local illumination differences, unsupervised thresholding is applied to randomly selected subimages and the outputs of the different windows are combined with a majority vote approach. Quantitative assessment of the change detection results shows that the proposed method provides accurate results. The comparison between the results obtained using the implemented multiclassifier approach and a standard approach points out that the proposed algorithm provides a more accurate change detection and a reduced sensitivity to the illumination issues.

Keywords: Multiple Classifiers, Change Detection, Retinal Images

[1]Tel.: +390103532672; fax: +390103532134; email: git2@hi.is

1. Introduction

In ophthalmology, the diagnosis of retinal diseases is often based on the analysis of fundus images, including retinal changes that can occur over time. Therefore, the examination of multitemporal images is an important diagnostic tool. Fundus images may be used to follow the progression of retinal diseases (Fritzsche et al., 2003), revealing retinal changes that have occurred during the period between medical visits. During the last years an intensified effort has been undertaken in developing tools to assist in the screening of diabetic retinopathy, which is the most common cause of legal blindness in the working age population of developed countries (Arun et al., 2009; Bek et al., 2009). Furthermore, effective treatments are available if the disease is detected early, before visual symptoms occur (Stefansson et al., 2009; Walter et al., 2002).

In screening programs, ophthalmologists have to deal with a large number of images. Therefore, automatic image analysis methods have been acquiring a growing interest. In particular, change detection in pathologies such as microaneurysms and retinal microhemorrhages would be useful in diabetic eye screening programs and possibly reduce the manpower needed for image evaluation.

Typically, the detection of retinal diseases has been addressed using supervised methods (Usher et al., 2003), which require training based on information from an expert on the data. In Usher et al. (2003) morphological operators and neural networks were used to detect and classify retinal lesions. The results strictly depended on the resolution and contrast of the photographs. A large number of studies have reported interesting preliminary results for retinopathy detection. Automatic techniques for detecting and counting microaneurysm in fluorescein angiograms have given good results (Cree et al., 1997; Spencer et al., 1992, 1996). However, angiography with intravenous fluorescein is too invasive to be used during

screening and the role of oral fluorescein is uncertain (Newsom et al., 2000).

Although many studies have been done to detect specific retinal diseases, few efforts have been undertaken to analyze their time evolution. A rare example can be found in Narasimha-Iyer et al. (2006), where changes were detected using a Bayesian approach. However, a training set, in which "change" and "nochange" classes are manually labeled, was required.

In this paper, an automatic technique is proposed for the detection of changes (in terms of red and white spots) in fundus images and for their registration (Brown, 1992). The implemented registration method is based on an optimization technique (Matsopoulos et al., 1999). The proposed change detection approach is based on the automatic thresholding method (K&I) proposed by Kittler and Illingworth (1986), applied to an appropriate difference image. However, the application of K&I to the whole image may be severely affected by the spatial behavior of the illumination field at the two observation dates. To compensate for nonuniform illumination across each acquisition and also for the variation of illumination between the two acquisitions, a multiclassifier voting approach (Troglio et al., 2010) is proposed. K&I is applied to randomly generated subimages, corresponding to different classifiers. This approach is based on the hypothesis that the illumination is approximately uniform in each subimage. By combining the multiple classifiers we aim at a more accurate classification although that comes at the expense of increased complexity and computational cost (Kuncheva, 2004).

The main novelty of this paper lies in the development of a fully automatic and unsupervised method, able to register retinal images, compare them, and detect changes occurred in between different medical visits. Moreover, the introduction of a multiple classifier system for change detection is novel and the idea of combining the vote of spatially different classifiers to overcome local illumination differences is new in the contest of multiclassifier

141

approaches.

The paper is organized as follows. Section 2 describes the methodology of the proposed approach. In Section 3, results are shown, and in Section 4 conclusions are drawn.

2. Methodology

2.1. Overview of the Proposed Approach

A pair of images, acquired from a given patient during different medical visits, is registered using an optimization technique (see Section 2.2). Once the images are aligned, they are compared by image differencing and the changes between them are detected using K&I (Kittler and Illingworth, 1986) and a multiclassifier approach (see Section 2.3). Figure 1 shows the overall architecture of the proposed approach.
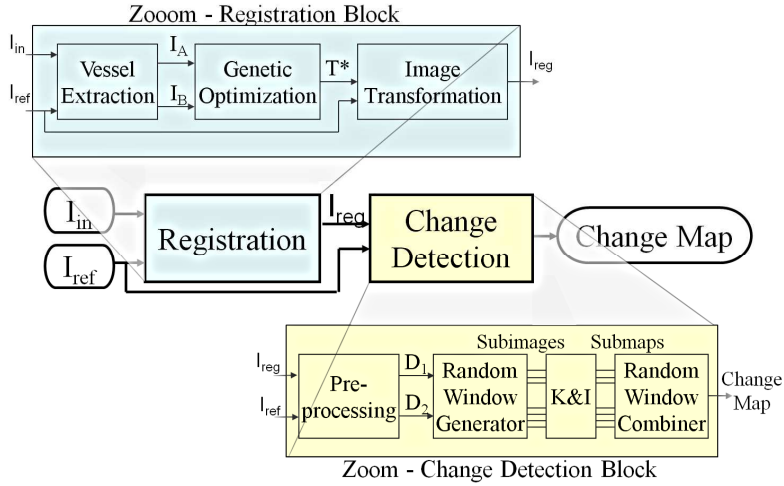
Figure 1: Architecture of the proposed approach.

Retinal image registration is a hard task because the eye position and rotation may vary between images, the illumination is rather uneven due to light scattering within the eye, and artifacts are often present.

Several automatic approaches for retinal image registration have been proposed in the literature. Those techniques can be divided into area-based and feature-based. Area-based approaches are generally based on pixel intensities and on optimization techniques. Those methods, often used in multitemporal and multimodal registration, adopt criteria such as least mean square error, crosscorrelation, phase correlation, and mutual information (Ritter et al., 1999; Ballerini, 1997). Feature-based approaches assume that point correspondences are available in both images to be registered and the registration is performed by matching those correspondences (Can et al., 2002; Lalibert et al., 2003).The performance of those methods largely depends on sufficient and reliable point correspondences.

Here, we propose an automatic approach based on the robust extraction of retinal vessels and a global optimization technique to match the extracted features (see Fig. 1). Vessels are used being the most prominent retinal feature, they cover all the fundus, and are assumed to be stable over time. Vessel elongation, changes in width and tortuosity may happen, due to specific retinal diseases, but here we assume that they are not great enough between visits to markedly affect the main vascular structure Kristinsson et al. (1997).

The input and reference images, I_{in} and I_{ref}, are first preprocessed to obtain the correspondent vessel maps I_A and I_B. An approach based on mathematical morphology, proposed in Chanussot et al. (May 1999) for road detection in remote-sensing images, is used here to extract retinal vessels. The method is unsupervised and involves very few parameters (i.e., the dimensions of the morphological operator structuring elements and one double

threshold).

I_A and I_B are fed as inputs to a module aimed at optimizing the transformation matrix T. The problem is formulated as determining a transformation T^* such that, when T^* is applied to I_A the best match with I_B is achieved. Mathematically, it can be formulated as the maximization of

$$MOM(T) = \frac{1}{n} \sum_{(x,y):I_B(x,y)\neq 0} I_A(T(x,y)), \tag{1}$$

where MOM (Measure Of Match) denotes the objective function, T is the transformation of the x and y coordinates in the image plane, and n is the number of nonzero pixels of I_B. An affine transformation model, which exhibits 6 independent parameters, is employed for T.

Equation 1 is considered appropriate in this case, where I_A and I_B are not identical and may contain noisy pixels. Correlation methods based on distance measure calculations would not perform satisfactory; they would be affected by noise and local differences between the images. Furthermore, elastic methods (van den Elsen et al., 1993) would increase the computational cost.

For the determination of the transformation parameters, search based methods provide a solution, based on the optimization of a matching functional between the images. For retinal image registration, where MOM has multiple extremes, global optimization techniques are the most attractive search methods. Here, a Genetic Algorithm (GA) (Michalewicz, 1999) is adopted (as proposed in Troglio et al. (2008)), since it ensures, under mild assumptions, convergence to a global maximum. GA was proven to be more efficient compared to other global optimization techniques in this case (Mouravliansky et al., 1998). GA is used to find a transformation T^* that maximizes MOM. The transformation parameters are converted

into binary digits concatenated in a single string, called individual. First, the initial population of individuals is randomly defined. The population is evaluated calculating the fitness of each individual (i.e., MOM of the transformation parameters encoded in the individual). Pairs of fit individuals are selected to recombine their encoded parameters in order to produce offsprings. In an iterative process, a new generation of solutions, which replaces the previous one, is produced at each step, until the MOM convergence is achieved. The final transformation matrix T^* is calculated decoding the last population fittest individual. T^* is applied to I_{in}, in order to obtain the registered image, I_{reg}.

2.3. Change Detection

After a preprocessing step (see Section 2.3.1), the proposed multiclassifier change detection approach (see Section 2.3.2), based on unsupervised thresholding (see Section 2.3.3), is applied.

2.3.1. Feature Transformation

First, the nonuniform illumination is corrected in both images using a homomorphic filtering technique (Oppenheim et al., 1968). For Lambertian surfaces, an observed image I_O can be modeled as a multiplicative composition of a luminance component, L_O, and a reflectance component, R_O (Toth et al., 2000),

$$I_O = L_O \cdot R_O. \tag{2}$$

This model holds for fundus images due to the diffusive retinal characteristics. L_O can be assumed to vary slowly over space, whereas R_O contains also medium and high frequency details (Brinkmann et al., 1998). Applying the logarithm, the multiplicative relation in

equation 2 is transformed into an additive one:

$$\log(I_O) = \log(L_O) + \log(R_O). \tag{3}$$

Gaussian filtering G is applied to $\log(I_O)$, isolating the lowpass component, $G(\log(I_O)) = \log(L_O)$. Hence R_O can be estimated as

$$R_O = \exp\{\log(I_O) - G(\log(I_O))\}. \tag{4}$$

The reflectance components R_{ref} and R_{reg} are estimated for I_{ref} and I_{reg}. Subsequently, before performing image differencing, R_{ref} and R_{reg} (i.e., two 3-cannel RGB images) need to be projected into a 1-channel feature space. The 3 RGB channels contain different information: The red channel, I_ρ, is usually the brightest channel but exhibits a very narrow dynamic range; the green channel, I_γ, has the best contrast (the edge of retinal features, such as exudates, optic disc, and blood vessels, are brighter than in the other channels); the blue channel, I_β, is nonzero mostly in the optic disc and the white spot areas.

Given a reflectance component R, a band ratioing between green R_γ and red R_ρ channels is applied pixel-by-pixel. By ratioing these bands, a new gray-level image, $\gamma\rho$, which emphasizes the features of interest, is obtained. Finally, $\gamma\rho_{ref}$ and $\gamma\rho_{reg}$, obtained band ratioing R_{ref} and R_{reg}, are subtracted pixel-by-pixel to generate two "difference images",

$$D_1 = \gamma\rho_{ref} - \gamma\rho_{reg} \qquad D_2 = \gamma\rho_{reg} - \gamma\rho_{ref}. \tag{5}$$

2.3.2. Multiclassifier Approach

To compensate for local illumination variations not compensated by the homomorphic filtering, an innovative multiclassifier approach is proposed. A thresholding approach for change detection is not applied to the whole "difference image" but to a set of randomly selected subimages. Square windows are randomly generated: They are centered in randomly selected pixels, which are uniformly distributed. As a result, the windows partially overlap.

Each window corresponds to a single classifier: The thresholding approach (see Section 2.3.3) is applied to each subimage and a change submap is obtained. All the pixels included within a subimage are classified into two different classes (i.e., "change" or "nochange") in the corresponding change submap. The information stored in each change submap needs to be combined in a global change map. Hence, a fusion of the label outputs ("change" or "nochange" labels for each pixel) obtained on the different windows is performed. For each pixel, all the corresponding classifiers (i.e., the windows that include it) vote for "change" or "nochange". The classification decision is taken using a nonweighted sum of the votes. Here, a majority vote is used because we assume that each classifier has the same probability of correct classification, p_{cc}. Indeed, the windows have the same dimension and only their spatial location is different, which does not influence p_{cc}.

Being the illumination within each subimage more uniform than within the entire image, the change detection results obtained by each classifier are less influenced by the illumination inhomogeneity. Therefore, the proposed method compensates for the local illumination differences between the two acquisitions and is expected to improve the change detection accuracy, especially in the external regions of the image, which are generally darker and, hence, provide poor information.

147

2.3.3. Thresholding

Changes are detected in each subimage (see Section 2.3.2) adopting a generalization of the K&I unsupervised thresholding algorithm (Kittler and Illingworth, 1986).

A thresholding approach is a simple classification procedure involving only one input feature, namely, the grey level of a scalar image. Here, such operator is applied to the "difference images" D_1 and D_2. The key issue is to choose the threshold to minimize the number of misclassified pixels. Being the approach unsupervised, the prior probabilities P_1 and P_2 and the parameters of the conditional probability density functions (pdfs) p_1 and p_2 of the classes $\omega_1 =$ "nochange" and $\omega_2 =$ "change" cannot be estimated through a training set. As a consequence, in place of the global grey level pdf of the difference feature z,

$$p_z(Z) = P_1 p_1(Z) + P_2 p_2(Z), \quad Z \in \mathbb{R}, \tag{6}$$

the histogram $h(Z)$ ($Z = 0, ..., L - 1$) of the considered difference image, D, is used (L denotes the number of quantization levels in D). The selection of an appropriate threshold τ on $[0; L-1]$ is based on the optimization of a given criterion function $J(\tau)$ which averages a cost function $c(\cdot, \tau)$ over $h(\cdot)$ (Chi et al., 1996). Kittler and Illingworth (1986) proposed a thresholding algorithm whose cost function is based on the Bayes decision theory. The minimum-error classification rule is adopted, under the Gaussian assumption for the class-conditional pdfs (i.e. $p_i(\cdot) = N(m_i, \sigma_i^2)$, where m_i and σ_i^2 are the ω_i-conditional mean and variance, respectively; $i = 1, 2$). Under this hypothesis, the only parameters to be estimated are the class prior probabilities P_i, means m_i, and variances σ_i^2, $i = 1, 2$.

According to the "maximum a posteriori probability" rule, $P(\omega_i|Z)$ ($i = 1, 2$) are to be maximized. This task is formulated introducing the following cost function (Kittler and

Illingworth, 1986)

$$c(Z, \tau) = \frac{[Z - \hat{m}_i(\tau)]^2}{2\hat{\sigma}_i^2(\tau)} - 2\ln\frac{\hat{P}_i(\tau)}{\hat{\sigma}_i(\tau)}, \qquad (7)$$

with $i = 1$ for $z \leq \tau$ and $i = 2$ for $z > \tau$. $\hat{P}_i(\tau)$, $\hat{m}_i(\tau)$ and $\hat{\sigma}_i^2(\tau)$ are histogram-based estimates of the class parameters and depend on τ $(i = 1, 2)$. The resulting criterion function is

$$J(\tau) = \sum_{Z=1}^{L-1} h(Z) \cdot c(Z, \tau) = 1 + 2\sum_{i=1}^{2} \hat{P}_i(\tau) \ln\frac{\hat{\sigma}_i(\tau)}{\hat{P}_i(\tau)}. \qquad (8)$$

The optimal threshold τ^* is chosen as to minimize $J(\cdot)$ over $0, 1, ..., L - 1$. The criterion function behavior is strongly related to the scene characteristics, represented by $h(\cdot)$. Typically, only one minimum in the interval $[0, L - 1]$ implies histogram bimodality, which reflects the presence of two classes (e.g., "change" and "nochange") in the scene. In the case of histogram monomodality a minimum is not identified, hence all the pixels are classified as "nochange" (i.e., $\tau = L$). Indeed, the window, in which the thresholding is applied, is assumed here to be larger than the maximum change area to be detected and, hence, to contain "nochange" pixels.

2.3.4. Change Classification

The change map obtained from the previous step is further classified into different categories, corresponding to the different change typologies (red vs white spots). Our aim is to detect certain types of pigmentation changes that are clinically relevant for diabetic retinopathy. The considered types of color changes are: Appearing/disappearing red spots, which generally correspond to bleedings/microaneurysms, and appearing/disappearing white spots, generally due to exudates/cotton wool spots (we will refer to these typologies as to new/old red and white spots).

To this end, each pixel is described by a set of features. Here, the feature space consists

149

of the green/red ratio, $\gamma\rho$, and the green channel, I_γ, for both images. The "white spot" and the "red spot" labels are assigned by comparing the intensities of these features to corresponding thresholds. Fig. 2 shows the architecture of the proposed subclassification step.
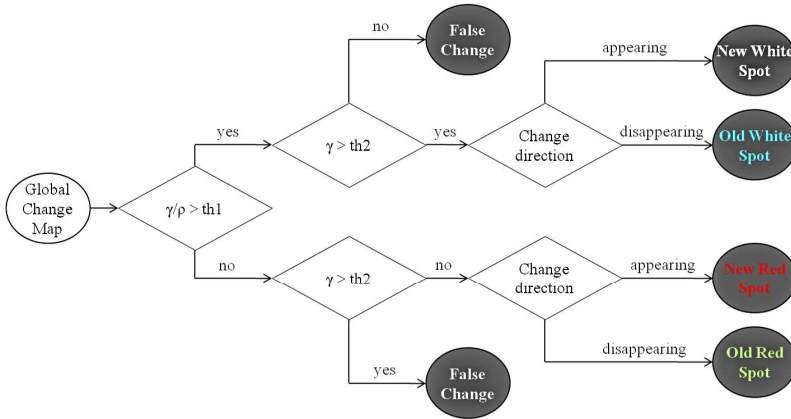

Figure 2: Block diagram of the change classification step.

The thresholds in this diagram are selected using an interactive approach, starting from the average values of the corresponding features. A trial-and-error approach is used by varying the threshold, with an excursion of 30% of the average value, in order to optimize the results from a visual view-point.

The method proposed here is simple and interactive and few parameters have to be set by a human expert. This approach is preferable to a supervised classification, because it encourages the data interpretability.

3. Experimental Results

The proposed method was tested on 22 pairs of multitemporal retinal images, which are RGB 8-bit color images of size 1280×1024 pixels, captured by a ZEISS FF 450plus IR

Fundus Camera with VISUPAC/System 451, connected to a JVC digital camera.

The images were taken in different medical visits from patients attending a retinopathy screening service and can present haemorrhages, microaneurysms, or exudates.

3.1. Registration

The 22 image pairs to be registered were preprocessed and the vessel maps, of both input and reference image, were extracted. Some differences in the maps, due to different illuminations, determined a low MOM value. Fig. 3 shows registration results of the first

(a) MOM

(b) I_A (c) I_B (d) Manual   (e) Automatic
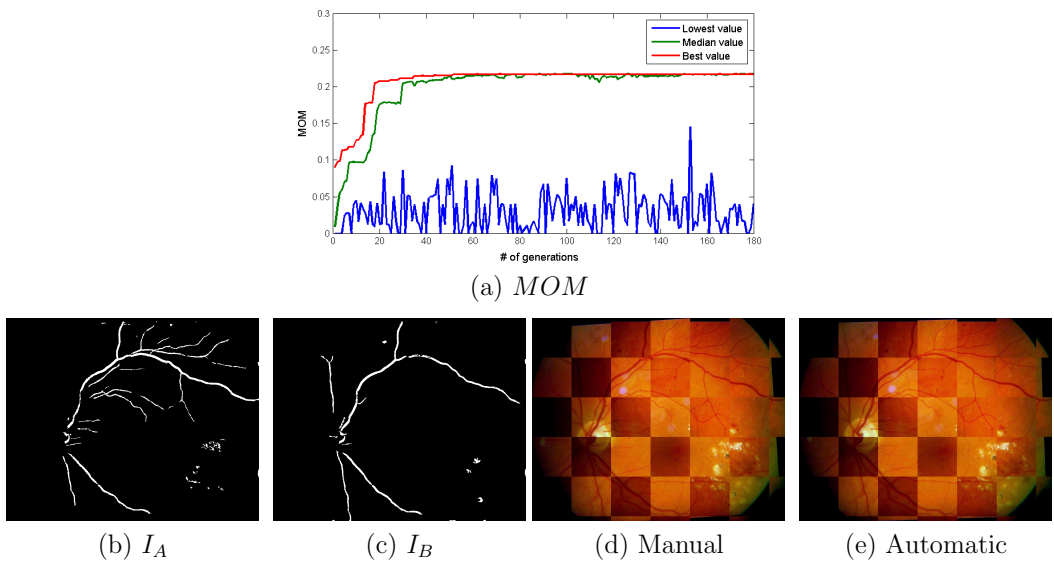
Figure 3: First dataset.(a) Measure Of Match (MOM) of the individuals among the generations. The blue, the green, and the red line represent the lowest, the median, and the highest value in the population, respectively. (b) Input and (c) reference image vessel maps. (d) Manual and (e) automatic registration shown by a checkerboard representation, in which checkers are alternately taken from I_{ref} and I_{reg}.

image pair, which presents differences in illumination and viewpoint. Spots also appeared from the first visit to the second one. Consequently, the vessel maps (b) and (c) exhibit large differences; nevertheless, the MOM convergence is steadily achieved, as shown in (a).

By a visual analysis of the results (d) and (e), one may note very good vessel continuity in border regions between a checker and its neighbors (i.e., where the vessel maps overlap).

A correct registration was achieved by the proposed method for all the 22 image pairs, despite a low MOM value at convergence.

3.2. Change Detection

3.2.1. Performance Evaluation

The quality assessment of a change detection system in the medical field is not an easy task. In order to evaluate the performance of the proposed change detection approach, the obtained results were compared to the performance of a human grader. A test map was created for each image pair, with the support of a specialist.

A quantitative evaluation of the results is performed in terms of Sensitivity (Sn) and Specificity (Sp). Sn is evaluated both in terms of pixels (SnP) and in terms of regions (SnR). In particular, SnP is the percentage of pixels correctly labeled as "change" in the change map over the number of "change" pixels in the test map, as determined by a human observer (i.e., it is an estimate of the detection probability (Duda et al., 2001)). SnR is the percentage of regions correctly identified as "change" in the change map over the number of "change" regions in the test map, irrespective of the specific number of correctly labeled pixels inside the regions. The Specificity (Sp) is the percentage of pixels correctly labeled as "nochange" in the change map (i.e., it is an estimate of $(1 - P_F)$, where P_F is the false-alarm probability (Duda et al., 2001)).

3.2.2. Preliminary Experiments

A few parameters of the multiclassifier approach need to be set. To this aim, preliminary experiments were carried out. The classification window size, S_W, is an important parameter

to set. The appropriate choice of S_W depends on the illumination inhomogeneity between the image pair and the expected size of the change regions. The windows should be small enough to guarantee homogeneous illumination in the area that they include. Meanwhile, S_W should be larger than the change areas to be detected. In order to estimate the proper value, several trials were done varying S_W in a wide range. Fig. 4 shows the behavior of the evaluation parameters (described in Sec. 3.2.1) versus S_W. Both SnP and SnR values
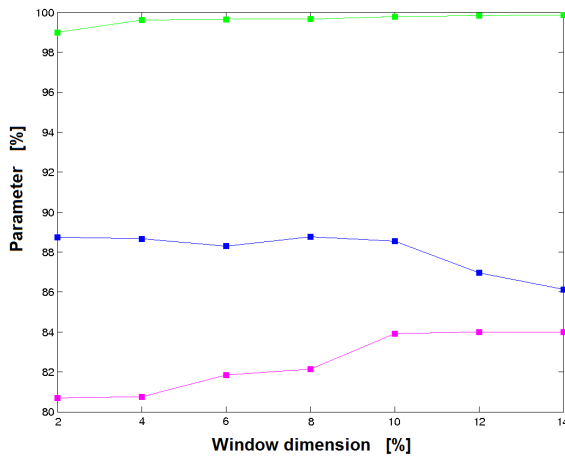
Figure 4: Performance parameter behavior versus S_W (expressed as a percentage of the entire image) for a selected dataset. The pink, the blue, and the green lines represent SnP, Sp, and SnR, respectively.

increase using classification windows of larger dimension. These parameters converge to their maximum value for window areas about 10% of the original image. Differently, Sp reaches its maximum value using windows that cover about 8-10% of the original image. Hence, S_W was set to 10% of the analyzed image pair.

Another parameter to set is the number of windows to be used, which influences the average number of votes per pixel. As the number of votes per pixel increases, the performance of the method improves, until reaching a certain value vpp. From experimental results vpp is about 30 votes per pixel. Here, 400 windows were generated, which give us about 40 votes

Table 1: Performances of BA, KEI, and MC applied to our datasets, in terms of SnP, Sp, and SnR.

Method	BA	BA	BA	KEI	KEI	KEI	MC	MC	MC
Parameter	SnP	Sp	SnR	SnP	Sp	SnR	SnP	Sp	SnR
Average	56%	87%	91%	54%	91%	94%	59%	92%	96%

per pixel on the average.

3.2.3. Results

The proposed change detection algorithm has been tested on all the registered image pairs.

For comparison purposes, a method for change detection based on a Bayesian Algorithm (BA) proposed in Narasimha-Iyer et al. (2006) was implemented and tested on our data set. The change maps were obtained by comparing the normalized sum square of the differences within a neighborhood (Aach and Kaup, 1995), see Narasimha-Iyer et al. (2006) for more details. That approach was chosen for comparison, being the only previous work for retinal change detection. Moreover, the results obtained by the proposed multiclassifier approach (MC) were also compared with the change maps obtained by applying K&I to the entire image (KEI). Table 1 shows the quantitative evaluation of the results obtained by BA, KEI, and MC. Specificity values (Sp) obtained applying either BA, KEI, and MC are very high also because the number of true negatives is always high. Moreover, Sp values produced by KEI and MC are higher than the ones obtained by BA. Differently, Sn is more variable because it strictly depends on the quality of the analyzed images and is thus affected by sharp differences in the image dynamics at the two dates. Sensitivity values (Sn), assessed both in terms of pixels (SnP) and of regions (SnR), produced by MC are higher than the ones obtained applying BA and KEI. In fact, the use of multiple classifiers avoids the presence of wide false alarm areas, otherwise caused by illumination differences. In all

154

(a) I_{ref}

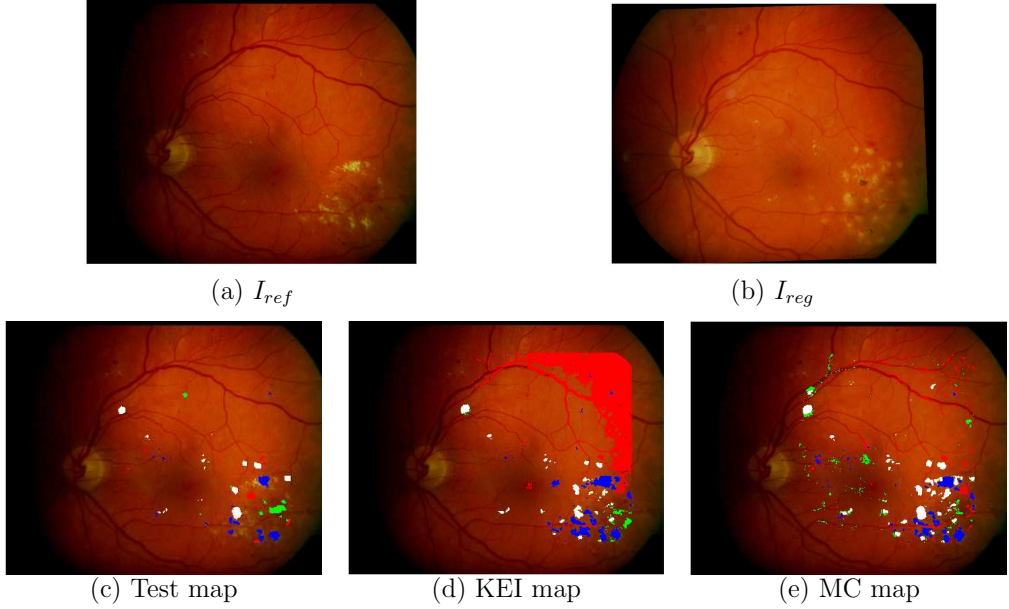(b) I_{reg}

(c) Test map

(d) KEI map

(e) MC map

Figure 5: First dataset: (a) and (b) registered images acquired two years apart. (c) Test map, (d) KEI change map, and (e) MC change map. The change maps are shown transparently superposed to the first image. Map legend: White = old white spots, red = old red spots, blue = new white spots, green = new red spots, background = "nochange".

cases, Sn values are higher in terms of regions. In fact, the presence and the position of most "change" areas are correctly detected, even when their shape is not perfectly reconstructed.

Figs. 5(d)-(e) show the change maps generated by KEI and MC when applied to the first dataset (Figs. 5(a) and (b)). Several typologies of change are present in this dataset, including new and old spots of both types: Fig. 5(c) shows the related test map. Few missed alarms appear in correspondence of edges between "change" and "nochange". Anyway, the detection of the changes and their classification, which is our aim (representing clinically relevant information), are achieved.

Moreover, results obtained applying MC to another dataset (Figs. 6(a) and (b)) are shown in Fig. 6(d). Fig. 6(c) shows the correspondent test map.
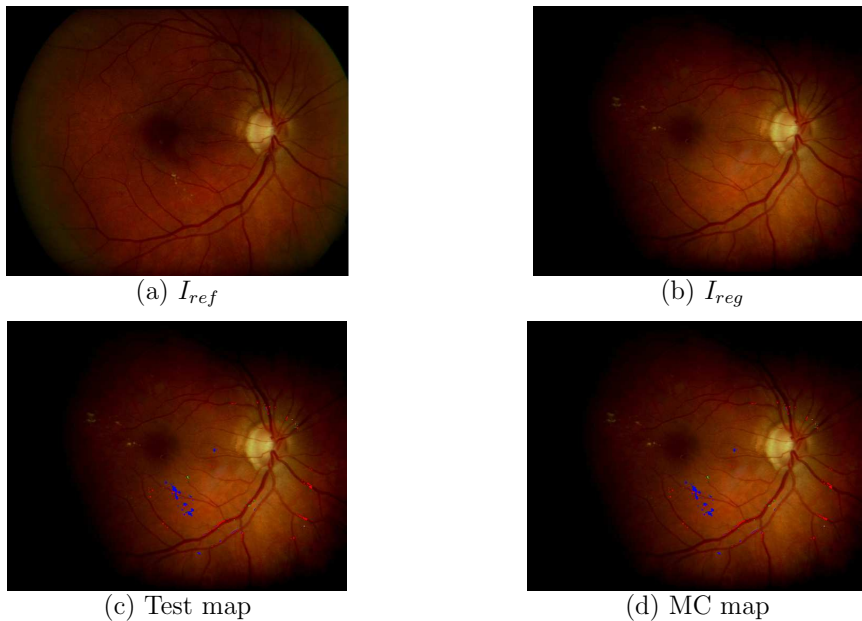
155

(a) I_{ref}

(b) I_{reg}

(c) Test map

(d) MC map

Figure 6: Fifth dataset: (a) and (b), acquired one year apart. (c) Test map, and (d) MC change map.

4. Conclusions

In this paper, an automatic technique has been proposed for retinal image registration and change detection. Different types of images, including changes of different sizes and typologies, were taken into account to test the performances of the proposed method. Accurate results were achieved. The registration accuracy, as compared to manual registration, has been evaluated by visual inspection of the results. A correct registration was obtained for all the image pairs.

The Kittler & Illingworth's thresholding technique, developed in the context of computer vision and previously applied to change detection problems on other typologies of images (Melgani et al., 2002; Moser and Serpico, 2006), has proven to be effective when locally applied to retinal images here. In particular, the multiclassifier approach (based on

K&I applied to randomly selected windows) provided accurate results, compensating for local illumination differences.

In our experiments, very good change detection accuracies were obtained for the analyzed images, for which the preprocessing phase effectively corrected the geometrical and radiometrical discrepancies between the two acquisition dates and the multiclassifier approach compensated for the local illumination differences. The main drawback is the possible sensitivity to the presence of undesired modes, such as artifacts and glares. The development of a method to automatically identify ungradable images may be an important next step of this research.

The proposed method integrates image registration and change detection. Retinal changes, which may occur between different medical visits, can be detected without the supervision of the ophthalmologists. A specialist will be consulted only in the case that temporal changes are detected by the proposed method.

Acknowledgment

References

Aach, T., Kaup, A., 1995. Bayesian algorithms for adaptive change detection in image sequences using markov random fields. Signal Processing: Image Communication 7, 147–160.

Arun, C.S., Al-Bermani, A., Stannard, K., Taylor, R., 2009. Long-term impact of retinal screening on significant diabetes-related visual impairment in the working age population. Diabet Med. 26, 489–492.

Ballerini, L., 1997. Temporal matched filters for integration of ocular fundus images, in: IEEE Conference on Digital Signal Processing, pp. 1161–1164.

Bek, T., Lund-Andersen, H., Hansen, A.B., Johnsen, K.B., Sandbaek, A., Lauritzen, T., 2009. The prevalence of diabetic retinopathy in patients with screen-detected type 2 diabetes in denmark: the addition study. Acta Ophthalmol. 83, 270–274.

Brinkmann, B., Manduca, A., Robb, R., 1998. Optimized homomorphic unsharp masking for mr grayscale inhomogeneity correction. IEEE Trans. on Medical Imaging 17, 161–171.

Brown, L., 1992. A survey of images registration techniques. ACM Comput. Surv. 24.

Can, A., Stewart, C.V., Roysam, B., Tanenbaum, H.L., 2002. A feature-based, robust, hierarchical algorithm for registering pairs of images of the curved human retina. IEEE Transactions on Pattern Analysis and Machine Intelligence 24, 347–364.

Chanussot, J., Mauris, G., P.Lambert, May 1999. Fuzzy fusion techniques for linear features detection in multitemporal SAR images. IEEE Transactions on Geoscience and Remote Sensing 37.

Chi, Z., Yan, H., Pham, T., 1996. Fuzzy Algorithms: with Applications to Image Processing and Pattern Recognition. World Scientific Publishing, Singapore.

Cree, M.J., Olson, J.A., McHardy, K.C., Sharp, P.F., Forrester, J.V., 1997. A fully automated comparative microaneurysm digital detection system. Eye 11, 622–628.

Duda, R., Hart, P., Stork, D., 2001. Pattern Classification. 2nd edition, Wiley, New York.

van den Elsen, P.A., Pol, E.J., Viergever, M.A., 1993. Medical image matching: A review with classification. IEEE Engineering for Medicine and Biology Society Magazine 12, 26–39.

Fritzsche, K., Can, A., Shen, H., Tsai, C., Turner, J., Tanenbuam, H., Stewart, C., Roysam, B., 2003. Automated model based segmentation, tracing and analysis of retinal vasculature from digital fundus images, in: Suri, J.S., Laxminarayan, S. (Eds.), State-of-The-Art Angiography, Applications and Plaque Imaging Using MR, CT, Ultrasound and X-rays. Academic Press, pp. 225–298.

Kittler, J., Illingworth, J., 1986. Minimum error thresholding. Pattern Recognition 19, 41–47.

Kristinsson, J.K., Gottfredsdottir, M.S., Stefansson, E., 1997. Retinal vessel dilatation and elongation precedes diabetic macular oedema. British Journal of Ophthalmology 81, 274–278.

Kuncheva, L.I., 2004. Combining pattern classifiers: Method and algorithms. Wiley Interscience, New Jersey.

Lalibert, F., Gagnon, L., Sheng, Y., 2003. Registration and fusion of retinal imagesan evaluation study. IEEE Transactions on Medical Imaging 22, 661–673.

Matsopoulos, G., Mouravliansky, N., Delibasis, K., Nikita, K., 1999. Automatic retinal image registration scheme using global optimization techniques. IEEE Transactionson on Information Technology in Biomedicine 3, 47–60.

Melgani, F., Moser, G., Serpico, S.B., 2002. Unsupervised change detection methods for remote sensing images. Optical Engineering 41, 3288–3297.

Michalewicz, Z., 1999. Genetic Algorithms + Data Structures = Evolutiona Programs. Springer Verlag, Berlin Heidelberg. third edition.

Moser, G., Serpico, S., 2006. Generalized minimum-error thresholding for unsupervised change detection from sar amplitude imagery. IEEE Transactions on Geoscience and Remote Sensing 44, 3695–3705.

Mouravliansky, N., Matsopoulos, G., Delibasis, K., Nikita, K., 1998. Automatic retinal registration using global optimization techniques, in: IEEE Engineering in Medicine and Biology Society, pp. 567–570.

Narasimha-Iyer, H., Can, A., Roysam, B., Stewart, C., Tanenbaum, H., Majerovics, A., Singh, H., 2006. Automated analysis of longitudinal changes in color retinal fundus images for monitoring diabetic retinopathy. IEEE Transactions on Biomedical Engineering 53, 1084–1098.

Newsom, R., Sinthanayothin, C., Boyce, J., Casswell, A., Williamson, T., 2000. Clinical evaluation of local contrast enhancement for oral fluorescein angiograms. Eye 14, 318–323.

Oppenheim, A., Schafer, R., Stockham, T.G., J., 1968. Nonlinear filtering of multiplied and convolved signals. Proceedings of the IEEE 56, 1264–1291.

Ritter, N., Owens, R., Cooper, J., Eikelboom, R., Saarloos, P.V., 1999. Registration of stereo and temporal images of the retina. IEEE Transactions on Medical Imaging 18, 404–418.

Spencer, T., Olson, J., McHardy, K., Sharp, P., , Forrester, J., 1996. An image-processing strategy for the segmentation and quantification of microaneurysms in fluorescein angiograms of the ocular fundus. Computers and Biomedical Research 29, 284–302.

Spencer, T., Phillips, R., Sharp, P., Forrester, J., 1992. Automated detection and quantification of microaneurysms in fluorescein angigraefes. Graefe's Archive for Clinical and Experimental Ophthalmology 230, 36–41.

Stefansson, E., Bek, T., Porta, M., Larsen, N., Kristinsson, J.K., Agardh, E., 2009. Screening and prevention of diabetic blindness. Acta Ophthalmol. Scand. 78, 374–385.

Toth, D., Aach, T., Metzler, V., 2000. Illumination-invariant change detection, in: IEEE Southwest Sym-

posium Image Analysis and Interpretation, pp. 3–7.

Troglio, G., Alberti, M., Benediktsson, J.A., Moser, G., Serpico, S.B., Stefansson, E., 2010. Unsupervised change-detection in retinal images by a multiple-classifier approach, in: El Gayar, N., Kittler, J., Roli, F. (Eds.), Multiple Classifier Systems, Springer Berlin / Heidelberg, Cairo, Egypt. pp. 94–103.

Troglio, G., Benediktsson, J.A., Serpico, S.B., Moser, G., Karlsson, R.A., Halldorsson, G.H., Stefansson, E., 2008. Automatic registration of retina images based on genetic techniques, in: IEEE Engineering for Medicine and Biology Conference, Vancouver, BC. pp. 5419–5424.

Usher, D., Dumskyj, M., Himaga, M., Williamson, T.H., Nussey, S., Boyce, J., 2003. Automated detection of diabetic retinopathy in digital retinal images: a tool for diabetic retinopathy screening. Diabetic Medicine 21, 84–90.

Walter, T., Klein, J.C., Massin, P., Erginary, A., 2002. A contribution of image processing to the diagnosis of diabetic retinopathy - detection of exudates in color fundus images of the human retina. IEEE Transactions on Medical Imaging 21, 1236–1243.

Appendix C

Paper 3

G. Troglio, J. Le Moigne, J. A. Benediktsson, G. Moser, and S. B. Serpico. "Automatic Extraction of Ellipsoidal Features for Planetary Image Registration," *IEEE Geoscience and Remote Sensing Letters*, submitted.

Automatic Extraction of Ellipsoidal Features for Planetary Image Registration

Giulia Troglio, *Student Member, IEEE,* Jacqueline Le Moigne, *Senior Member, IEEE,* Jon A. Benediktsson, *Fellow, IEEE,* Gabriele Moser, *Member, IEEE,* and Sebastiano B. Serpico, *Fellow, IEEE*

Abstract— With the launch of several planetary missions in the last decade, a large amount of planetary images has already been acquired and much more will be available for analysis in the coming years. The image data need to be analyzed, preferably by automatic processing techniques because of the huge amount of data. Although many automatic feature extraction methods have been proposed and utilized for Earth remote sensing images, these methods are not always applicable to planetary data that often present low contrast and uneven illumination characteristics. Here, we propose a new unsupervised method for the extraction of different features of elliptical and geometrically compact shape from the surface of the analyzed planet. This approach is based on the combination of several image processing techniques, including a watershed segmentation and the generalized Hough transform. In particular, craters and rocks of compact shape (e.g., boulders) can be extracted. The method has many applications, first of all image registration, and can be applied to arbitrary planetary images.

Index Terms— Crater Detection, Feature Extraction, Watershed Segmentation, Hough Transform.

I. Introduction

With each new planetary mission, the volume of acquired data significantly increases. Different types of data are being collected at different times, by different sensors, and from different view-points: Multitemporal, multimodal and stereo-images need to be analyzed. Therefore, image registration is an essential task to jointly exploit, integrate, or compare all these different data. Feature extraction, i.e., extraction of spatial features in the images, is the first step in the image registration process. Furthermore, the feature extraction is important for further analysis of the data.

In this paper, the extraction of spatial features in planetary images is addressed. In particular, ellipsoidal features, such as craters and rocks, are detected for registration purposes.

Identification of spatial features on planetary surfaces can be manually performed by human experts but this process can be very time consuming. Therefore, a reliable automatic approach to detect the position, structure, and dimension of each feature is highly desirable. This is a difficult task for several reasons: Limited data are usually available, the quality of the images is generally uneven (i.e., it depends on illumination, surface

properties, and atmospheric state), and the features that are present in the images can be barely visible due to atmospheric erosion and they may be based on different structure types of variable sizes.

Among the typical features in planet-surface imagery, craters play a primary role. Detection of craters has been widely addressed and different approaches have recently been proposed in the literature, based on the analysis of planetary topography data [1], satellite images [2] in the visible spectrum and the infrared spectrum. Here, we focus on optical image-based approaches for crater and rock detection. The existing techniques can be divided into two main categories: Super-vised and unsupervised. Supervised methods require input labeled data to train the algorithm for feature extraction. Unsupervised methods do not involve any training process and search for the structures of interest in the image. Different approaches have been presented, based on template match-ing [2], [3], texture analysis [4], neural networks [5], [6], boosting approaches [7], or a combination of these tech-niques [8], [9]. In particular, in [10], the identification of impact craters was achieved through the analysis of the probability volume created as a result of a template matching procedure. Such methods enable the identification of round spatial features with shadows. Kim and Muller [4] presented a crater detection method based on texture analysis and ellipse fitting. That method was not robust when applied to optical images, hence it was performed by using fusion techniques exploiting both DEM and optical images. In subsequent work [11], in order to automatically detect craters on Mars, the authors proposed a combination of edge detection, template matching, and supervised neural network-based schemes for the recognition of false positives. In a different approach, Martins et al. [12] adopted a supervised boosting algorithm, originally developed by Viola and Jones [13] in the context of face detection, to identify craters on Mars. In [14], Urbach and Stepinski presented a different approach for crater detection in panchromatic planetary images. The method in [14] is based on using mathematical morphology for the detection of craters and on supervised machine learning techniques to distinguish between objects and false alarms.

Other typical features in planetary images are represented by rocks. Rock detection in ground imagery has been addressed in the literature. In particular, in [15] the authors presented a supervised method for segmentation, detection and classi-fication of rocks on data collected by rovers. That approach, based on a probabilistic fusion of data from multiple sensor sources, was tested on Earth data (collected in the Atacama

desert in Chile). In [16], the same authors tested different rock detection approaches on Mars Exploration Rover data. In [17], the authors addressed rock detection by using a segmentation method on data collected by the Spirit Mars Rover Planetary Camera. That approach incorporates multiple scale attributes, which include local attributes (e.g., texture), object attributes (e.g., shading), and scene attributes (e.g., illumination direction). Moreover, in [18], the authors proposed an automatic algorithm for rock detection both on ground imagery and on HiRISE data, based on cylinder fitting.

Also the detection of other types of planetary features, which is not relevant for this letter, has been addressed (e.g., detection of volcanoes on Venus [19], polygonal patterns on Mars [20], valley networks on Mars [21]).

Registration of planetary images has been addressed in the literature as well. Kim et al. [22] proposed a method for crater extraction from MDIM and MOLA tracks, for their alignment. However, registration errors occurred due to shape distortions of the detected craters. In [23] a method for the automatic recognition of impact craters on Mars was proposed and applied to remeasure the coordinates of big craters (exceeding 10 km in diameter) in a catalogue. Lin et at. [24] proposed a method for the co-registration of topographic data by surface matching. Nonetheless, here, we focus on the analysis of optical data.

In order to overcome the typical problems of planetary images with limited contrast, poor illumination, and a lack of good features, we propose here a new unsupervised region-based approach for the extraction of different planetary features. The main contribution of this paper is a novel feature extraction approach for the unsupervised identification of planetary images, aimed at extracting curvilinear features, relevant for this typology of images as a typical model for craters and rocks. In particular, the proposed approach is based on a novel combination of robust image processing techniques, such as the Canny operator, the Hough transform, and the watershed. Moreover, the approach allows not only to locate the features, but also to reconstruct their shape.

II. THE PROPOSED APPROACH

Planetary images show the surface of a planet and its structures. The aim here is to automatically detect the different structures that are present on a considered planetary surface by using image analysis techniques. The extracted features could then be used for image registration purposes, as will be shown in Section III.

Different types of features are present in the planetary images, and their sizes, shapes and positions are estimated by applying different methods. The extracted features can be used for registration purposes, as will be shown in Section III.

The main features to be extracted are craters and rocks. Craters are objects of approximately elliptical (and generally circular) shape with shadows, due to their deep concave shape and uneven illumination. Rocks have small elliptical shape, with almost no shadows, because of their convex shape. The extraction of these spatial features is a difficult task, because planetary images are blurry, quite noisy, present lack of contrast and uneven illumination, and the represented objects are

not well defined. For these reasons, a region-based approach, based on segmentation, has been chosen in order to address such problems. Segmentation is the process of partitioning an image into multiple regions, for instance, in order to distinguish objects from the background. A frequent approach to segmentation introduces a set of characteristic points that are related to the objects to be detected, automatically selected and used as "seed points" to segment the images. Many segmentation approaches have been explored in the literature. Here, the watershed algorithm, presented by Beucher in [25], has been chosen, a method which is automatic, robust and fast. The basic concept of watershed segmentation is giving a topographic representation of a grey-level image (i.e., the grey level of a pixel represents its elevation). A flooding process starts from the minima of the image in terms of elevation, so that the merging of the flooding coming from different sources is prevented. As a result the image is partitioned into two different sets: The catchment basins (i.e., the regions) and the watershed lines (i.e., the region boundaries). The flowchart of the proposed technique for feature extraction is shown in Figure 1.
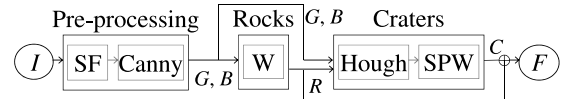

Fig. 1. Flowchart of the proposed approach.

Before applying feature extraction techniques, the input image I needs to be preprocessed. First, the noise is reduced by a Smoothing Filter, SF. Then, in order to detect edges, the image gradient is computed by using the Canny edge detector [26]. As an intermediate result of this operation an intensity gradient, G, is generated. Then, by applying a non-maximum suppression algorithm followed by an hysteresis thresholding to G, a binary gradient image, B, is obtained but this image shows the contours of the objects represented in the original image.

Rocks generally appear like closed contours in B, because of the almost absence of shadows. In order to extract these features, the Watershed segmentation algorithm, W, is applied to B and closed contours are extracted. All the areas included within a closed contour correspond to "seed point-areas," and are identified as regions. The result of this first step is a binary image R that shows boundaries of small ellipsoidal features of regular shapes, such as rocks.

While rocks generally appear like closed contours and can be easily detected, craters have a more complex structure and, due to their depth and uneven illumination, often exhibit internal shadows. Their borders can be approximated with incomplete non-continuous elliptical curves. A generalized Hough accumulator [27] is used to identify the seed points to detect these structures from B. For every pair of pixels that are detected as edge points in B and exhibit opposite gradient directions (being the relation of opposition defined with tolerance ϵ), an accumulator, corresponding to the median point between them in the image plane, is incremented of a unit value. The maxima of the accumulator are taken as

centers of ellipses. The three parameters describing the ellipse centered in each detected maximum are then computed and a 3D accumulator is used to estimate the two semi-axes and the direction angle of the ellipse from all the pairs of points that contributed to the accumulator in the considered center. The center of each ellipse that has been generated is used as a seed point for segmentation. Starting from all the detected Seed Points, SPs, a Watershed algorithm, SPW, is applied to G and the craters are identified. G is used in this case because it represents not only the edges but also the elevation information. As a result, a binary image C that shows the boundaries of elliptical features, such as craters, that were not detected by the previous step. In a post-processing step, features are approximated by ellipses and their attributes (i.e., ellipse semi-axes and rotation angle) are estimated. Features with eccentricity $e > 0.6$ are discarded, being features of larger e unlikely to be either craters or rocks. A binary image, F, which represents the contours of all detected features, is created. The binary image, F, shows the boundaries of the features, identifies their locations and estimates their shapes.

The proposed technique for feature extraction can be used to register image pairs representing the same scene. For registration, two binary images (I_{ref} and I_{in}) need to be extracted from both images to be registered and their match can be estimated (in Section III an example of the application of the proposed approach to image registration is presented).

III. Experimental Results

Experiments were carried out using Mars data, collected both by the THermal EMission Imaging System (THEMIS), an instrument on board the Mars Odyssey spacecraft, and by the High Resolution Imaging Science Experiment (HiRISE) camera flying on the Mars Reconnaissance Orbiter (MRO), were used. THEMIS combines a 5-band visual imaging system with a 10-band infrared imaging system [28]. Both THEMIS visible (VIS) and infrared (IR) images, with resolutions of 18 meters and 100 meters per pixel, respectively, were used to test the proposed approach. For the experiments 5 VIS and 7 IR images were selected. Moreover, 9 HiRISE images (HR) were used, with resolution of about 0.3 meters per pixel. The name, location, and attributes of each test site are listed in I.

TABLE I

NAMES, LOCATION, ATTRIBUTES, AND NUMBER OF IMAGES N OF EACH SELECTED TEST SITE.

Site n°	Name	Lat	Lon	N
1	No description	14.7°S	175.4°E	4
2	No description	1.1°S	352.9°E	5
3	Kasei Valles	20.7°N	287.2°E	1
4	Ascreaus Mons	6.6°N	258.5°E	1
5	Iberus Vallis	21.5°N	151.5°E	1
6	Hesperia Planum	19.9°S	114.5°E	1
7	Pavonis Mons	0.5°S	251.5°E	1
8	Noctis Labyrinthus	8.2°S	260.4°E	1
9	Unnamed crater ray	15.9°S	151.9°E	1
10	Nili Fossae	19.4°N	75.6°E	1
11	Acidalia Planitia	38.1°N	319.5°E	1

Reference data were generated by manually analyzing each image of the data set and identifying all the craters and rocks that are present. Only objects completely included within the images were considered (i.e., objects cut by the borders of the image were discarded). No limits were imposed on the minimum dimensions of the features to be detected. A quantitative assessment of the obtained results by the proposed method was performed using these reference data. This was accomplished by comparing the obtained results with the labeled features in the correspondent Reference Map (RM), by the similarity measure proposed in [29]. Moreover, the Detection percentage D, the Branching factor B, and the Quality percentage Q were computed as follows:

$$D = \frac{100 \cdot TP}{TP + FN}; B = \frac{FP}{TP}; Q = \frac{100 \cdot TP}{TP + FP + FN}; \quad (1)$$

where True Positive (TP) is the number of detected features that correspond to labeled objects in RM, False Positive (FP) is the number of features detected by the proposed approach, which do not correspond to any object in RM, and False Negative (FP) is the number of objects in RM that have not been detected by the proposed approach. The global values of D, B, and Q and the total number of TP, FP, and FN obtained by the proposed approach for VIS, IR, and HR data are reported in Table II.

TABLE II

AVERAGE NUMERICAL PERFORMANCE OF THE PROPOSED APPROACH AS MEASURED BY DETECTION PERCENTAGE (D), BRANCHING FACTOR (B) AND QUALITY PERCENTAGE (Q).

Param	VIS	IR	HR	Overall	Rock	Crater
D	82%	78%	83%	81%	80%	81%
B	0.03	0.05	0.06	0.05	0.04	0.07
Q	81%	75%	79%	77%	78%	77%

The global values of D for VIS data, IR data, and HR data were about 82%, 78%, and 83%, respectively. These high values reflect good detection rates (i.e., high TP values). Furthermore, B was about $0,03$ for VIS, $0,05$ for IR, and $0,06$ for HR, which indicates in all cases a small amount of false detections with respect to true detections, thanks to the small FP values. Finally, relatively high Q values (i.e., about 81%, 75%, and 79% for VIS, IR, and HR, respectively) reflect a good overall algorithm performance. The same evaluation parameters obtained by testing the proposed approach on all the data sets were also expressed separately in Table II for rock and crater detections. The crater detection performance of the proposed approach in terms of D, B, and Q compares favorably with most of the results previously published for automatic crater detection methods [11], [14], [30]. The classification error, i.e., the percentage of feature classified in the wrong class (crater versus rock) over the total number of classified features is about 6%.

Visual results are shown for a partition of a single band VIS image (Figure 2-a). The grey level image is first preprocessed in order to reduce the noise. In particular, Gaussian and median filtering operations are applied in a cascade [31] in order to reduce the noise and, at the same time, preserve the edges. The Canny operator is applied to the smoothed image. Subsequently, in order to extract the rocks, a watershed
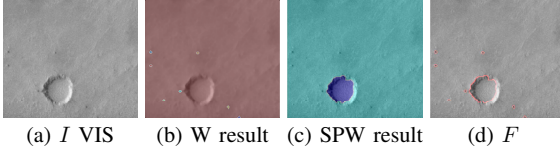
(a) I VIS   (b) W result   (c) SPW result   (d) F

Fig. 2.   Experimental results obtained by applying the proposed method to a VIS image. (a) Original image, (b) watershed segmentation applied to B, (c) watershed segmentation, using the maxima of the Hough accumulator as "seed points", and (d) detected features. Each color in the segmentation map denotes a different region.

(a) $I\,1$ (b) $I\,2$ (c) $I\,3$ (d) $I\,4$ (e) $I\,5$ (f) $I\,6$

(g) $F\,1$ (h) $F\,2$ (i) $F\,3$ (j) $F\,4$ (k) $F\,5$ (l) $F\,6$

Fig. 4.   Experimental results obtained by applying the proposed method to HR images.

algorithm is applied to the binary image gradient B. Rock segmentation results are shown in Figure 2-b. Then, the generalized Hough transform is computed (with $\epsilon = 5°$) and a watershed segmentation is applied, starting the flooding process from the ellipse centers and leading to the detection of the craters. The segmentation results are shown in Figures 2-c. Finally, the extracted features, including both rocks and craters, are combined into a binary map and shown in Figure 2-d, transparently superimposed to the original image. By a visual inspection, it is possible to appreciate the accuracy of both the detection and the reconstruction of the feature shape.

Visual results are also shown for a partition of the first band of an IR image (Figure 3-a). Figure 3-b shows the

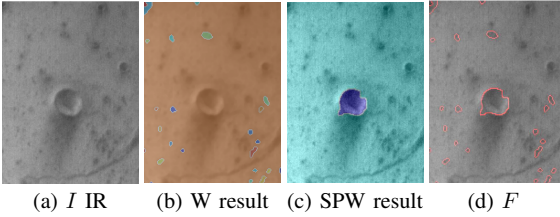(a) I IR   (b) W result   (c) SPW result   (d) F

Fig. 3.   Experimental results obtained by applying the proposed method to the first band of an IR THEMIS image.

segmentation results when watershed is applied to B. Figure 3-c shows the crater segmentation results. The different extracted features are combined and shown in Figure 3-d. In this example, not all the features are detected. This is because their contours were not extracted by the Canny operator. A modified edge detection approach which may improve the accuracy of the proposed method is currently under investigation. On the other hand, it is shown below that the detected features are enough to achieve an accurate registration.

Finally, visual results are also shown for different partitions of HR images. Figures 4-a to 4-f show the input data and Figures 4-g to 4-l show the contour maps in red superimposed on the correspondent inputs.

To demonstrate the applicability of the proposed method to registration, two different non-registered bands of an IR image are used as reference I_{ref} and input I_{in} images. In order to show the results, the same partition of Figure 3-a is used; in particular, the 4th and 5th bands were selected (Figures 5-a and 5-b, respectively). For both images, craters and rocks are detected and their contours are represented in binary feature
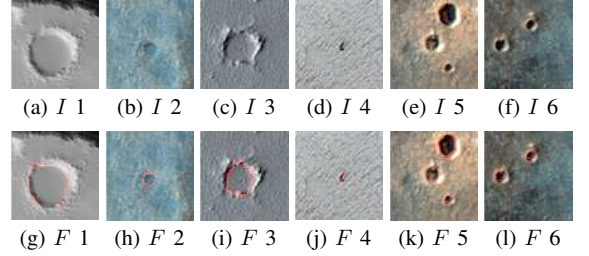

(a) I_{ref} (b) I_{in} (c) F_{ref} (d) F_{in} (e) F_{ref+in} (f) Results
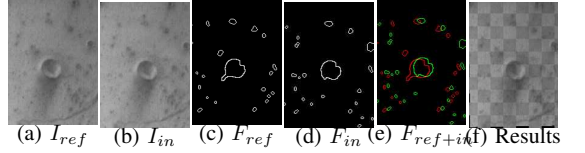
Fig. 5.   Experimental registration results for a partition of (a) the 4th and (b) the 5th bands of an IR image. (c) and (d) feature contours extracted from (a) and (b), respectively. (e) Feature contours superimposed and represented in a false-color composition (i.e., the green plane is (c), the red plane is (d), and the blue plane is identically zero). (f) Registration results, by using a checkerboard representation.

images, F_{ref} and F_{in}, as shown in Figures 5-c and 5-d, respectively. The rotation and translation between the two bands are visible by looking at Figure 5-e, in which the two non-registered feature images are superimposed in a false-color representation. The features extracted from I_{ref}, F_{ref}, are represented in green, whereas the I_{in} features, F_{in}, are shown in red. The registration scheme used in this phase was based on a global optimization technique aimed at estimating the optimum parameters of an image transformation model. The contour images, which represent the features of the two input image bands, were fed as inputs to an optimization module. The transformation matrix was to be optimized: Its goodness was evaluated by an objective function and its optimization was achieved by applying a genetic algorithm [32]. After the optimum matrix was estimated, it was used to transform and interpolate one of the two bands with respect to the other one. The co-registered bands are shown in Figure 5-f, by using a checkerboard representation: Each tile of the board represents the registered input band and the reference band, alternately. The registration accuracy can be evaluated by looking at the continuity of the features at the borders of the tiles. The visual analysis of Figure 5-f suggests that the registration performed very well; craters and ridges appear continuous at the borders, i.e., the points of overlap.

IV. CONCLUSIONS

In this letter a novel unsupervised region-based approach has been proposed for automatic detection of spatial features that characterize planetary surfaces. The proposed approach has been applied to the registration of planetary data.

The features to be extracted are not as well contrasted nor

defined as for Earth data. However, small rocks, which are not affected by uneven illumination, can easily be detected by the proposed approach. Crater detection is more difficult than rock detection, because of their depth and spatial extent and, consequently, their contours are often blurry and not continuous. Nevertheless, we showed here that their identification can be achieved and the proposed approach provided quite accurate results. The accuracy of the detection has been assessed by comparison to a manually generated reference map. The results in terms of several indices based on true and false positives compared favorably to previously proposed approaches. Moreover, we showed that the extracted features can be used to accurately register pairs of image bands acquired from the same sensor. The accuracy of the registration step is confirmed by visual inspection of the results.

The proposed approach represents the first important step for many applications dealing with all the various data that are being collected by different planetary missions, among which image registration and image analysis, with the aim of selecting safe landing sites, identifying lunar resources, and preparing for subsequent explorations of the Moon and Mars by both robots and humans.

In future, we plan to expand the experimental validation. The approach will be applied to different types of data and registration of multisensor images will be addressed.

In our future work we plan to integrate the shadow information around the features in order to improve the reliability of the edge detection and reduce the false alarms in the contour map F. Illumination correction, based on the knowledge of the orbital angle and the acquisition time, will be useful to reduce the bias in the reconstruction of the exact feature shape.

Furthermore, crater detection and rock detection could be addressed separately for specific applications. The different features could be distinguished in a post-processing step, by using the shape information. A crater detection algorithm able to detect features of small size would be useful to identify small craters. Craters that are not catalogued yet could be identified and this information would increase the importance of the already accurate but not complete Mars catalogues [33].

Finally, the proposed method could be used to extract other features of elliptical shape, such as volcanoes. Additionally, features of other shapes, such as ridges or polygonal patterns among others, could be extracted, by adapting the generalized Hough transform to the detection of the shape of interest.

References

[1] G. Salamuniccar and S. Loncaric, "Method for crater detection from martian digital topography data using gradient value/orientation, morphometry, vote analysis, slip tuning, and calibration," *IEEE Trans. Geosci. Remote Sens.*, vol. 48, pp. 2317–2329, 2010.

[2] A. Flores-Mendez, *Crater Marking and Classification using Compu. Vision.* New York: Springer-Verlag, 2003, vol. 2905.

[3] T. Barata, E. I. Alves, J. Saraiva, and P. Pina, *Automatic Recognition of Impact Craters on the Surface of Mars.* Berlin, Germany: Springer-Verlag, 2004, vol. 3212.

[4] J. R. Kim and J.-P. Muller, "Impact crater detection on optical images and DEM," in *ISPRS*, Houston, TX, 2003.

[5] A. A. Smirnov, "Exploratory study of automated crater detection algorithm," Boulder, CO," Tech. Rep., 2002.

[6] P. G. Wetzler, B. Enke, W. J. Merline, C. R. Chapman, and M. C. Burl, "Learning to detect small impact craters," in *IEEE WACV*, vol. 1, 2005, pp. 178–184.

[7] R. Martins, P. Pina, J. S. Marques, and M. Silveira, "A boosting algoritm for crater detection," in *Vis, Imaging, Image Process. Conf.*, Spain, 2008.

[8] Y. Sawabe, T. Matsunaga, and S. Rokugawa, "Automated detection and classification of lunar craters using multiple approaches," *Adv. Space Res.*, vol. 37, no. 1, pp. 21–27, 2006.

[9] J. Earl, A. Chicarro, C. Koeberl, P. G. Marchetti, and M. Milsen, "Automatic recognition of crater-like structures in terrestrial and planetary images," in *36th Annu. Lunar Planetary Sci. Conf.*, no. 1319, TX, 2005.

[10] L. Bandeira, J. Saraiva, and P. Pina, "Impact crater recognition on mars based on a probability volume created by template matching," *IEEE Trans. Geosci. Remote Sens.*, vol. 45, pp. 4008–4015, 2007.

[11] J. R. Kim, J.-P. Muller, S. van Gasselt, J. G. Morley, and G. Neukum, "Automated crater detection, a new tool for mars cartography and chronology," *Photogrammetric Eng. Remote Sens.*, vol. 71, no. 10, pp. 1205–1217, 2005.

[12] R. Martins, P. Pina, J. S. Marques, and M. Silveira, "Crater detection by a boosting approach," *IEEE Geosci. Remote Sens. Lett.*, vol. 6, pp. 127–131, 2009.

[13] P. Viola and M. Jones, "Robust real-time face detection," *Int. J. Compu. Vision*, vol. 57, pp. 137–154, 2004.

[14] E. R. Urbach and T. F. Stepinski, "Automatic detection of sub-km craters in high resolution planetary images," *Planetary Space Sci.*, vol. 57, pp. 880–887, 2009.

[15] D. Thompson, S. Niekum, T. Smith, and D. Wettergreen, "Automatic detection and classification of features of geologic interest," in *IEEE Aerosp. Conf.*, 2005, pp. 366–377.

[16] D. Thompson and R. Castano, "Performance comparison of rock detection algorithms for autonomous planetary geology," in *IEEE Aerosp. Conf.*, 2007, pp. 1–9.

[17] H. Dunlop, D. Thompson, and D. Wettergreen, "Multi-scale features for detection and segmentation of rocks in mars images," in *IEEE Conf. on Compu. Vision and Pattern Recognition*, 2007, pp. 1–7.

[18] M. P. Golombek, R. E. Arvidson, T. Heet, L. Barry, J. R. Matijevic, and A. S. McEwen, "Size-frequency distributions of rocks on the northern plains of mars in hirise images with special reference to phoenix landing sites," in *LPSC*, vol. 1405, TX, 2007.

[19] M. C. Burl, L. Asker, P. Smyth, U. Fayyad, P. Perona, J. Aubele, and L. Crumpler, *Machine Learning.* Boston, USA: Kluwer Academic Publishers, 1998, vol. 30, ch. Learning to Recognize Volcanoes on Venus, pp. 165–195.

[20] P. Pina, J. Saraiva, L. Bandeira, and T. Barata, "Identification of martian polygonal patterns using the dynamics of watershed contours," in *Int. Conf. Image Anal. Recognition*, 2006, vol. 4142, pp. 691–699.

[21] "Automatic mapping of valley networks on mars," *Compu. & Geosci.*, vol. 33, no. 6, pp. 728–738, 2007.

[22] J. R. Kim, J.-P. Muller, J. G. Morley, and K. L. Mitchell, "Automated registration of mdim with mola tracks," in *LPSC*, vol. 2087, TX, 2001.

[23] G. G. Michael, "Coordinate registration by automated crater recognition," *Planetary and Space Sci.*, vol. 51, pp. 563–568, 2003.

[24] S.-Y. Lin, J.-P. Muller, J. P. Mills, and P. E. Miller, "An assessment of surface matching for the automated co-registration of mola, hrsc and hirise dtms," *Earth Planetary Sci. Lett.*, vol. 294, pp. 520–533, 2010.

[25] S. Beucher, "The watershed transformation applied to image segmentation," *Scanning Microscopy Int.*, vol. 6, 1992.

[26] J. Canny, "A computational approach to edge detection," *IEEE Trans. Pattern Anal. Mach. Intell.*, vol. 10, no. 6, 1986.

[27] S. Tsuji and F. Matsumoto, "Detection of ellipses by a modified Hough transformation," *IEEE Trans. Comput.*, vol. 27, 1978.

[28] P. Christensen, B. M. Jakosky, H. H. Kieffer, M. C. Malin, H. Y. Mcsween, K. Nealson, G. L. M. S. H. Silverman, S. Ferry, M. Caplinger, and M. Ravine, "The thermal emission imaging system for the mars 2001 odyssey mission," *Space Sci. Rev.*, vol. 100, pp. 85–130, 2004.

[29] G. Salamuniccar and S. Loncaric, "Open framework for objective evaluation of crater detection algorithms with first test-field subsystem based on mola data," *Adv. Space Res.*, vol. 42, pp. 6–19, 2010.

[30] B. D. Bue and T. F. Stepinski, "Machine detection of martian impact craters from digital topography data," *IEEE Trans. Geosci. Remote Sens.*, vol. 45, pp. 265–274, 2007.

[31] L. G. Shapiro and G. C. Stockman, *Computer Vision.* Prentice Hall, 2001.

[32] Z. Michalewicz, *Genetic Algorithms + Data Structures = Evolution Programs*, 3rd ed. Berlin: Springer Verlag, 1999.

[33] G. Salamuniccar and S. Loncaric, "Gt-57633 catalogue of martian impact craters developed for evaluation of crater detection algorithms," *Planetary Space Sci.*, vol. 56, pp. 1992–2008, 2008.

Appendix D

Paper 4

G. Troglio, J. Le Moigne, J. A. Benediktsson, G. Moser, and S. B. Serpico. "Unsupervised Detection of Planetary Craters by a Marked Point Process," *IEEE Transactions on Geoscience and Remote Sensing*, submitted.

Unsupervised Detection of Planetary Craters by a Marked Point Process

Giulia Troglio, *Student Member, IEEE,* Jon A. Benediktsson, *Fellow, IEEE,* Jacqueline Le Moigne, *Senior Member, IEEE,* Gabriele Moser, *Member, IEEE,* and Sebastiano B. Serpico, *Fellow, IEEE*

Abstract— With the launch of several planetary missions in the last decade, a large amount of planetary images is being acquired. Preferably, automatic and robust processing techniques need to be used for data analysis because of the huge amount of the acquired data. Here, the aim is to achieve a robust and general methodology for crater detection. A novel technique based on a marked point process is proposed. First, the contours in the image are extracted. The object boundaries are modeled as a configuration of an unknown number of random ellipses, i.e., the contour image is considered as a realization of a marked point process. Then, an energy function is defined, containing both an a priori energy and a likelihood term. The global minimum of this function is estimated by using reversible jump Monte-Carlo Markov chain dynamics and a simulated annealing scheme. The main idea behind marked point processes is to model objects within a stochastic framework: Marked point processes represent a very promising current approach in the stochastic image modeling and provide a powerful and methodologically rigorous framework to efficiently map and detect objects and structures in an image with an excellent robustness to noise.

The proposed method for crater detection has several feasible applications. One such application area is image registration by matching the extracted features.

Index Terms— Crater Detection, Marked Point Process, Markov Chains, Simulated Annealing.

I. INTRODUCTION

With each new planetary mission, the volume of acquired data significantly increases. Different types of data are being collected at different times, by different sensors, and from different view-points.

Feature extraction, i.e., extraction of spatial features in the images, is typically the first step in most image analysis processes. For instance, registration is an essential task to jointly exploit, integrate, or compare all these different data and usually requires a prior accurate extraction of the spatial features in the image.

Identification of spatial features on planetary surfaces can be manually performed by human experts but this process can be very time consuming. Therefore, a reliable automatic approach to detect the position, structure, and dimension of each feature is highly desirable. This is a difficult task for several reasons: Limited data are usually available, the contrast of planetary images is generally low (i.e., it is heavily affected by illumination, surface properties and atmospheric state), and the features that are present in the images can be barely visible due to atmospheric erosion and they may be based on different structure types of variable sizes. Among the typical features in planet-surface imagery, craters play a primary role. Detection of craters has been widely addressed and different approaches have recently been proposed in the literature, based on the analysis of planetary topography data [1], satellite images in the visible spectrum and the infrared spectrum [2]. Here, we focus on optical image-based approaches for crater detection.

The existing techniques can be divided into two main categories; supervised and unsupervised. Supervised methods require the input of an expert and generally use supervised learning concepts to train the algorithm for feature extraction. These techniques contemplate a learning phase, in which a training set of images containing craters is labeled by human experts. Craters are then detected by applying the previously trained algorithm to new unlabeled sets of images. In [3], a continuously scalable

detector, based on a supervised template matching technique, is applied. In [4], different supervised learning approaches, including ensemble methods, support vector machines (SVM), and continuously-scalable template models, were employed to derive crater detectors from ground-truthed images. The SVM approach with normalized image patches provided the best detection and localization performance. In a different approach, Martins *et al.* [5] adopted a supervised boosting algorithm, originally developed by Viola and Jones [6] in the context of face detection, to identify craters on Mars.

Unsupervised methods are fully automatic and generally based on image-analysis techniques. These approaches generally rely on the identification of circular or elliptical arrangements of edges along the crater boundary. A standard approach is based on the use of a Generalized Hough Transform (GHT) [7]. Examples include the works of Cross [8], Cheng *et al.* [9], Honda *et al.* [10], Leroy *et al.* [11], and Michael [12]. Instead, in [13], the identification of impact craters was achieved through the analysis of the probability volume created as a result of a template matching procedure, approximating the craters as objects of round shape. That unsupervised method enables the identification of round spatial features. Kim and Muller [14] presented a crater detection method based on texture analysis and ellipse fitting. That method was not robust when applied to optical images. Therefore the authors needed to use also DEM data and fuse them with the optical data.

In subsequent work [15], Kim *et al.* proposed a combination of unsupervised and supervised techniques. In particular, edge detection, template matching, and supervised neural network-based schemes for the recognition of false positives were integrated, in order to automatically detect craters on Mars. In [16], Urbach and Stepinski presented a different approach, which combines unsupervised and supervised techniques, for crater detection in panchromatic planetary images. The method in [16] is based on using mathematical morphology for the detection of craters and on supervised techniques to distinguish between objects and false alarms.

Each of the previously published methodologies for automatic crater detection has its advantages and drawbacks. Although the recent approaches show high detection accuracy, the underlying technology is complicated and its robustness to different types of planetary surfaces and to image quality is not totally satisfactory yet.

Here, a novel automatic and unsupervised approach for the extraction of planetary craters, based on a Marked Point Process (MPP) [17], is proposed (see also [18]). An MPP is an abstract random variable whose realizations are configurations of objects, each object being described by a marked point (see Appendix A for more details). In the proposed method, the objects that are searched for are craters and a novel MPP model is defined to determine their statistical distribution in the image. The boundaries of the regions of interest are considered as a realization of an MPP of ellipses: Hence, the optimum configuration of objects has to be estimated. Similar to Markovian modeling, the "Maximum-A-Posteriori" (MAP) can be proved to be equivalent, under MPP assumption, to the minimization of a suitable energy function. An energy function, which takes into account the interactions between the geometric objects and the way they fit in the image, is minimized by using a Markov chain coupled with a simulated annealing scheme.

The main novelty of this paper is a novel unsupervised method for crater detection, based on the MPP stochastic modeling technique. Moreover, a new formulation of the likelihood energy function is proposed here, being more appropriate for the analyzed data. In comparison with other techniques, e.g., based on template matching, the proposed approach enables the identification of features of different shapes and orientations and it is applicable to different types of data.

The proposed approach is described in Section II. Experimental results with real data are presented and discussed in Section III. Finally, conclusions and ideas for future extensions are presented in Section IV.

II. METHODOLOGY

A. Overview of the proposed method

Planetary images show the surface of a planet and its structures. The aim of this study is to automatically detect elliptical structures, such as craters, that are present on a considered planetary surface by using image analysis techniques. The extracted features can be used for the registration of multitemporal, multisensor, and stereo-images.

Different types of spatial features are present in the planetary images, but the most evident ones are generally craters, i.e., objects of approximately elliptical shapes with shadows. Their extraction is a difficult task, because planetary images are blurry, quite noisy, present lack of contrast and uneven illumination, and the represented objects are not well defined.

In order to address this problem, an MPP-based approach, aimed at detecting round and elliptical objects, is proposed here. MPPs enable to model the distribution of complex geometrical objects in a scene (see Appendix A for more details) and have been exploited for different applications in image processing. Marked point processes have been successfully applied to address different problems in terrestrial remote sensing, among which road network detection [19], building extraction in dense urban areas [20], [21], [22], and road markings [23]. Moreover, in forestry applications, marked point processes have been used to reproduce the spatial distribution of the stems [24]. In [25], MPPs were used to detect and count flamingos on aerial photographs. Vascular tree detection in angiograms was addressed in [25]. Here, the method is applied to the detection of features in planetary images.

The context is stochastic and the goal is to minimize an energy on the state space of all possible configurations of objects, using a Markov Chain Monte-Carlo (MCMC) algorithm and a Simulated Annealing (SA) scheme. More properly, a novel MPP is introduced to model the structure of the crater edges in the image.

The overall architecture of the proposed approach for crater detection is shown in Figure 1. First, the noise is reduced by applying a smoothing filtering operation. Then, in order to produce an edge map I_g, showing the contours of the objects represented in the original image, the Canny edge detector [26] is applied. The Canny detector has been chosen because it guarantees a low error rate, the obtained edge points are well localized, and the width of each detected edge is one pixel.

The result of this first step, I_g, is a binary image that shows the object boundaries. Craters have a complex structure and, due to their depth and uneven illumination, exhibit shadows. Their borders can be approximated with incomplete non-continuous elliptical curves. The boundary information is extracted here, being a crater univocally
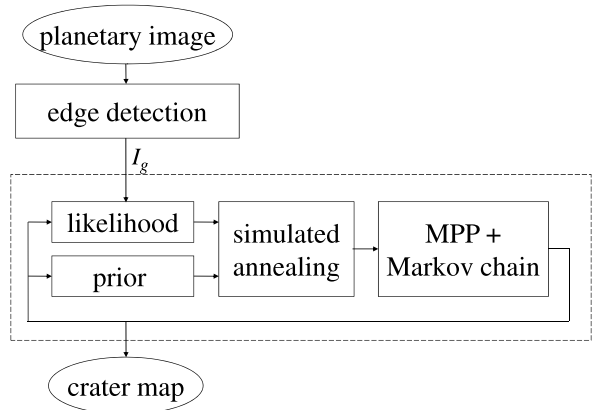

Fig. 1. Block diagram of the architecture of the proposed approach.

described by its contour.

I_g is modeled as a configuration of objects whose positions and attributes are a realization of an MPP X [27]. The MPP X is a process whose realizations are random configurations x of several objects, each belonging to a space $S = P \times K$, where P is the position space, and K the space of the marks, i.e., set of parameters that fully describe each object. Here, the 2D model, used to extract the features of interest, consists of an MPP of ellipses, and each ellipse is represented by a 5-tuple (u, v, a, b, θ), taking values in the set space

$$S = \overbrace{[0, M] \times [0, N]}^{P} \times \overbrace{[a_m, a_M] \times [b_m, b_M] \times [0, \pi]}^{K}, \tag{1}$$

where $(u, v) \in [0, M] \times [0, N]$ are the coordinates of the ellipse center (M and N being the width and height of I_g), a and b are the ellipse axes (ranging in $[a_m, a_M]$ and $[b_m, b_M]$, respectively), and $\theta \in [0, \pi]$ is the ellipse orientation angle.

The probability distribution of this stochastic process is uniformly continuous [28] with respect to a suitable Poisson measure on S. Operatively, this means that it may be characterized by a density f with respect to this measure. Similarly, the posterior distribution of x conditioned to I_g can also be characterized by a density function f_p with respect to the same measure and a Gibbs formulation is proven to hold for f_p [21]. Hence, one may introduce an energy function U such that

$$f_p(x|I_g) = \frac{1}{Z} \exp\{-U(x|I_g)\} \tag{2}$$

173

where Z is a normalizing constant. Hence, in order to minimize this posterior distribution, U will be minimized on the space of all configurations x in the feature extraction process.

B. The proposed energy function

The energy function takes into account the interactions between the geometric objects $x_1, x_2, ..., x_n$ in the configuration x (the prior energy U_P), and the way they fit to the data (the likelihood energy U_L)

$$U(x|I_g) = U_P(x) + U_L(I_g|x). \qquad (3)$$

The prior term characterizes the general aspect of the desired solution. According to the geometric properties of the configurations of craters, a basic rule is imposed on the prior term of our model. The prior energy, U_P, penalizes overlapping objects in x, which are very unlikely, by adding a repulsion between objects which intersect. The prior energy of our model is

$$U_P(x) = \frac{1}{n} \sum_{x_i \star x_j} R(x_i, x_j) \qquad (4)$$

where R is a repulsion coefficient, which penalizes each pair of overlapping objects (denoted as $x_i \star x_j$) in the configuration x. The repulsion coefficient φ is calculated as follows

$$\varphi(x_i, x_j) = \frac{x_i \cap x_j}{x_i \cup x_j} \qquad (5)$$

where $x_i \cap x_j$ denotes the overlapping area between the two objects x_i and x_j in the configuration ($i, j = 1, 2, ..., n$, $i \neq j$) and $x_i \cup x_j$ indicates the sum of the areas covered by the two objects x_i and x_j. It is worth noticing that the repulsion term φ, as defined in equation 5, penalizes overlapping object, but still allows them. In fact, overlapping craters are very rare but plausible.

Then, the likelihood term U_L is defined as

$$U_L(I_g|x) = U_S(I_g|x) + U_D(I_g|x), \qquad (6)$$

where U_S measures the similarity between the configuration and the data, whereas the data term U_D measures the distance between the objects in the configuration and the contours of the data. Different formulations for the likelihood energy, which have been proposed in previous work on MPP [24], [27], have proven to be unfeasible for planetary data.

Hence, a new formulation for U_L, more appropriate for the analyzed data, is proposed here.

In particular, the similarity energy U_S between the data I_g and the current configuration x is defined as a correlation measure[1] where u and v are the spatial coordinates in the image plane; $\Pi(\cdot|x)$ is the projection of the configuration x such that $\Pi(u, v|x) = 1$ if (u, v) belongs to the boundary of at least one ellipse in the configuration x (i.e., if there exists $i \in \{1, 2, ..., n\}$ such that (u, v) is on the boundary of x_i), and $\Pi(u, v|x) = 0$, otherwise. Consequently, U_S expressed as (7) is equivalent to the definition of a correlation function between the binary images I_g and $\Pi(\cdot|x)$, representing the extracted and the modeled edges, respectively. According to the correlation definition, in the binary case, only nonzero pixels from both images contribute to the value of the correlation. This energy term, which is novel with respect to the MPP literature, resembles analogous correlation measures that have been used for registration purposes [29]. The correlation measure in (7) is considered to be appropriate here because it enables to estimate the match between two binary images (I_g and Π) in a fast and accurate way.

Then, the data energy U_D is calculated at the object level: For each object x_i in the current configuration x a weight parameter W_i, proportional to the distance from the closest detected edge pixel in the data I_g with respect to its dimension, is calculated, i.e.,

$$W_i = \frac{d(G, O_i)}{\max(a_i, b_i)}, \qquad (8)$$

where

$$G = \{(u, v) : I_g(u, v) = 1\}, \qquad (9)$$

$$O_i = \{(u, v) : \Pi(u, v|x_i) = 1\}, \qquad (10)$$

$$d(A, B) = \inf\{||P - Q||\}, P \in A, Q \in B, \quad (11)$$

$\Pi(\cdot|x_i)$ has a meaning similar to above, and a_i and b_i are the two ellipse axes associated to the object x_i ($i = 1, 2, ..., n$).

The resulting data energy will be

$$U_D(I_g|x) = \frac{1}{n} \sum_{i=1}^{n} W_i. \qquad (12)$$

Then, objects with a low value of W will be favored in the configuration.

---

[1]Given a finite set A, we denote by $|A|$ the cardinality (i.e., the number of elements) of A.

$$U_S(I_g|x) = \frac{|\{(u,v) : I_g(u,v) = 1 \ \& \ \Pi(u,v|x) = 1\}|}{|\{(u,v) : I_g(u,v) = 1\}|} \tag{7}$$

C. Energy Minimization and Crater Mapping

A Markov Chain Monte-Carlo (MCMC) algorithm [30], coupled with a Simulated Annealing (applied with a given annealing schedule $T(\cdot)$), is used in order to find the configuration x which minimizes U.

We stress here that this minimization is carried out with respect to not only the locations and marks of the objects in the MPP realization but also the number of objects, i.e., the proposed method also automatically optimizes the choice of the number of detected craters. In particular, the marked point process X, defined by f, is sampled by using a random jump MCMC algorithm: It allows to build a Markov chain X_k ($k = 0, 1, ...$), which jumps between the different dimensions of the space of all possible configurations and, in the ideal case, ergodically converges to the optimum distribution x^* [31]. The final configuration of convergence does not depend on the initial state. The flowchart of the minimization scheme is shown in Figure 2.
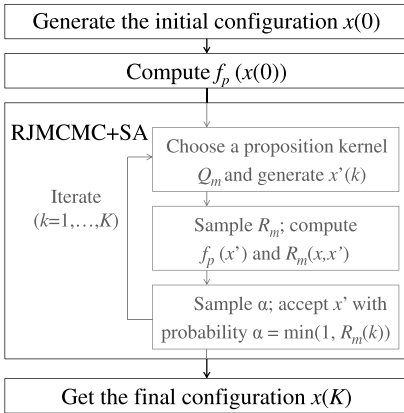

Fig. 2. Flowchart of the proposed minimization scheme.

At each step, the transition of this chain depends on a set of "proposition kernels", which are random changes proposed to the current configuration. In order to find the configuration maximizing the density $f_p(\cdot)$ on S, we sample within a Simulated Annealing scheme (SA), which gives us the MAP estimator. SA is an iterative algorithm where at each iteration k a perturbation is proposed to the current

configuration at temperature $T(k)$, $k = 1, 2, ..., K$). This perturbation is accepted or rejected with a probability which ensures that the probability distribution of the Markov chain ergodically converges to $f_p(x)^{\frac{1}{T(k)}}$. Here, the annealing schedule, $T(\cdot)$, is defined as

$$T(k) = T_I \cdot \left(\frac{T_F}{T_I}\right)^{\frac{k}{K}}, \tag{13}$$

where T_I and T_F are the initial and the final temperatures, respectively, and K is the total number of allowed iterations. In practice, in order to cope with too long computational times, the decrease of the temperature is geometric (as usual in SA for Markov random fields) and does also not imply the ergodic convergence to a probability distribution localized at the minima of $U(x|I_g)$, in contrast, it follows the adaptive approach developed in [32].

The efficiency of the algorithm highly depends on the variety of the proposition kernels Q. The set of proposition kernels are birth and death, translation, dilation, and rotation [33]. Birth and death are jumping perturbations, i.e, they vary the number of objects in the configuration. If birth is chosen, a new marked point is randomly generated and added to the configuration, while if death is chosen a randomly selected point in the configuration is removed. Non-jumping moves are transformations that do not change the number of objects in the configuration. In particular, a marked point is randomly selected and is replaced by a "perturbed" version of it.

For each proposition kernel m, a Green ratio $R_m(x, x')$ is defined, that tunes the likelihood of replacing configuration x by configuration x' at each SA iteration (analytical details can be found in Appendix B). More precisely, the birth and death kernel consists in proposing, with probability p_B, to uniformly add in S an object to the current configuration x or, with probability $p_D = 1 - p_B$, to remove a randomly chosen object of x. The Green's ratios for birth and death (namely, R_B and R_D, respectively) are

$$R_B = \frac{p_D}{p_B} \frac{f_p(x'|I_g)}{f_p(x|I_g)} \frac{\nu(S)}{n(x) + 1} \tag{14}$$

$$R_D = \frac{p_D}{p_B} \frac{f_p(x'|I_g)}{f_p(x|I_g)} \frac{n(x)}{\nu(S)}, \qquad (15)$$

where $n(x)$ is the number of objects in the current configuration x, x' is the candidate configuration, and $\nu(S)$ is the Poisson intensity measure. For the selected non-jumping kernels (i.e., translation, dilation, and rotation), the suitable Green's ratio is given by the usual Metropolis-Hastings ratio

$$R(x, x') = \frac{f_p(x'|I_g)}{f_p(x|I_g)}. \qquad (16)$$

III. EXPERIMENTAL RESULTS

Experiments were carried out using Mars data, collected during the 2001 Mars Odyssey mission, by the THermal EMission Imaging System (THEMIS), an instrument on board the Mars Odyssey spacecraft. Such an instrument combines a 5-band visual imaging system with a 10-band infrared imaging system [34]. Both 7 visible and 7 infrared THEMIS images, with a resolution of 18 meters and 100 meters per pixel, respectively, were used to test the proposed approach. In particular, the visible data set was chosen in the area with center longitude $lon = 352.86$ and center latitude $lat = -1.09$; the infrared data set was chosen within an area with $lon = 175.36$ and $lat = -14.68$.

Few parameters of the proposed method had to be assigned, concerning both the MPP state space S and the MCMC sampler. Let recall that $S = P \times K$, where $P = [0, M] \times [0, N]$ corresponds to the size of the data (I_g). The resolution r varies for the two different types of images used, hence the total area A of interest is $A = M \cdot N \cdot r^2$ [m^2]. The parameters of K (i.e, a_m, a_M, b_m, and b_M) depend on the size of the objects that need to be detected. In this study, the minimum size for both semi-axes was fixed to 3 pixels (i.e., $a_m = b_m = 3$) and the maximum size to 100 pixels (i.e., $a_M = b_M = 100$). The eccentricity e of each object, defined as

$$e = \sqrt{1 - \left(\frac{min(a,b)}{max(a,b)}\right)^2}, \qquad (17)$$

was constrained to $e \in [0, 0.6]$ (i.e., $min(a,b) \geq 0.8 \cdot max(a,b)$), being craters of bigger e unlikely.

Sampler probabilities needed to be assigned as well. In particular, the global parameters that correspond to the probability of choosing the proposition kernel m were fixed to $p_m = 0.25$, where $m \in$

$\{Tranlation, Rotation, Scaling, Birth\&Death\}$. The probabilities p_B and p_D regulating the birth and death kernel, were fixed to $p_B = p_D = 0.5$.

For comparison purposes, a method for ellipse detection based on a Generalized Hough Transform (GHT) [7] has been implemented and tested on our data set. With this method, for every pair of pixels that were detected as edge points in the Canny gradient and exhibit opposite gradient directions, an accumulator, corresponding to the median point between them in the image plane, is incremented by a unit value. The maxima of the accumulator are taken as centers of ellipses. Then, the three parameters describing the ellipse centered in each detected maximum are computed and a 3D accumulator is used to estimate the two semi-axes and the direction angle of the ellipse from all the pairs of points that contribute to the accumulator in the considered center. The results obtained by the proposed approach and by GHT were compared. This particular approach was chosen for comparison, being a standard technique for the detection of round and elliptical objects, commonly used for crater detection [12], [10], [11], [35].

Reference data were generated by manually analyzing each image of the data set and identifying all the craters that are present. Only objects completely included within the images were considered (i.e., objects cut by the borders of the image were discarded). A quantitative assessment of the obtained results by the proposed method was performed using these reference data. This was accomplished by comparing the obtained results with the labeled features in the correspondent reference map. The Detection percentage D, the Branching factor B, and the Quality percentage Q were computed as follows:

$$D = \frac{100 \cdot TP}{TP + FN}; \qquad (18)$$

$$B = \frac{FP}{TP}; \qquad (19)$$

$$Q = \frac{100 \cdot TP}{TP + FP + FN} \qquad (20)$$

where True Positive (TP) is the number of detected features that correspond to labeled objects in the reference map, False Positive (FP) is the number of features detected by the proposed approach, which do not correspond to any object in the reference map, and False Negative (FN) is the number of

Data	Method	D	B	Q
VIS	GHT	73%	0.24	62%
IR	GHT	78%	0.14	70%
Average	GHT	75%	0.20	65%
VIS	MPP	82%	0.22	71%
IR	MPP	89%	0.13	79%
Average	MPP	85%	0.18	74%

objects in the reference map that have not been detected by the proposed approach. The global values of D, B, and Q obtained by the proposed approach (MPP) and the standard method used for comparison (GHT) both for VIS and IR data are shown in Table I. The global values of D for VIS data and IR data obtained by the proposed approach were about 82% and 89%, respectively. These high values indicate a good detection rate (because of the high number of TP). B was about 0.22 for VIS and 0.13 for IR, which indicate a small amount of false detections with respect to the true detections in both cases, thanks to the small number of FP. The results obtained by applying the proposed approach are more accurate when compared to the performance of the implemented standard technique based on the GHT. In particular, the average value of the detection rate D improved from 75% for the GHT to 85% for the MPP. This is explained by the increase in true detections with respect to the reference map. Similarly, the quality percentage Q. A relatively smaller improvement in the branching factor B is due to the fact that the number of FP was already small when applying GHT.

Moreover, the detection performance of the proposed approach in terms of D, B, and Q compares also favorably with most of the results previously published for automatic crater detection methods [13], [16], [36], [37]. Ideally, the performance of the proposed approach should be compared with the results obtained by the previously published methods when applied to the same data. Unfortunately, the performance of each published approach has been assessed on different sites and distinct types of data (e.g., panchromatic images, topographic data). The most direct performance comparison can be made with the method proposed

by Barata *et al.* in [36]. That approach was tested on images acquired by the Mars Orbiter Camera (MOC). The method in [36] identified 546 craters, with $TP = 171$, $FN = 93$, and $FP = 282$. Hence, the resulting assessment factors were about $D = 65\%$, $B = 1.65$, and $Q = 31\%$. Bandeira *et al.* [13] proposed an unsupervised approach for crater detection from MOC data based on template matching. The average performances of that approach were about $D = 86\%$ and $Q = 84\%$. However, they tested their algorithm on images having resolution of 200-300m/pixel. The high performances obtained in [13] may be attributed to the fact that large craters in the sites of analysis have a very regular shape and are relatively easy to identify by template matching. The performance of that approach for the detection of small and irregular craters is unknown. Bue and Stepinski [37] proposed a supervised approach for crater detection from topographic data. The average performances of that approach were about $D = 74\%$, $B = 0.29$, and $Q = 61\%$. The evaluation factors increased to $D = 92\%$, $B = 0.29$, and $Q = 73\%$ if degraded craters, which the method was not able of detecting, were excluded. That approach is not fully comparable with the proposed method, being supervised. Urbach and Stepinski [16] proposed a supervised approach for crater detection from panchromatic images. The performance factors of their method were about $D = 68\%$, $B = 0.29$, and $Q = 57\%$, when detecting craters of diameter greater that 200m, and lower when taking into account also craters of smaller dimensions. However, a full comparison with our approach is again not possible. In general, the results obtained by the proposed approach are comparable to, and in some cases better than results obtained by methods reported in the literature in terms of the assessment factors. Unfortunately, a full comparison is not possible, because the methods were applied to different data.

Visual results of the feature extraction are shown for the first band of a visible image (Fig. 3(a)). The image is first preprocessed, in order to reduce the noise. In particular, Gaussian filtering and median filtering operations are applied in a cascade [38] in order to reduce the noise and preserve the edges at the same time. The Canny edge detector is applied to the smoothed image and the binary gradient I_g is shown in Fig. 3-b. The estimated optimum configuration of the MPP x^*, which identifies the
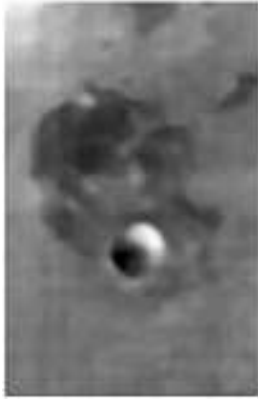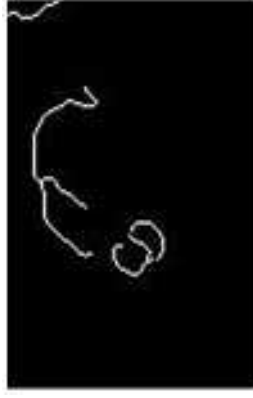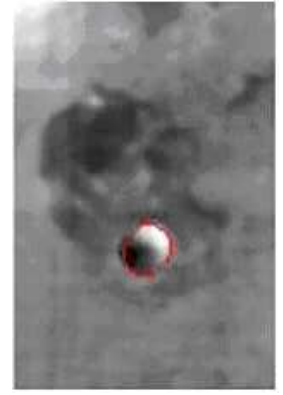
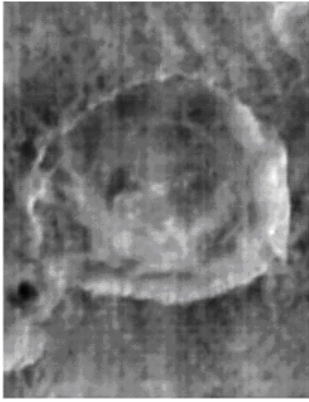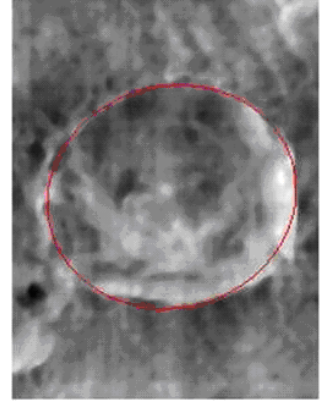|		
(a) Original image	(b) Image edges	(c) Crater contours

Fig. 3. Experimental results obtained by applying the proposed method to the first band of a visible image. (a) Original image, (b) Canny gradient, and (c) detected crater contours in red, transparently superimposed to the original image.

(a) Original image	(b) Image edges	(c) Crater contours

Fig. 4. Experimental results obtained by applying the proposed method to the eighth band of an infrared image. (a) Original image, (b) Canny gradient, and (c) detected crater contours in red, transparently superimposed to the original image.

feature contours, is shown in Fig. 3-c. The optimum configuration x^* is represented in red, transparently superimposed to the original image. By a visual inspection, it is possible to appreciate the accuracy of the detection, even when many false alarms are present in the binary image gradient I_g. Also the reconstruction of the feature shape is very accurate.

Then, visual results obtained by applying the proposed approach to the eighth band of an infrared image (Figure 4-a) are presented. In particular, the Canny gradient I_g is shown in Fig. 4-b and the estimated x^* is shown in Figure 4-c, transparently superimposed to the original image. The contours of

the represented crater appear non-continuous in the binary image gradient I_g, due to the uneven quality of the image. Anyway, the feature is correctly detected and its shape reconstructed.

A visual analysis of the detection results obtained with other planetary images (see Fig. 5) confirms that the proposed method is able to correctly identify the location and shape of the imaged craters, even though the input edge map detected only part of the crater borders, included many spurious contours unrelated with the craters, and was severely affected by the shadows in the crater area.
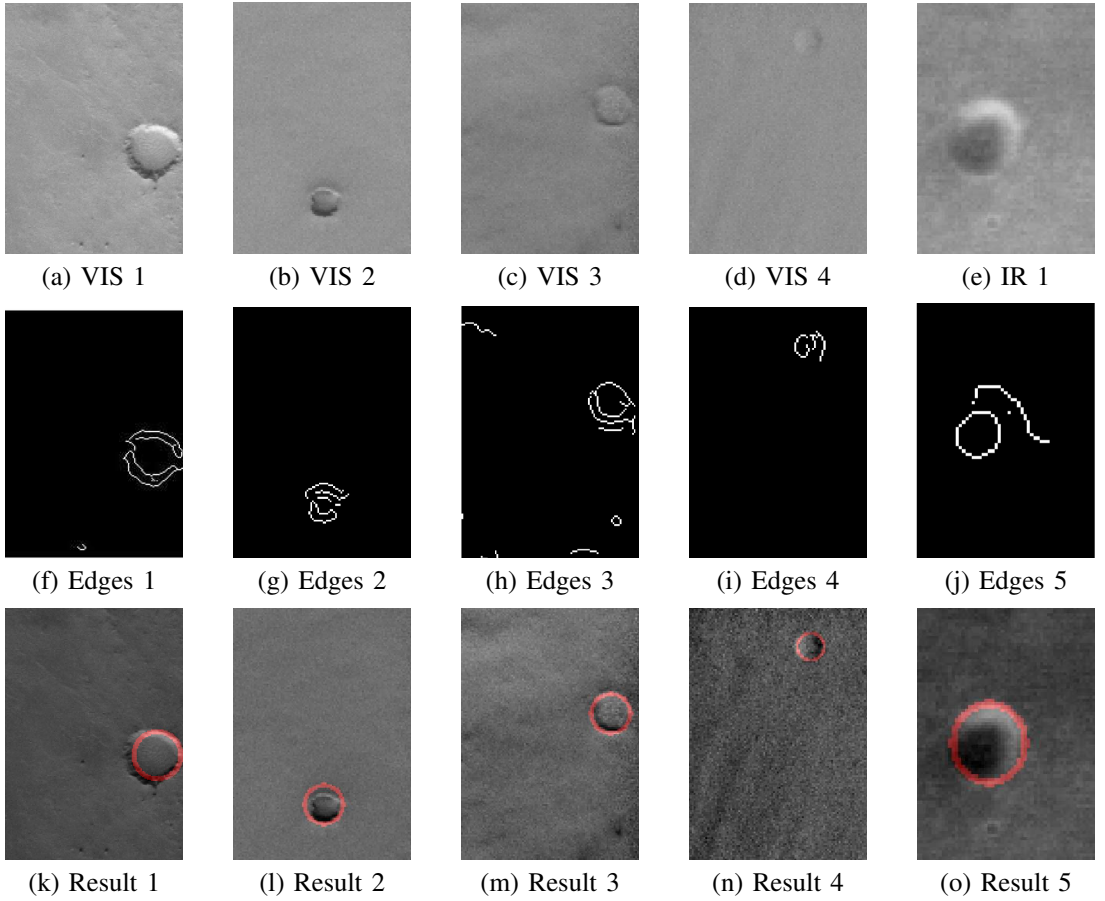
178

Fig. 5. Examples of experimental results obtained by the proposed method. (a), (b), (c), (d), (e) Original data, (f), (g), (h), (i), (j) respective edge maps, and (k), (l), (m), (n), (o) detected crater contours in red.

IV. CONCLUSIONS

In this paper, a novel approach has been proposed for automatic detection of features that characterize planetary surfaces. The identification is achieved by using a method based on a Marked Point Process (MPP), coupled with a Markov chain and a simulated annealing scheme.

Mars infrared and visible multiband images, captured by THEMIS during the Mars Odyssey Mission, were used. Before the algorithm could be used to estimate the MPP optimum configuration, the images had to go through a preprocessing stage, aimed at obtaining contour map of the analyzed image. The likelihood between the extracted map and the current configuration was measured and maximized, in order to identify the optimum configuration.

The MPP approach, which was developed in the context of computer vision and previously used in many different applications (e.g., tree crown identification, road network detection, building extraction), has proven to be effective when applied to planetary images here. For such data, the features to be extracted are not as well contrasted nor defined as for Earth data. Nevertheless, we showed here that their identification can be accurately achieved. The accuracy of the detection has been assessed by a comparison to a manually generated reference map. The method outperformed a standard method for crater detection based on a generalized Hough transform, in terms of several indices based on true positives, false negatives, and false positives. Moreover, the obtained results compared favorably

to most previously proposed approaches, when performances reported in the literature were considered for the same indices. Finally, a visual inspection of the detection results confirmed that the proposed method was also able to correctly identify the location and shape of the detected craters.

In our future work, we will investigate the use of an illumination correction to improve the reliability of the detection for all craters, when shadows are present. Illumination correction, based on the knowledge of the orbital angle and the acquisition time, will be useful to reduce the bias in the reconstruction of the exact feature shape. Moreover, we plan to integrate the shadow information around the features in order reduce the false alarms in the contour map.

The proposed approach can be adopted as the first important step in several applications dealing with all the various data that are being collected during the current and future planetary missions. Among them selecting safe landing sites, identifying planetary resources, and preparing for subsequent planetary exploration by humans and robots. The proposed approach will also be applied to the registration of multisensor and multitemporal images, by performing feature matching.

References

[1] G. Salamuniccar and S. Loncaric, "Method for crater detection from martian digital topography data using gradient value/orientation, morphometry, vote analysis, slip tuning, and calibration," *IEEE Trans. Geosci. Remote Sens.*, vol. 48, pp. 2317–2329, 2010.

[2] A. Flores-Mendez, *Crater Marking and Classification using Compu. Vision.* New York: Springer-Verlag, 2003, vol. 2905.

[3] T. Vinogradova, M. Burl, and E. Mjolsness, "Training of a crater detection algorithm for mars crater imagery," in *IEEE Aerospace Conference Proceedings*, vol. 7, 2002, pp. 3201–3211.

[4] P. G. Wetzler, B. Enke, W. J. Merline, C. R. Chapman, and M. C. Burl, "Learning to detect small impact craters," in *IEEE WACV*, vol. 1, 2005, pp. 178–184.

[5] R. Martins, P. Pina, J. S. Marques, and M. Silveira, "Crater detection by a boosting approach," *IEEE Geosci. Remote Sens. Lett.*, vol. 6, pp. 127–131, 2009.

[6] P. Viola and M. Jones, "Robust real-time face detection," *Int. J. Compu. Vision*, vol. 57, pp. 137–154, 2004.

[7] S. Tsuji and F. Matsumoto, "Detection of ellipses by a modified Hough transformation," *IEEE Trans. Comput.*, vol. 27, 1978.

[8] A. M. Cross, "Detection of circular geological features using the Hough transform," *Int. J. Remote Sens.*, vol. 9, pp. 1519–1528, 1988.

[9] Y. Cheng, A. E. Johnson, L. H. Matthies, and C. F. Olson, "Optical landmark detection for spacecraft navigation," in *13th Annu. AAS/AIAA Space Flight Mech. Meeting*, Feb. 2002.

[10] R. Honda, Y. Iijima, and O. Konishi, "Mining of topographic feature from heterogeneous imagery and its application to lunar craters," in *Progress in Discovery Sci.*, ser. Lecture Notes in Compu. Sci., S. Arikawa and A. Shinohara, Eds. Springer Berlin / Heidelberg, 2002, vol. 2281, pp. 27–44.

[11] B. Leroy, G. Medioni, A. E. Johnson, and L. H. Matthies, "Crater detection for autonomous landing on asteroids," *Image Vision Comput.*, vol. 19, pp. 787–792, 2001.

[12] G. G. Michael, "Coordinate registration by automated crater recognition," *Planetary and Space Sci.*, vol. 51, pp. 563–568, 2003.

[13] L. Bandeira, J. Saraiva, and P. Pina, "Impact crater recognition on mars based on a probability volume created by template matching," *IEEE Trans. Geosci. Remote Sens.*, vol. 45, pp. 4008–4015, 2007.

[14] J. R. Kim and J.-P. Muller, "Impact crater detection on optical images and DEM," in *ISPRS*, Houston, TX, 2003.

[15] J. R. Kim, J.-P. Muller, S. van Gasselt, J. G. Morley, and G. Neukum, "Automated crater detection, a new tool for mars cartography and chronology," *Photogrammetric Eng. Remote Sens.*, vol. 71, no. 10, pp. 1205–1217, 2005.

[16] E. R. Urbach and T. F. Stepinski, "Automatic detection of sub-km craters in high resolution planetary images," *Planetary Space Sci.*, vol. 57, pp. 880–887, 2009.

[17] M. van Lieshout, *Marked Point Processes and their Applications.* London: Imperial College Press, 2000.

[18] G. Troglio, J. A. Benediktsson, G. Moser, and S. B. Serpico, "Crater detection based on marked point processes," in *IEEE Int. Geosci. Remote Sens. Symp.*, 2010.

[19] X. Descombes and J. Zerubia, "Marked point processes in image analysis," *IEEE Signal Proces. Mag.*, vol. 19, no. 5, pp. 77–84, 2002.

[20] F. Cerdat, X. Descombes, and J. Zerubia, "Urban scene rendering using object description," in *IEEE International Geoscience and Remote Sensing Symposium*, vol. 1, 2003, pp. 62–64.

[21] M. Ortner, X. Descombes, and J. Zerubia, "A marked point process of rectangles and segments for automatic analysis of digital elevation models," *IEEE Trans. Pattern Anal. Mach. Intell*, vol. 30, no. 1, pp. 105–119, 2008.

[22] M. Quartulli and M. Datcu, "Stochastic geometrical modeling for built-up area understanding from a single sar intensity image with meter resolution," *IEEE Transactions on Geoscience and Remote Sensing*, vol. 42, no. 9, pp. 1996–2003, 2004.

[23] O. Tournaire and N. Paparoditis, "A geometric stochastic approach based on marked point processes for road mark detection from high resolution aerial images," *ISPRS Journal of Photogrammetry and Remote Sensing*, vol. 64, no. 6, pp. 621 – 631, 2009.

[24] G. Perrin, X. Descombes, and J. Zerubia, "Tree crown extraction using marked point processes," in *EUSIPCO Conf.*, Vienna, Austria, 2004.

[25] S. Descamps, X. Descombes, A. Bechet, and J. Zerubia, "Automatic flamingo detection using a multiple birth and death process," in *IEEE International Conference on Acoustics, Speech and Signal Processing*, 2008, pp. 1113 –1116.

[26] J. Canny, "A computational approach to edge detection," *IEEE Trans. Pattern Anal. Mach. Intell.*, vol. 10, no. 6, 1986.

[27] G. Perrin, X. Descombes, and J. Zerubia, "A marked point process model for tree crown extraction in plantations," in *IEEE ICIP*, 2005, pp. 661–664.

[28] W. Rudin, *Principles of Mathematical Analysis.* New York: 2nd edition, McGraw-Hill, 1976.

[29] G. Matsopoulos, N. Mouravliansky, K. Delibasis, and K. Nikita, "Automatic retinal image registration scheme using global op-

180

timization techniques," *IEEE Trans. on Information Technology in Biomedicine*, vol. 3, no. 1, pp. 47–60, 1999.

[30] C. Geyer and J. Moller, "Likelihood inference for spatial point processes," *Stochastic Geometry Likelihood Comput.*, 1998.

[31] C. Robert and G. Casella, *Monte Carlo statistical methods*. New York: Springer-Verlag, 1999.

[32] G. Perrin, X. Descombes, and J. Zerubia, "Adaptive simulated annealing for energy minimization problem in a marked point process application," in *EMMCVPR Conf.*, Saint Augustine, FL, 2005.

[33] P. Green, "Reversible jump Markov chain monte carlo computation and Bayesian model determination," *Biometrika*, vol. 82, pp. 711–732, 1995.

[34] P. Christensen, B. M. Jakosky, H. H. Kieffer, M. C. Malin, H. Y. Mcsween, K. Nealson, G. L. M. S. H. Silverman, S. Ferry, M. Caplinger, and M. Ravine, "The thermal emission imaging system for the mars 2001 odyssey mission," *Space Sci. Rev.*, vol. 100, pp. 85–130, 2004.

[35] G. Troglio, J. L. Moigne, J. A. Benediktsson, G. Moser, and S. B. Serpico, "Automatic extraction of planetary image features," in *IEEE Int. Conf. SMC-IT*, Pasadena, CA, 2009, pp. 211–215.

[36] T. Barata, E. I. Alves, J. Saraiva, and P. Pina, *Automatic Recognition of Impact Craters on the Surface of Mars*. Berlin, Germany: Springer-Verlag, 2004, vol. 3212.

[37] B. D. Bue and T. F. Stepinski, "Machine detection of martian impact craters from digital topography data," *IEEE Trans. Geosci. Remote Sens.*, vol. 45, pp. 265–274, 2007.

[38] L. G. Shapiro and G. C. Stockman, *Computer Vision*. Prentice Hall, 2001.

Acknowledgment

First of all, I would like to thank my thesis advisors. In particular, a special thank goes to Jon Atli, which has been a really good tutor, giving me great opportunities and strong technical support. But, apart from that, I would like to thank him for being a wonderful person, always positive and encouraging. Likewise, my gratitude goes to Bruno, which gave me the opportunity to start this experience, supported me during this pleasant years, demonstrated to appreciate my work and helped me a lot. Working with both of you has been a great experience.

My acknowledgment goes to Einar and Johannes for serving on my PhD committee, for their interest to my work, and for the helpful comments they have provided me with. I also want to thank Helgi Þorbergsson for presiding over the defense, and Josiane Zerubia and John Kerekes for accepting the role of opponents.

A huge huge thank to Gab, for all the time he spent helping me, starting from my Master thesis 4 years ago, for being always available, and for the technical support he has given me during these years. But thanks also for being a good friend, for the company as an office mate, as a co-traveler in Hawaii, as a visitor in Iceland and for being brave enough to sneak into the blue lagoon :-)

All my gratitude goes to Jacqueline, for giving me the opportunity to spend a stimulating period in her research group at the Goddard Space Flight Center. I also wish to thank her and her great family for

being so welcoming to me.

Then, those people who made the time in Iceland great: thanks to granfa Alberto, the party-goer Kevin, Doctor-PhD Prashanth, the rocker Nicola, los guapos Silvia y Xabi, Romain, Cloe, Mauro, Yuliya. A special thank to Bjorn. Merci Zohra et Louise. Thanks to all the people that I did not mention, thank to the Oxymap-Landspitali team, to the Icelandic people at the University. But a last special thank goes to Hildur and Hafrun, for being other than co-workers really good friends and for sharing with me a bit of their lives and Icelandic culture.

Poi, un grazie speciale ai colleghi di ufficio ed ai compagni di animate pause pranzo genovesi.

E soprattutto grazie a chi fuori dal lavoro mi ha dato un appoggio morale. Grazie agli amici. Grazie alla neo-mamma Vale e scapestrata Eli. Grazie alla Ju e tutti i savonesi (emigrati e non). Grazie agli affettuosissimi Massi e Marco.

Manca qualcuno?? Beh, sì! Grazie a mamma e papà! Per avermi accompagnato, stimolato e compreso negli scorsi (ahimè) quasi-29 anni. Per essere stati 2 genitori speciali, aperti e disponibili. Grazie a voi, ai vostri stimoli ed ai vostri sogni nel cassetto ho scelto di intraprendere tutte le esperienze che mi hanno permesso di arrivare fin qua.

Manca ancora qualcuno??? Beh, sì... La persona che, nonostante qualche piccola divergenza, rimane il mio coinquilino preferito ;-) Grazie Rurù per avermi saputo capire, stimolare ed appoggiare nei momenti di sconforto, per avermi aiutato a trovare la forza per reagire quando tutto era nero... per aver sopportato tutti i miei sbalzi d'umore! Ed infine grazie per aver accettato la distanza dovuta a questa esperienza, che ci ha unito invece di allontanaci! Biribì.

Grazie!!

Giulia